Towards an Optomechanical Quantum Memory

Preparation and Storage of Non-Classical States in High-Frequency Mechanical Resonators

Wallucks, Andreas

DOI
10.4233/uuid:388a09c0-1619-4947-9d82-f27eedf88155

Publication date
2020

Document Version
Final published version

Citation (APA)
Wallucks, A. (2020). *Towards an Optomechanical Quantum Memory: Preparation and Storage of Non-Classical States in High-Frequency Mechanical Resonators*. [Dissertation (TU Delft), Delft University of Technology]. https://doi.org/10.4233/uuid:388a09c0-1619-4947-9d82-f27eedf88155

Towards an Optomechanical Quantum Memory

Preparation and Storage of Non-Classical States in High-Frequency Mechanical Resonators

TOWARDS AN OPTOMECHANICAL QUANTUM MEMORY

PREPARATION AND STORAGE OF NON-CLASSICAL STATES IN HIGH-FREQUENCY MECHANICAL RESONATORS

Dissertation

for the purpose of obtaining the degree of doctor
at Delft University of Technology
by the authority of the Rector Magnificus Prof. dr. ir. T.H.J.J. van der Hagen,
chair of the Board for Doctorates,
to be defended publicly on
Monday 10 February 2020 at 10:00 o'clock

by

Andreas WALLUCKS

Master of Science,
University of Konstanz, Germany
born in Freiburg im Breisgau, Germany

This dissertation has been approved by the promotors.

Composition of the doctoral committee:

Rector Magnificus,	chairperson
Dr. S. Gröblacher,	Delft University of Technology, promotor
Prof. dr. ir. H. S. J. van der Zant	Delft University of Technology, promotor
Independent members:	
Prof. dr. L. Kuipers,	Delft University of Technology
Prof. dr. H.-J. Schmiedmayer,	Vienna University of Technology
Prof. dr. S. D. C. Wehner,	Delft University of Technology
Prof. dr. W. Pernice,	University of Münster
Dr. W. Löffler	Leiden University

Printed by: ipskamp printing

Front & Back: Artistic depiction of the bandstructure of a phononic shield, conceived together with Anne Wallucks.

Casimir PhD series, Delft-Leiden 2020-04
ISBN 978-90-8593-431-8

An electronic version of this dissertation is available at
http://repository.tudelft.nl/.

CONTENTS

SUMMARY

Cavity Optomechanics is a field employing optical control over mechanical oscillators with a variety of possible applications for sensing, optical signal processing as well as quantum technologies. Such systems are attractive because they are often fully engineerable and can be tailored to specific applications by allowing a large range of frequencies and the usage of a number of host materials. The following work explores one such application of a high frequency, ultra-long lived mechanical mode as a quantum memory which can be read out on-demand via an optical interface. In chapter 1, we introduce the device design and discuss the optomechanical interactions. We also review the requirements for an application of the memory in long-distance entanglement distribution with the DLCZ protocol. We argue that such mechanical devices constitute a promising technology for future quantum networks and discuss how they differ from competing systems.
Chapter 2 gives a detailed description of the experimental techniques used in the later chapters. We describe the fabrication of the device in the cleanroom, show how the optical coupling to the chip is achieved in the cryostat and discuss the full setup for the single photon counting experiments. In chapter 3 we continue by giving details on the most important measurements that can be used to characterize the performance of the devices. This includes the detection of the optical mode with continuous light, as well as pulsed experiments on the mechanical mode for thermometry and ringdown measurements. We finish this discussion by demonstrating quantum behavior of the device with the heralded preparation of a phonon Fock state using single photon counting.
In chapter 4 we demonstrate the heralded entanglement generation between two devices by projection onto a Bell state, which we verify using an entanglement witness. Chapter 5 continues with an experiment with improved device performance which allows us to perform a Bell test including two mechanical devices and two optical modes. While not closing the loopholes, we can show strong quantum correlations between the modes which are necessary for realistic applications.
In chapter 6 we focus on the actual memory aspect of the modes by performing a series of experiments on a device with greatly improved mechanical quality factor. We demonstrate that the mode can be used to store Fock states for its whole ringdown time of more than one millisecond. We furthermore prepare the mode in a superposition with the vaccuum and find a dephasing of the state on a timescale around ten microseconds.
In chapter 7, we summarize the findings of these experiments and discuss future directions for both improved device performance as well as alternative use cases of the system as more versatile quantum memory.

SAMENVATTING

Cavity Optomechanics is een veld in de natuurkunde waarin gebruik gemaakt wordt van de optische controle over mechanische oscillatoren met een verscheidenheid aan toekomstige toepassingen voor detectie, optische signaalverwerking en kwantumtechnologieën. Dergelijke systemen zijn aantrekkelijk omdat ze vaak kunnen worden aangepast aan specifieke toepassingen, door een hele reeks frequencies en verschillende materialen toe te laten. Het volgende werk onderzoekt een dergelijke toepassing van een hoogfrequente mechanische resonator met ultra-lage demping als een kwantum-geheugen dat op aanvraag kan worden uitgelezen via een optische koppeling. In hoofdstuk 1 introduceren we het chipontwerp en bespreken we de optomechanische interacties. We motiveren ook de exacte toepassing van het geheugen voor de distributie van kwantum verstrengeling op lange afstand met het DLCZ-protocol. We stellen dat mechanische resonatoren een veelbelovende technologie vormen voor toekomstige kwantumnetwerken en bespreken hoe ze verschillen van concurrerende systemen.
Hoofdstuk 2 geeft een gedetailleerde beschrijving van de experimentele technieken die in de latere hoofdstukken worden gebruikt. We bespreken de fabricage van de chips in de cleanroom, laten zien hoe de optische koppeling in de cryostaat wordt bereikt en bespreken de volledige opstelling voor de experimenten voor het tellen van individuele fotonen. In hoofdstuk 3 gaan we verder met deze bespreking door details te geven over de belangrijkste metingen die gebruikt kunnen worden om de prestaties van de chips te karakteriseren. Dit omvat de detectie van de optische resonantiefrequentie met continu licht, evenals gepulseerde experimenten voor thermometrie en 'ringdown'-metingen van de mechanische resonator. We eindigen deze discussie door het kwantumgedrag van het apparaat te demonstreren met de 'heralded' aanmaak van een phonon Fock toestand met behulp van enkele fotontelling.
In hoofdstuk 4 demonstreren we de 'heralded' verstrengeling generatie tussen twee chips door projectie op een Bell-toestand, die we verifiëren met behulp van een verstrengelingsgetuige. Hoofdstuk 5 gaat verder met een experiment met verbeterde chips waarmee we een Bell-test kunnen uitvoeren met twee mechanische resonatoren en twee optische velden. Hoewel we de theoretische mazen niet dichten, kunnen we sterke kwantumcorrelaties tonen tussen de velden die nodig zijn voor realistische toepassingen.
In hoofdstuk 6 richten we ons op het feitelijke geheugenaspect van de resonanties door een reeks experimenten uit te voeren op een chip met een sterk verbeterde mechanische kwaliteitsfactor. We tonen aan dat de resonantie gebruikt kan worden om Fock-toestanden op te slaan voor de hele 'ringdown' tijd van meer dan één milliseconde. We bereiden de resonantie bovendien voor in een superpositie met het vacuüm en vinden een defasering van de staat op een tijdschaal van ongeveer tien microseconden.
In hoofdstuk 7 vatten we de bevindingen van deze experimenten samen en bespreken we toekomstige mogelijkheden voor zowel verbeterde chipprestaties als alternatieve gebruikstoepassingen van het systeem als veelzijdig kwantumgeheugen.

1

INTRODUCTION

Long-distance entanglement distribution is one of the current frontiers in quantum optics and quantum information science, promising novel communication and metrology applications. Direct transmission allows for ranges up to few hundreds of kilometers in modern ultra low-loss fiber-optic networks. Beyond that, quantum repeater protocols based on optical quantum memories are required. While there exist many protocols and proof-of principle demonstrations have been successful in several systems, the performances of the quantum memories have not yet allowed for real world applications. Here we discuss mechanical resonators as a new approach suitable for integration into the DLCZ-scheme. We argue that, with improved efficiencies, they could be used in the future as versatile quantum memories due to a substantial design freedom and incorporation possibilities to other quantum techniques. At the same time, researching long-lived mechanical modes opens avenues to test fundamental physics alike.

1

1.1. QUANTUM MEMORIES FOR LONG-DISTANCE ENTANGLEMENT DISTRIBUTION

Optical photons are ideal carriers of quantum information as they move quickly and, due to their high frequencies, they are almost decoherence-free at ambient temperatures. Optical components to route and manipulate light at telecom frequencies are commercially available with high efficiencies. Homodyne setups are able to perform quantum noise limited detection and superconducting nanowires can be used to spot individual photons with efficiencies approaching unity. Technologies using light as the carrier for quantum information are being explored, including linear optical quantum computation techniques [1], quantum cryptography [2] and quantum communication techniques to establish links between future quantum computers [3, 4]. Many of these schemes rely on simultaneous successful outcomes of many individual probabilistic processes. Some of those are unavoidable, for example due to weak non-linear optical interactions or stochastic quantum light sources. Others are by design, including heralded quantum state preparation or entanglement purification, where probabilistic protocols are used to achieve high state fidelities in a trade-off with the chance of a successful outcome. As a result, scaling of these techniques into mature technologies is hindered because the total probability of success is quickly reduced with increased complexity and the overall rates become minute. To develop ever more complex optical quantum technologies, synchronization devices have to be developed which can hold on to optical quantum states such that all dependencies are resolved before further processing.

Enter optical quantum memories [5]. An ideal multi purpose memory would allow to efficiently store and retrieve a quantum state of any quantum light source for arbitrary times with on-demand operation and high fidelity. Such a device has been elusive, and current approaches have focused on highly specialized devices tailored for specific tasks. In this work, we focus on memories for long-distance quantum communication. Here entanglement is distributed between the two endpoints of a optical link as a resource for secure communication using quantum cryptography protocols or for the transmission of unknown quantum states using quantum teleportation. Note that quantum states cannot be amplified to overcome unavoidable transmission losses and hence the probability for a successful entanglement distribution decreases exponentially with distance. Imagine the transmission of entangled photons over 1000 km of standard telecom fiber with attenuation of 0.17 dB/km at a repetition rate of 10 MHz. A successful detection of a photon at the other side would take on average more than 100 years, a prohibitively long time for practical communication tasks.

Quantum repeater protocols can allow for more efficient communication by dividing the distance into much shorter segments, each well below the attenuation length of the channel. Entanglement can then be distributed between the nodes of these segments by transmission of single photons with relatively high probabilities. In a second step, the entanglement in the segments can be converted to long-distance entanglement between the two endnodes of the channel by entanglement swapping operations, which are pairwise joint measurements on the states of the memories. We will describe a particular protocol for this in section 1.3. Crucially, even if the operations on the individual links have only modest success rates, polynominal scaling of the swapping probability allows

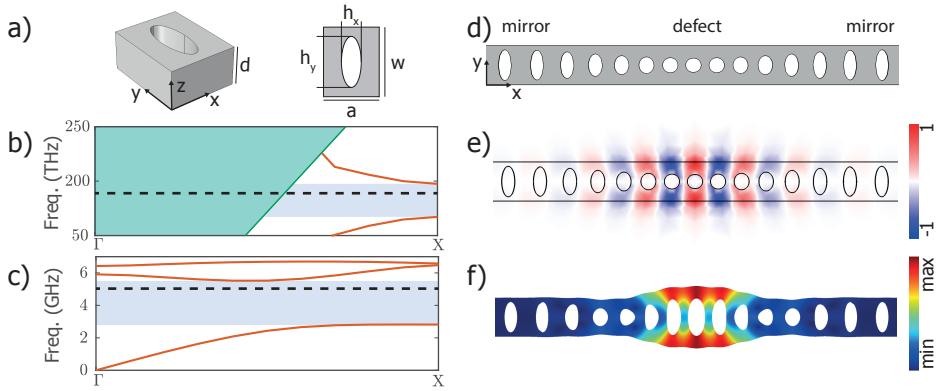

Figure 1.1: (a) Unit cell of the mirror region. The dimensions of the design are given in the main text. (b) Optical bandstructure simulation of the mirror region with the green shaded region indicating unguided modes above the light line. The bandgap is shown in light blue shade and the defect frequency ω_c of the full structure as a dashed line. (c) Mechanical bandstructure simulation of the mirror region. Shown are only the modes with xy-symmetry as well as the bandgap shaded in light blue and the defect frequency as a dashed line. (d) Full nanobeam design, in which the unit cell dimensions are adiabatically transformed from the mirror region to the defect dimensions given in the main text. (e) Optical simulation, shown is the electric field component E_x. (f) Mechanical simulation of the displacement amplitude.

such a scheme to asymptotically outperform direct transmission for long distances. A demonstration of this increase in efficiency is so far outstanding due to a lack of suitable and scalable optical quantum memories.

In this thesis we explore engineered mechanical structures as a new approach to build an optical quantum memory. Such mechanical excitations share many similarities to optical modes with both having bosonic fundamental excitations, photons and phonons. Optical modes can thus in principle always be mapped on acoustic ones as they share the same Hilbert space. The key difference with regards to a quantum memory is that the propagation of phonons is bound to the speed of sound in their host material which is orders of magnitude slower than the speed of light. Current microfabrication techniques additionally allow to build acoustic cavities with extremely high quality factors, which could be used to store quantum states for extended amounts of time. The main technical challenge is thus to provide an efficient light-matter interface to be able to inter-convert the quantum information. Here, we use the optomechanical interaction, which is a parametric coupling between light and mechanical motion due to radiation pressure forces [6]. We describe these devices and the relevant optomechanical interactions in the following section 1.2 and describe an application as a quantum memory in section 1.3.

1.2. SILICON NANOBEAMS

The following chapters describe experiments with optomechanical nanobeams which were originally developed in Caltech based on earlier integrated photonics designs (see e.g. [7]). Beams of silicon can act as waveguides for light due to total internal reflection.

Periodically patterning the beams with holes can create bandstructures with which individual guided modes can be defined. Bandgaps can furthermore be designed to introduce highly reflective mirror regions in the beams. The interference for light scattered from the individual holes depends on the wavelength of the light. To achieve telecom operation at frequencies around $\omega_c \approx 200$ Thz, our design employs a lattice-constant of $a = 439$ nm. The hole width is h_x=161 nm, the hole height is h_y=404 nm and the beam thickness is d=250 nm, as defined in Figure 1.1a. The simulated bandstructure in Figure 1.1b shows the formation of a bandgap, i.e. a region in frequency in which modes cannot propagate in the beam. Optical cavities can be designed by introducing defect modes in the middle of this bandgap by deforming the unit cell adiabatically over a number of holes. Scattering to the outside of the light cone can be avoided by a smooth transition, while keeping the mode volume close to the theoretical limit of $(\lambda/2n)^3$ [8]. In the defect, the design parameters from the mirror region are reduced to $a = 319$ nm, $h_x = 193$ nm and $h_y = 175$ nm. While simulated structures easily achieve optical quality factors exceeding 10 million, fabricated nanobeams are typically bound to quality factors of one million and below, resulting in intrinsic FWHM linewidths of κ_i=200 Mhz and above.

The crucial innovation of the Caltech group was to realize that localized phonon modes can be formed by the same design principles, and even in about the same mode volume. A simulated bandstructure for acoustic waves is shown in Figure 1.1c, including the defect frequency that is created by the deformation of the unit cell. Notably, the bandgap that is formed by the mirror is only a bandgap for a certain phonon polarization. Elastic waves with xy-symmetry cannot propagate whereas all others can. This is a feature which can limit the achievable quality factors of the modes in practice and is therefore considered further in chapter 6. The mode that is generated by the defect is often called a breathing mode, it is shown in Figure 1.1f. The material periodically expands and contracts in the center with a frequency of $\Omega/2\pi \approx 5\ GHz$. The mechanical confinement can be extremely good with mechanical damping times exceeding one second [9].

Co-confining the optical and mechanical modes enables a coupling term between the two. Physically, the interaction is caused to the most extend by an interplay between electrostriction and photoelasticity. Electrostriction causes deformations of the material due to the presence of an optical field and strain within the material will subsequently modulate the refractive index due to photoelasticity. Additionally, but to much smaller extent, the movement of the boundaries of the silicon beam change the mode frequency by modulating the evanescent field. The mechanical resonance thus shifts the optical frequency ω_c periodically. We capture this in a coupling rate g_0 as

$$g_0 = \left(\frac{\partial \omega_c(x_m)}{\partial x_m}\bigg|_{mb} + \frac{\partial \omega_c(x_m)}{\partial x_m}\bigg|_{pe} \right) x_{ZPF}. \tag{1.1}$$

The proportionality constant is the zero-point fluctuation x_{ZPF} of the mechanical mode which we will discuss below. Analytic expressions for the frequency shifts caused by photoelasticity (pe) and moving boundaries (mb) are given in Ref. [7]. Using these equations, the optomechanical coupling strength can be estimated from finite element simulations using for example COMSOL.

To discuss the optomechanical interaction in detail, we introduce a quantum description of the system [6]. The mechanical mode alone, a harmonic oscillator, is governed by the Hamiltonian of the form

$$\hat{H}_{\mathrm{mech}} = \hbar\Omega\left(\hat{b}^{\dagger}\hat{b} + \frac{1}{2}\right). \tag{1.2}$$

Here $\hbar$ is the reduced Planck constant and $\hat{b}$ ($\hat{b}^{\dagger}$) is the mechanical annihilation (creation) operator defined by

$$\hat{x}_{\mathrm{m}} = x_{\mathrm{ZPF}}\left(\hat{b} + \hat{b}^{\dagger}\right), \quad \hat{p}_{\mathrm{m}} = i\,x_{\mathrm{ZPF}}\left(\hat{b} - \hat{b}^{\dagger}\right) \tag{1.3}$$

Here we use the quantized position $\hat{x}$ and momentum $\hat{p}$ operators. The zero-point fluctuation x_{zpf} of the mode is defined as the spread of the position variable in the quantum groundstate $\langle 0|\hat{x}_{\mathrm{m}}{}^2|0\rangle$ and is given by

$$x_{\mathrm{ZPF}} = \sqrt{\frac{\hbar}{2m_{\mathrm{eff}}\Omega}}. \tag{1.4}$$

It is dependent on the mass of the oscillator, which we define as

$$m_{\mathrm{eff}} = \rho\int d^3x\,|\boldsymbol{q}(\boldsymbol{x})|^2, \tag{1.5}$$

where $\boldsymbol{q}(\boldsymbol{x})$ is the displacement field of the mode normalized to $\max(\boldsymbol{q}(\boldsymbol{x})) = 1$ [7]. Using a numerical solver such as Comsol, we calculate an effective mass of around ~130 fg. We treat the optical cavity in a similar fashion using the Hamiltonian

$$\hat{H}_{\mathrm{opt}} = \hbar\omega_{\mathrm{c}}\left(\hat{a}^{\dagger}\hat{a} + \frac{1}{2}\right), \tag{1.6}$$

where we introduce the creation $\hat{a}^{\dagger}$ and annihilation $\hat{a}$ operators of the optical mode.

With this we can turn to the optomechanical coupling. Expanding ω_{c}, the resonance frequency of the optical resonator, to the first order gives

$$\omega_{\mathrm{c}}(x) = \omega_{\mathrm{c}}(0) + \left.\frac{\partial\omega_{\mathrm{c}}(x)}{\partial x_{\mathrm{m}}}\right|_0 x_{\mathrm{m}} + \ldots \tag{1.7}$$

This can be used with Eq. 1.6 to find the interaction term of the optics and mechanics $\hat{H}_{\mathrm{int}}$ as

$$\hat{H}_{\mathrm{int}} = \hbar g_0\left(\hat{b} + \hat{b}^{\dagger}\right)\hat{a}^{\dagger}\hat{a}. \tag{1.8}$$

We find the single photon coupling rate

$$g_0 = \left.\frac{\partial\omega_{\mathrm{c}}(x_{\mathrm{m}})}{\partial x_{\mathrm{m}}}\right|_0 x_{\mathrm{zpf}}, \tag{1.9}$$

which we can estimate using the photoelastic and moving boundary contributions as in Eq. 1.1 to be on the order of ~1 MHz.

Before writing the full Hamiltonian, we make a transformation into the rotating frame of the laser with frequency ω_{laser} as $\hat{a}_{\text{old}} \rightarrow \hat{a}_{\text{new}} \exp^{-i\omega_{\text{laser}} t}$ (we will drop the index of the operator $\hat{a}_{\text{new}}$ immediately). Frequency components in the Hamiltonian with a detuning $\Delta = \omega_{\text{laser}} - \omega_c$ can then be interpreted as sidebands on the laser. We then get

$$\hat{H}_{\text{full}} = -\hbar\Delta\hat{a}^\dagger\hat{a} + \hbar\Omega\hat{b}^\dagger\hat{b} + \hbar g_0\left(\hat{b} + \hat{b}^\dagger\right)\hat{a}^\dagger\hat{a}. \tag{1.10}$$

Comparing the coupling rate $g_0 \approx 1$ MHz to the loss rates of the mechanical mode $\Gamma << 1$ MHz and optical cavity $\kappa_i < 200$ MHz, we get the hierarchy $\Gamma \leq g_0 \leq \kappa_i$. Since the total optical loss rate κ typically exceeds the coupling g_0 by a factor of almost 10^3, we are deeply in the weak coupling regime and proceed to linearize Eq. 1.10. We first set $\hat{a} = \alpha + \hat{\delta a}$, using a strong, classical drive amplitude α and quantum fluctuations $\hat{\delta a}$. This yields an approximate interaction Hamiltonian according to [6]

$$\hat{H}_{\text{int}} = -\hbar g_0\sqrt{n_{\text{cav}}}\left(\hat{b}^\dagger + \hat{b}\right)\left(\hat{\delta a}^\dagger + \hat{\delta a}\right) \tag{1.11}$$

where we have introduced a real-valued intracavity photon number $\sqrt{n_{\text{cav}}} = \alpha$. A further shorthand notation is to denote $g = g_0\sqrt{n_{\text{cav}}}$ as the optomechanical coupling, which is increased from the single photon coupling rate by the driving strength. Finally, we simplify the notation below by writing only $\hat{a}^\dagger$ for the fluctuating $\hat{\delta a}^\dagger$, consistent with the bulk of literature [6].

We can single out two different types of interactions, depending on the detuning of the optical drive that we employ. Within the sideband-resolved regime and under a blue detuned drive, we can use the rotating wave approximation to set up a two-mode squeezing interaction

$$\hat{H}_{\text{TMS}} = -\hbar g\left(\hat{a}\hat{b} + \hat{a}^\dagger\hat{b}^\dagger\right). \tag{1.12}$$

We can understand this interaction in a three-wave mixing process as shown in Figure 1.2a. Stokes scattering from blue-detuned pulse downconverts the light onto the optical resonance while driving the mechanical mode. We will see in the following section that this two-mode squeezing is an entangling operation on the optical and the mechanical mode.

Red driving on the other hand results in anti-Stokes scattering from the optomechanical cavity as shown in Figure 1.2b. An excitation of the mechanical mode is annihilated and a photon is created at ω_c. Under the rotating wave approximation, Eq. 1.11 results a beamsplitter type interaction

$$\hat{H}_{\text{BS}} = -\hbar g\left(\hat{a}\hat{b}^\dagger + \hat{a}^\dagger\hat{b}\right). \tag{1.13}$$

This Hamiltonian enables an exchange of interactions between the mechanical mode at Ω and the optical field at ω_c. It allows for an efficient state-transfer of the mechanics to the anti-Stokes field, which we will use throughout of the thesis to read out the mechanical modes [6].

1.2.1. PROBABILISTIC QUANTUM STATE PREPARATION

In this section, we will see how the two-mode squeezing interaction together with single photon counting can be used to herald non-classical mechanical states. Eq. 1.12 interaction is linear in the mechanical degree of freedom, and as such is unable to create

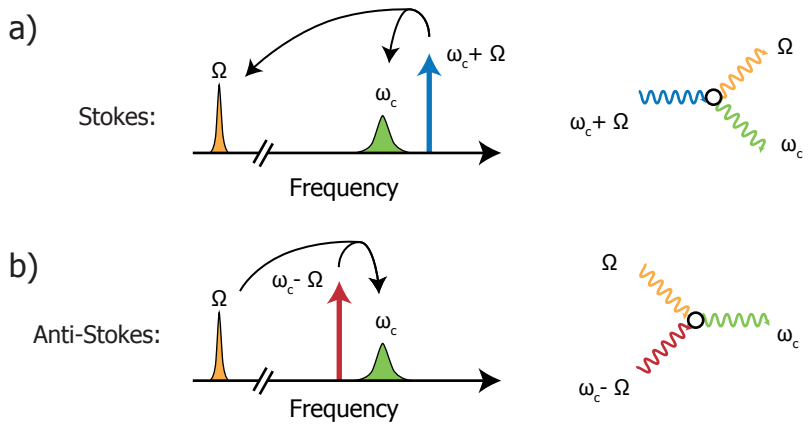

Figure 1.2: Linear optomechanical interactions with a mechanical mode Ω and an optical cavity at ω_c under sideband driving. (a) Blue-detuned driving at $\omega_c+\Omega$ enables Stokes scattering from the optomechanical cavity. This creates pairs of excitations in the mechanical mode Ω and the Stokes field on resonance with the optical cavity ω_c, as described by the two-mode squeezing Hamiltonian. (b) Red-detuned driving at $\omega_c-\Omega$ enables anti-Stokes scattering. Here, excitations are removed from the mechanical mode Ω and up-converted to the anti-Stokes field at ω_c. This interaction is described by the optomechanical beamsplitter Hamiltonian and allows cooling of the mode as well as an optical readout of the mechanical state.

non-Gaussian states starting from an initially Gaussian state (such as the vacuum or a thermal state). We can see this by propagating the state of the mechanics (m) and Stokes field (S) using Eq. 1.12. Assuming both modes are initialized in vacuum states and neglecting a global phase we write

$$|\psi\rangle_{\mathrm{S,m}} = e^{i/\hbar \hat{H}_{\mathrm{TMS}}}|00\rangle_{\mathrm{S,m}} \tag{1.14}$$

$$= \left(1 + i/\hbar \hat{H}_{\mathrm{TMS}} + \frac{1}{2}\left(i/\hbar \hat{H}_{\mathrm{TMS}}\right)^2 + ...\right)|00\rangle_{\mathrm{S,m}} \tag{1.15}$$

$$= |00\rangle_{\mathrm{S,m}} + \sqrt{p_{\mathrm{S}}}|11\rangle_{\mathrm{S,m}} + p_{\mathrm{S}}|22\rangle_{\mathrm{S,m}} + O(p_{\mathrm{S}}). \tag{1.16}$$

Here, p_{S} is the Stokes scattering probability, which in this simplified treatment is given as $p_{\mathrm{S}} = \exp(g_0\sqrt{n_{\mathrm{cav}}}t_{\mathrm{int}})$ with an interaction time t_{int}. Note that a more realistic formula including a thermal background on the mechanical mode and the coupling to the optical cavity is discussed in chapter 3.2.1. We see that by choosing either the intracavity photon number or the interaction time small, we can limit the absolute contribution of the higher order terms in this state. This, however, goes at the expense of creating a state with vanishing total amplitude. The trick is to make use of the non-linearity provided by the measurement on single photon detectors. This can be described by a projection on the subspace containing at least one photon in the Stokes field

$$_{\mathrm{S}}\langle 1| + {}_{\mathrm{S}}\langle 2| + ... \tag{1.17}$$

Applying this projection and tracing over the optical mode, we are left with a mechanical state of the form

$$|\Psi\rangle_{\mathrm{m}} = |1\rangle_{\mathrm{m}} + O(\sqrt{p_{\mathrm{S}}}). \tag{1.18}$$

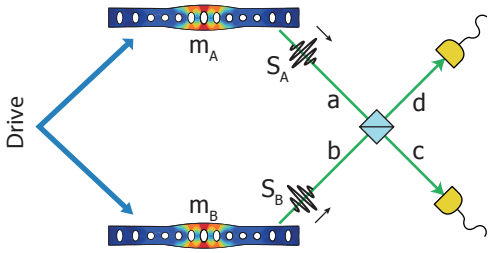

Figure 1.3: Schematic of a Bell state measurement for the single excitation schemes used throughout this work. Simultaneous blue-detuned drives cause Stokes scatting from the two optomechanical devices with a small probability $p_S << 1$ for each each. The two-mode squeezing interaction correlates the excitations in the modes m_A and S_A as well as in m_B and S_B. The Stokes fields are mixed on a beamsplitter which erases all which path information by transforming the input modes a and b to the output modes c and d. A Click on one of the detectors projects the two mechanical modes on an approximately maximally entangled state with one excitation shared between the two. Experimentally, phase stability between the optical paths has to be ensured, which is discussed in chapter 2.2.2

Due to the re-normalization, the dominant component of this state is the single phonon component making it a highly non-classical state. We can in fact choose p_S arbitrarily small and approximate the Fock state as well as we wish. This is, however, at the expense of reduced scattering probabilities which decrease the experimental state preparation rate.

1.2.2. BELL STATE MEASUREMENTS

The second tool from quantum optics that is heavily used in this thesis is a so-called Bell state measurement. It is a joint measurement on modes of two initially separable quantum systems which can induce correlations between them. The scheme is particularly powerful if the modes that are subject to the Bell state measurement are themselves entangled to other modes, which is the basis for quantum teleportation and entanglement swapping. Throughout this thesis we work with single excitation schemes for which this is realized by projecting two optical modes modes S_A and S_B onto Bell states of the form

$$\frac{1}{\sqrt{2}}\left({}_{S_A S_b}\langle 10| \pm {}_{S_A S_b}\langle 01|\right). \tag{1.19}$$

Here $|0\rangle = |\text{vac}\rangle$ indicates the vacuum and $|1\rangle$ indicates a single phonon Fock state. The measurement projects onto a maximally entangled basis, such that no information about the individual subsystems is revealed. Now assume the modes S_A and S_B are entangled with a set of mechanical modes m_A and m_B respectively through the two-mode squeezing interaction. In this case, entanglement can be generated between these extra modes m_A and m_B though entanglement swapping of S_A and S_B, even though they have never directly interacted before. The scheme is shown in Figure 1.3. With equal scattering probabilities for the two beams, we generate the combined two-mode squeezed state as

$$|\psi\rangle \propto \left(|00\rangle_{S_A m_A} + \sqrt{p_S}|11\rangle_{S_A m_A} + O(p_S)\right) \otimes e^{i\phi}\left(|00\rangle_{S_B m_B} + \sqrt{p_S}|11\rangle_{S_B m_B} + O(p_S)\right). \tag{1.20}$$

We furthermore have an additional phase term $e^{i\phi}$, which corresponds to the phase of the light traveling in the interferometer which we experimentally have to keep constant between the trials. After re-ordering the operators and suppressing the higher order term, the state reads

$$|\psi\rangle_{S_A S_B m_A m_B} \propto |0000\rangle + \sqrt{p_S}|1010\rangle + e^{i\phi}\sqrt{p_S}|0101\rangle + O(p_S). \tag{1.21}$$

To implement the Bell state measurement of Eq. 1.19 we mix the two modes on a beamsplitter (see Figure 1.3). After this, the new state is

$$\begin{aligned} |\psi\rangle &= |0000\rangle_{\mathrm{cdAB}} && (1.22)\\ &+ \sqrt{p_S/2}\,(|10\rangle_{\mathrm{cd}} - |01\rangle_{\mathrm{cd}}) \otimes |10\rangle_{\mathrm{AB}} && (1.23)\\ &+ e^{i\phi}\sqrt{p_S/2}\,(|10\rangle_{\mathrm{cd}} + |01\rangle_{\mathrm{cd}}) \otimes |01\rangle_{\mathrm{AB}} && (1.24)\\ &+ O(p_S). && (1.25) \end{aligned}$$

A successful Bell measurement is performed by selecting on measurement outcomes where exactly one photon is found in either of the modes c and d. This corresponds to a projection onto ${}_{\mathrm{cd}}\langle 10|$ or alternatively ${}_{\mathrm{cd}}\langle 01|$. Applying this, we herald a mechanical state of

$$|\Psi\rangle_{\mathrm{AB}} = \frac{1}{\sqrt{2}}\left(|10\rangle_{\mathrm{AB}} \pm e^{i\phi}|01\rangle_{\mathrm{AB}}\right) + O(\sqrt{p_S}). \tag{1.26}$$

The state is either symmetric or anti-symmetric depending on which detector clicks. Note that due to the projection measurement, the vacuum component of the state is gone and the two mechanical modes are left in an approximately maximally entangled state. The two oscillators have never interacted and can in principle be separated far away from each other. This type of measurement is used in chapter 4 and chapter 5 this thesis.

1.3. A MECHANICAL QUANTUM MEMORY

In this thesis, we perform several experiments based on the DLCZ protocol for long-distance entanglement distribution [10]. The original formulation of the protocol was for optically thick clouds of atoms. Nowadays, it has inspired experiments in a whole family of systems, for which we review the state of the art in appendix A. The type of memory required for the protocol combines the storage functionality with the action of a quantum light source to provide the optical states for communication. Generally, a classical control is applied to the device creating light-matter entanglement between the state of the memory and the optical field. In the case of the nanobeams, we can achieve this using the two-mode squeezing interaction, which correlates the mechanical state with the Stokes field. Together with single photon detection, this can then be used to herald highly non-classical mechanical states as discussed in section 1.2.1. Bell state measurements on the Stokes photons of two devices can create entanglement between two mechanical oscillators at a distance as discussed in section 1.2.2. We show this first step of the DLCZ protocol in a minimal network of four memory nodes in Figure 1.4a. Once the Bell state measurements between A and B as well as C and D are successful, the entanglement can be stored in the memory nodes. A red-detuned driving field can

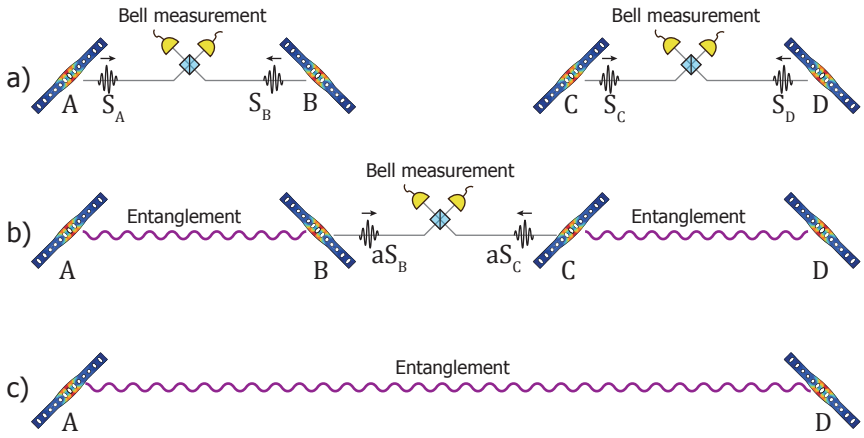

Figure 1.4: a) Blue driving of stationary memory nodes x=A,B,C,D enables Stokes scattering with emission into the respective fields S_x at a small probability p_S. The state of the memories is correlated to the respective fields due to the two-mode squeezing interaction such that a successful Bell state measurement with a click on one of the two detectors emitted from neighboring nodes projects them into a maximally entangled state. Due to losses and necessarily only small excitation probabilities p_S, this process may have to be repeated multiple times. The memory nodes allow to synchronize the attempts and store the successfully generated entanglement. b) A red-detuned driving field allows to optically read out the memories with a high state-transfer probability using the beamsplitter interaction. Entanglement swapping can be achieved by a successful Bell state measurement on the anti-Stokes fields aS_x with, once again, one click in either of the two detectors. c) Swapping of the quantum states of the memory nodes allows to distribute entanglement over longer distances, which can be used for quantum communication protocols between the end-nodes.

be used to retrieve the mechanical states from the memories and to prove the entanglement of the nodes. An entanglement swapping operation can furthermore be used to connect the individual nodes at greater distances [10]. Anti-Stokes fields of neighboring nodes, here B and C, are combined on a beamsplitter and detected on single photon counters, as shown in Figure 1.4b. A detection event projects the remaining nodes, here A and D, onto a maximally entangled state, analogous to the Bell state measurement on the Stokes photons in Figure 1.4a. This entanglement swapping is probabilistic because a successful outcome is conditioned on the registration of one photon in either one of the detectors. Once successful, however, the entanglement can be distributed at further and further distances using the two elementary processes as described above. Losses in the transmission channels only affect the success probability of entanglement generation or swapping but not the fidelity of the memory states. Polynominal scaling of the probabilities with the number of nodes furthermore allows this scheme to outperform a direct transmission for long distances. Subtleties to this protocol and improvements for realistic applications are reviewed in Ref. [11].

Nanobeam mechanical oscillators are in principle well suited for such quantum communication tasks, as they have been shown to host mechanical quality factors that are easily compatible with the requirements for quantum communication. Damping times exceeding milliseconds [7, 12] and even seconds [9], for example, are readily achieved

and would enable to establish quantum links beyond 1000 km. Due to the high frequencies in the Gigahertz regime, they can furthermore be cryogenically cooled to their groundstates eliminating the thermal noise on the mode which in principle enables a high fidelity state preparation. Additional incoherent excitations of the mode due to the optical control fields as well as pure dephasing of the modes must both be limited to achieve this goal and are discussed in detail in the later chapters.
Besides their general suitability, mechanical modes lend themselves for usage as quantum memories due to several advantageous properties. There is an immense design freedom in constructing optomechanical devices because the functionality of the devices is primarily based on their geometry rather than naturally occurring resonances or material properties. Firstly, this means that the optical resonance can be designed at any optical frequency below the bandgap of the host material. This straight-forwardly enables the operation in the conventional telecom band, making them one of the very few memories to operate natively at this frequency range. Multimode mechanical devices can furthermore be envisaged, which could allow for low-overhead multiplexing approaches or relaxed experimental requirements using two-photon protocols [11]. The optomechanical interaction furthermore allows to construct more versatile read-write memories using the optomechanically induced transparency [13] to store optical quantum states from an outside source [14]. As such, mechanical modes could be used in the future as more versatile chip-integrated memories even beyond usage in the DLCZ-protocol, handling short-delay synchronization tasks and long-time storage alike.

The relative freedom of choice of material also in principle enables the integration with integrated silicon photonics components [15], possibly allowing for completely chip based repeater nodes. On-chip integration with superconducting quantum circuits is feasible and under lots of current experimental efforts. Resonant coupling via the piezoelectric effect enables the coherent exchange of excitations between superconducting qubits to the mechanical resonators [16–19] which by itself has been proposed to build electromechanical quantum memories [20]. Alternative approaches are based on capacitive coupling [21, 22]. Efficient interactions with optical as well as microwave frequencies at the same time would allow for converting quantum information between superconducting qubits and telecom photons [23–28]. In such a system, mechanical modes could perform several functions, namely on-demand single photon generation, the up-/down conversion of quantum information between microwave and optical frequencies as well as the storage during the time of flight of the photons.

Beyond practical applications, there is interest in mechanical quantum states because motion is a macroscopic collective quantum variable and in particular because it has an associated mass. Generating macroscopic quantum states such as entanglements and superpositions are excellent tools to explore the physics at the intersection between quantum and classical physics [29]. Experiments have struggled so far to isolate massive systems from their direct environment enough to be able to probe interactions to other source or probe masses in the quantum regime [30]. New types of effects have been hypothesized, for example due to the interaction with gravity [31, 32] or due to other unconventional decoherence mechanisms [33–36]. While the mass of the nanobeams themselves is fairly small [37], successful experiments can still help to develop strategies for future experiments on more massive systems. Achieving precise control over

engineered (i.e. macroscopic) quantum systems is thus crucial for both the progress in fundamental studies of quantum systems as well as for new quantum technologies including quantum memories.

The following work explores the silicon nanobeams as a fully engineer-able quantum memory. Chapter 2 starts by giving an overview on the fabrication and experimental techniques used throughout this work. Chapter 3 goes into detail on the preparation of the mechanical mode into highly non-classical states and explores some of its dynamics. In chapter 4, we build on this and employ a Bell state measurement to generate entanglement between two mechanical modes on two separate chips. Chapter 5 explores the entanglement in more detail and gives a benchmark in the form of a Bell inequality violation. Finally, in chapter 6, we explore the ability of our memory to store various quantum states for extended time periods.

2

EXPERIMENTAL TECHNIQUES

Here we discuss the experimental techniques of chapters 3-6 as well as others, which were developed but ultimately not used in published research yet. Some of the techniques are more common, such as laser or interferometer locking techniques. Others are tailored towards working with the optomechanical crystals, like fiber coupling with optical access in a dilution fridge. While it is expected that some of the techniques will be refined in the future and others will be added, the following is a snapshot of the current state of the experimental capabilities and meant as a reference for experimentalists.

2.1. FABRICATION

The fabrication of the silicon nanobeams is adapted from Ref. [7] with changes due to differences in the cleanroom capabilities. We start off with a silicon-on-insulator wafer (Soitec) with a 250 nm silicon layer on top of 3 μm buried oxide. The patterns are written using a Vistec EBPG5200 ebeam writer and CSar09 resist. We develop the exposed pattern for 1 min in pentyl-acetate, stop the development in a 1 min bath in 1:1 MIBK:IPA before a final IPA rinse. The dry etching of the devices is done using SF_6O_2 chemistry in an inductively coupled plasma etcher (Oxford Instruments). The devices are written in the center of the chips. Access to the waveguides in plane is achieved by dicing within 15 μm of the waveguide tips. After this step, the resist in cleaned in 80°C di-methylformamide before moving to the inorganic etching. Here we typically use a combination of a cleaning / oxidation step and isotropic oxide etching with hydrofluoric acid. The first step involves inorganic cleaning of the chips in either a piranha or with the RCA method. No conclusion has been found so far as to which method produces better results, tests have been performed in Refs. [38, 39]. The Piranha consists of heating sulfuric acid to 80 °C and adding hydrogen peroxide in a 3:1 ratio. The mixture heats up well above 120 °C, which provides good cleaning of the silicon as well as oxidation. The RCA method is the standard method [40]. Afterwards, the devices are undercut for 3:30 min in 36% concentrated hydrofluoric acid. Typically, a second round of either Piranha or RCA cleaning followes, after which the formed oxide is etched away in 1 % hydrofluoric acid. The idea is that consecutive oxidation of a few nanometers of the surface of the silicon and etching of this oxide can smoothen the surface. Additionally, the last etching step with hydrofluoric acid step can terminate the surface of the silicon with a hydrogen passivation layer which can, in principle, protect the devices against oxidizing in ambient conditions until they can be mounted in the cryostat. While full wafers can be protected against oxidation for up to days, it is questionable how long the termination can last on the fully processed chips (see also Ref. [41]). We therefore try to keep the exposure times as small as possible before mounting the devices in the fridge.

2.1.1. DEVICE COUPLING

We couple to the devices via an optical waveguide on the silicon chip as shown in Figure 2.1a. Three different coupling strategies to the waveguide itself were explored during this thesis. The first and most widely used coupling is done with commercially available lensed fibers (Figure 2.1a). We use fibers with a focal distance of 14 μm where they simply focus the light onto the waveguide tip by moving the fibers with nanopositioner stages, as shown in Figure 2.2. Our current chip design allows for single pass couplings of up to ~70%. The devices have to be placed at the edge of the chip with the waveguides facing outwards, which is achieved with the dicing step in the fabrication. The fiber coupling can easily be used in the dilution fridge, since it does not require optical access. As the fiber is approached, a small optical interferometer is formed between the fiber tip and the side of the chip. The free spectral range of this interferometer which can be measured by scanning the laser makes it possible to estimate the distance to the chip. The upper edge is easily found moving upwards until all reflection is lost. Finally, device coupling is achieved by moving a bit left and right until the waveguide reflection is found, whereas the reflection from the waveguide clearly exceeds the reflection from the chip sidewall.

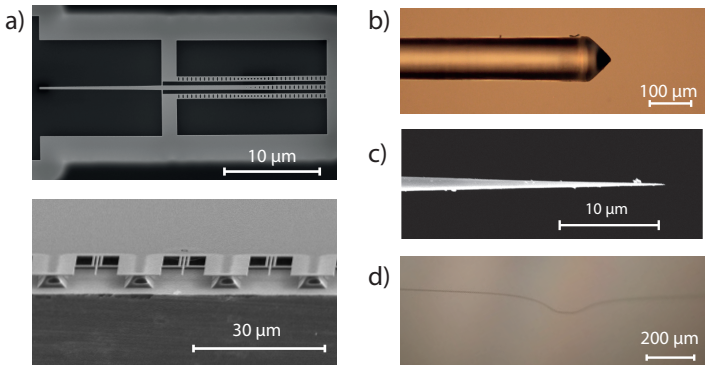

Figure 2.1: a) Scanning electron microscope images of the devices with the waveguides used for coupling at the edge of the chip. On the top is an image of two nanobeams on the two sides of a center waveguide extending to the left. Below is a view from the side, depicting the typical placement of multiple devices at the edge of the chip. b) Microscope image of a lensed fiber, the most common coupling method used throughout this work. Coupling with is done by aligning fiber focal spot 14 μm in front of the fiber to the tip of the device waveguides. This coupling method necessitates the placement of the devices at the edge of the chip, where the alignment to the waveguides can be done without optical access as described in the text. c) Scanning electron microscope image of a tapered fiber. Coupling is done by placing the fiber on top of the waveguide such that evanescent coupling is enabled (see also Figure 2.2). Efficiencies exceeding 90% can be achieved using this method. d) Microscope image of a dimpled fiber. Coupling is done by placing the dimple on top of the waveguide for evanescent mode coupling. While high efficiencies of more than 90% can be achieved using this strategy, optical access to align the dimple is strictly necessary.

More details on the technique for reliably approaching the device waveguides without optical access can be found in Ref. [42]. During all experiments presented in this thesis, the lensed fiber coupling was employed. Nevertheless substantial amounts of work were put into developing more efficient, fridge compatible coupling strategies.

Coupling via so called dimpled fibers was investigated as an alternative to the lensed fibers. The strategy was developed in stages in Caltech, starting with direct coupling (e.g. Ref. [7]) and later incorporating a waveguide [43]. The fibers themselves are tapered while heating them with a hydrogen torch and pulling until the diameter drops below 1 μm [44]. Afterwards a so called dimple is formed by pressing the hot fiber against a sapphire fiber. We have achieved coupling efficiencies exceeding 95 % in a room temperature test setup. Two main drawbacks of this coupling strategy is that the fiber alignment requires optical access and that the coupling can be quite unstable, as the fibers tend to be long. Ultimately, the dimpled fibers were thus abandoned.

The third technique for fiber coupling is based on single-sided tapered fibers, which can be produced by etching a standard SMF28 fiber in hydroflouric acid [45]. Details on the process can be found in Ref. [42], and a picture of a pulled fiber is shown in Figure 2.2. Coupling is achieved by evanescent mode coupling between the fiber and the waveguide [43]. Efficiencies exceeding 90 % have been achieved in our lab, whereas coupling to the waveguides without optical access can be done similarly to the lensed fibers [42].

Figure 2.2a shows a sketch of our standard setup without optical access inside the fridge. It was used in all later chapters of this thesis. A lensed fiber is mounted on a

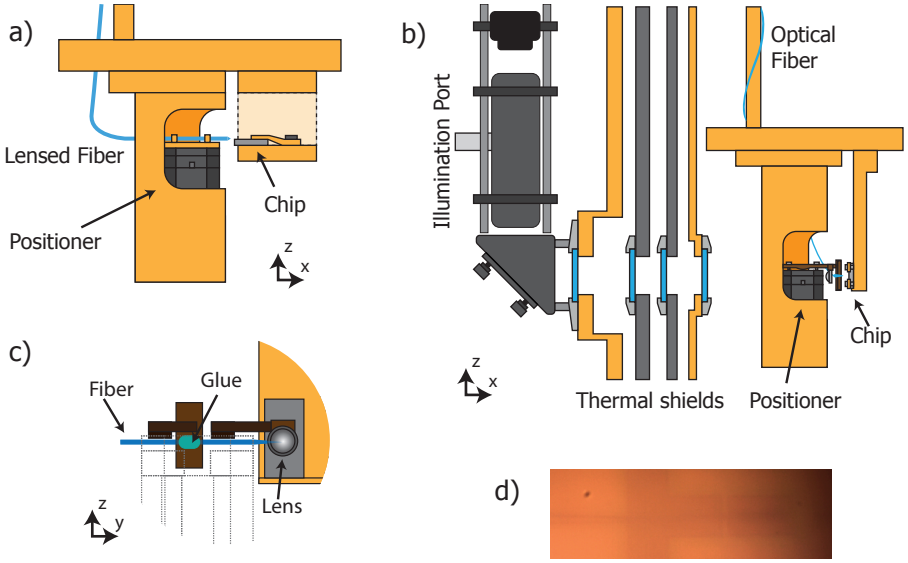

Figure 2.2: a) Sketch of the standard microscope setup for fiber coupling in the fridge. Lensed or tapered fibers are mounted on top of a nanopositioner stack with which they can be aligned to different device waveguides. The chip is mounted in the xy-plane with the waveguides at the side of the chip facing towards the fiber. b) Sketch of the setup including optical access through windows in the vacuum can and thermalization shields. All three fiber types can be mounted with different holders on top of a nanopositioner stage with which they can be aligned to the device waveguides. The microscope focus can be adjusted using a telescope tube outside of the cryostat. c) Close-up of the chip with orientation as seen through the microscope. A small lens on top of the positioner is used to focus onto the fiber, which is coming from the left side. The chip is mounted in the yz-plane with the waveguides facing to the left, however, the devices do not necessarily have to be at the edge of the chip. d) Microscope image with a successfully coupled tapered fiber. The image sharpness is more than sufficient, whereas the image contrast can be improved in the future using an illumination source inside the cryostat.

movable piezo stack (Attocube) facing a chip with the waveguides at the edge, such that different devices can be coupled even at cold temperatures. In Figure 2.2a, we show a setup including optical access which was developed but ultimately not yet used for published experiments. The optical access is achieved though windows in the thermal shields of the fridge which can be purchased as an option from Bluefors. The microscope itself can be mounted on the outside of the fridge. It uses a telescope tube, through which the illumination light can be injected, and CCD camera. The fiber tip is centered at a fixed distance in front of a small lens with focal length of 1.4 mm, which moves together with the fiber. The microscope focus is adjusted in the telescope tube outside the fridge. Figure 2.2 shows an example image which was used to successfully couple to a device in the center of the chip. The image sharpness is quite good considering the total length of the microscope, although the contrast is somewhat low. The light passes the four windows in the thermalization shields of the fridge before it reaches the device which results in lots of back reflections. A straight forward improvement would be adding a light source inside the fridge, e.g. LED light that is routed to the base of the fridge through an optical fiber [44].

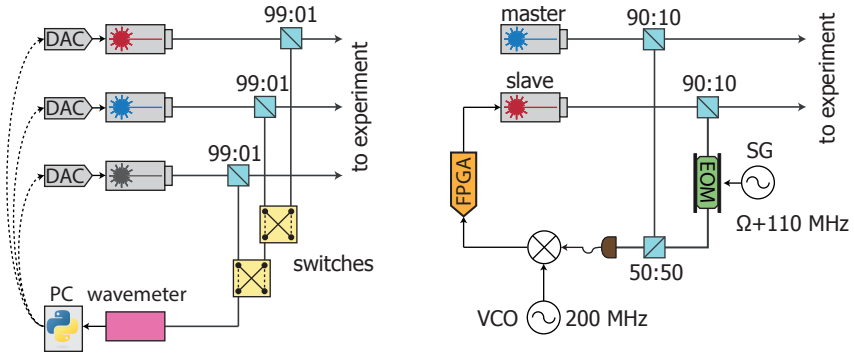

Figure 2.3: (a) Schematic of the wavemeter locking, where multiple lasers can all be stabilized to a single wavemeter. Python scripts handle the switching of the wavemeter input as well as the feedback to the lasers. (b) Schematic of the beat-locking where a master laser is stabilized to a wavemeter whereas the slave laser is is stabilized to the beatnote between the two lasers. Note that both lasers need to be stabilized offset from the respective mechanical sidebands by $\omega_{\mathrm{AOM}}/2\pi = 110$ MHz, as they are frequency shifted later on by an accousto-optic modulator. We create sidebands on the red-detuned laser using an electro-optic modulator (EOM) driven with a signal generator (SG) at $\Omega + \omega_{\mathrm{AOM}})/2\pi$. The beatnote between the first order sideband and the other laser has thus to be stabilized at 220 MHz to ensure correct detunings. We detect this signal on a photodiode with 360 MHz bandwidth and further mix it down electronically using a voltage controlled oscillator (VCO) at 200 MHz. The feedback is generated using a redpitaya with a 60 MHz analog to digital bandwith.

2.2. EXPERIMENTAL SETUP

The experiments presented in the following are all carried out with variations of the same principal setup. While the setup (including all control code) was built in Delft, the general layout and some of the techniques were developed earlier by Ralf Riedinger and Sungkun Hong in the University of Vienna.

2.2.1. PULSE GENERATION AND LASER FREQUENCY NOISE

The protocols used in the following employ laser pulses with a specific detuning of plus and minus the mechanical frequency Ω from the optical resonance frequency ω_c. We generate the light from two continuous-wave external cavity diode lasers. The locking of the lasers to the respective frequencies differes slightly throughout the experiments and the following description refers to chapters 5 and 6. Here, a wavemeter (Angstrom) is used to monitor the laser frequencies and a software controlled feedback loop actuates the laser piezo. To synchronize the locking for two or more lasers, a python script was developed together with Beverly Lee to account for multiple users as shown in Figure 2.3a. Optical switches (JDSU) are toggling the input of the wavemeter. The script handles multiple instances of the laser locking programs and assigns measurement slots for each of them. Slots of 1 s are assigned to each laser during which it gets the reading of the wavelength with the refreshing rate of the wavemeter of 50 Hz. This stabilization techniques allows to stabilize the lasers at any absolute frequency and compensate for slow, longterm drifts. The linewidth of the beatnote between two lasers of chapter 6 is measured to be ~2 MHz. This is sufficiently smaller than the typical bandwidth of the

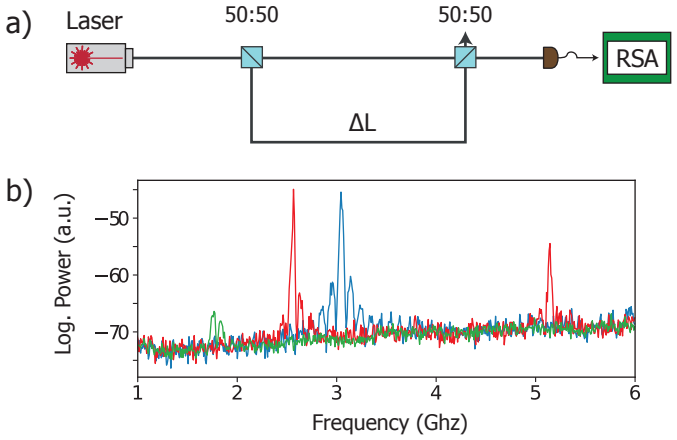

Figure 2.4: a) Setup to detect GHz phasenoise peaks in the lasers used in the experiments. An unbalanced Mach-Zehnder interferometer with path-length mismatch $\Delta L \approx 1$ m resulting in a free spectral range around 100 MHz is used to convert the phase fluctuations into amplitude noise at the output. It is detected on a photodiode with 10 GHz bandwidth and analyzed on a real-time spectrum analyzer (RSA). b) Noise spectra of three of the lasers used throughout of this work, all measured with 5 mW optical power: Santec TSL550 (blue), New Focus TLB-6700 (red) and Toptica CTL 1500 (green).

pulses of ~30 MHz and is thus not affecting the interference visibility in the experiments.

While the frequency stability in the above locking technique is sufficient, it was found that small inaccuracies of the wavemeter could introduce an offeset in the laser frequencies. Locking two lasers to the wavemeter individually with a detuning of twice the mechanical frequency (around 10 GHz) can introduce offsets from this setpoint in the range of a few MHz. An improved locking technique was developed partly with Ian Yang. The idea is to lock only one of the lasers, the master, to the wavemeter and stabilize the other one, the slave, using the beatfrequency between the two. To reduce the required bandwith of the photodiode, it is useful to shift the beatnote down to the MHz regime before detection. We use an electro-optic modulator driven at approximately the mechanical frequency to optically shift the frequency to 220 MHz before detection and electronically further mixed down to 20 MHz as shown in Figure 2.3b. The feedback loop was implemented on a FPGA (redpitaya) with the pyrpl software package [46], using a FPGA frequency comparator and PID. Due to the fast bandwith of the ADC of 60 MHz, this setup could in principle be used to reduce the beating linewidth of the lasers by current modulation of the laser diode.

The lasers used throughout the experiments are external cavity diode lasers from different manufacturers (Santec, New Focus and Toptica). It is known that these lasers can have pronounced phase noise peaks in the Gigahertz regime due to relaxation processes of the gain medium [47]. We show measurements of this noise for three of the lasers used throughout this work in Figure 2.4. Such noise can disturb the experiments by producing false detection events if the noise frequency matches the mechanical frequency of the nanobeams. In the setup for the pulsed experiments as shown in Figure 2.5, we employ fiber filters (MicronOptics) with ~50 MHz bandwidth to suppress these fluctua-

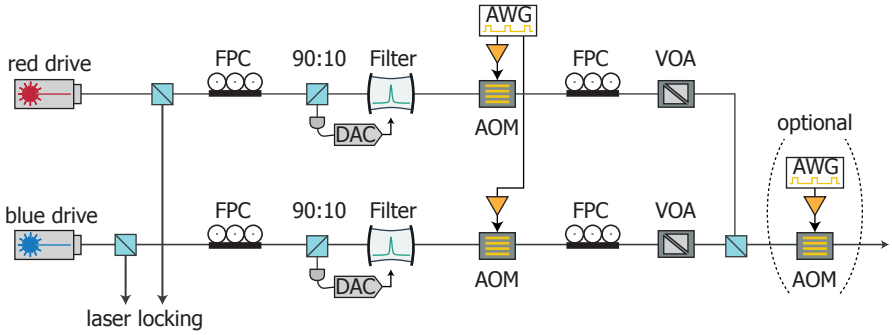

Figure 2.5: Schematic of the setup for the pulse generation. Two continuous-wave lasers are used to generate the pulsed sideband drives for the optomechancial device. We filter GHz noise on the lasers using two fiber optical filters with ~40 Mhz bandwidth, which are stabilized by collecting parts of the reflected light and providing feedback via a python script. The pulses are shaped using two 110 MHz accousto-optic modulators (AOM) which are driven by an arbitrary waveform generator (AWG). A third optional AOM can be used to gate the pulses for a better on-off ratio. We note that each AOM causes a frequency up-shift of the lasers, which is compensated during the laser stabilization in section 2.1.1. The polarizations of the two lines are aligned using fiber polarization controllers (FPC) and their powers are adjusted using a variable optic attenuator (VOA).

tion. To lock the filters, we use 90:10 fiber couplers in front of the cavities to detect the signal in reflection. The photodiodes are read by digital to analog converters (DAC) such that feedback can be applied from a python script. The lock is implemented by constantly scanning the resonance with small amplitude (ca. 20% of the FWHM of the filter resonance) such that drifts can be detected and compensated.

After this filtering step, we create optical pulses using two 110 MHz AOMs (Gooch & Housego) as also shown in Figure 2.5. The pulse shapes are programmed onto either an AFG (Tektronix) ar AWG (Agilent) and amplified using RF amplifiers (Minicurcuits). We typically use pulses with a Gaussian shape with FWHM of 30–40 nsec. Leakage through the AOMs while in the off state causes latent absorption heating in the devices. The AOMs have a suppression of roughly 60 dB, which is enough when working with devices with modest mechanical ringdown times below 100 μs. In devices with large mechanical quality factors, however, this leakage causes measurable absorption heating because more and more photons are passing during the lifetime of the mechanical mode. For the experiments of chapter 6, a third AOM is used to gate the pulses for an improved on-off ratio.

2.2.2. INTERFEROMETER LOCKS

For all experiments involving Bell state measurements, we require optical interferometer with a stabilized roundtrip phase. Phase fluctuations up to a few hundreds of Hertz are normal in the fiber interferometer and can easily be locked. Additionally, fast noise from the pulse-tube is picked up by the fibers inside the fridge. We use a homemade fiber stretcher to apply a kilohertz feedback to the interferometer phase (for details see Ref. [48]). As seen in Figure 2.6b, the Piezo has a resonance around 25 kHz, which sets an upper limit for the feedback bandwidth. Using a high voltage amplifier (Falco), we are able to induce phase-shifts exceeding $10 \times 2\pi$. The error signal for the lock is generated

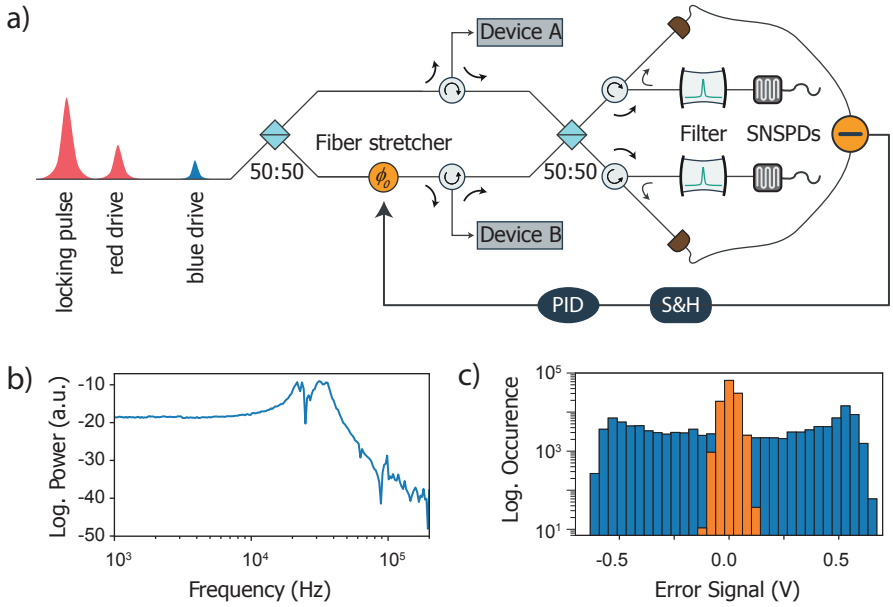

Figure 2.6: (a) Schematic of the interferometer locking technique used in chapters 4 and 5. We typically insert strong locking pulses after the experimental drives such that the absorbtion of those pulses in the device does not affect the experiments. The error signal is taken from the reflected light from the detection cavities on a balanced detector. A sample and hold (S&H) board is used to pick the pulse signal and feedback is applied from an FPGA board (redpitaya) to a home-built fiber stretcher. Note that while the most of the setup is in fiber, circulators, filters and balanced detector in the detection path are implemented in free-space optics as described in Figure 2.7. (b) Transfer function of the fiber stretcher measured using a vector network analyzer by detecting the optical modulation on the balanced detector. A resonance above 20 kHz is seen, which ultimately limits the feedback bandwidth. (c) Histogram of the noise in a free running (blue) and a locked (orange) interferometer.

by reflection of the light on the filter cavities in the detection arms (see section 2.2.3). Conveniently, the error signal can in principle be generated from the reflected optical drives themselves or by adding an additional locking pulse, without the need to emply additional light for locking. The optical setup to do this is schematically shown in Figure 2.6a whereas a detailed implementation of the circulator and filter in the freespace detection setup is shown in Figure 2.7). We use a balanced detector (Thorlabs, bandwidth 70 MHz) connected to the two output ports of the interferometer to be insensitive to power fluctuations. The feedback electronics were partially developed in Vienna using a FPGA board (redpitaya) and a sample and hold board (S&H) to pick the voltage on top of the pulse. In chapters 4 and 5, a locking pulse generated from the red detuned laser is injected into the interferometer after the experimental pulses. As such, the feedback is limited to the repetition rate of the experiment at most. This is sufficient for devices with modest damping times in the microsecond regime, for which repetition rates above ~10 kHz can be used. In other experiments (e.g. chapter 6), an off-resonant beam was injected into the interferometer as there was no device inside. In this case, a quasi-continuous locking can be used which can increase the locking bandwidth up to

the resonance of the piezo tube. The error signal of a locked and an unlocked interferometer is shown in Figure 2.6c. We typically achieve RMS phase stabilities up to $\pi/25$ (see also chapter 5.5.1).

2.2.3. DETECTION

The detection lines in all experiments include a set of two narrow optical filters with linewidths around 40 MHz to remove the reflected optical drives from the detected fields. In chapter 4, a fiber-based setup with two commercial filters (MicronOptics) was used. Here we focus on the freespace setup used in chapters 5 and 6 which was developed partly in Ref. [49]. The main reason to use freespace cavities is to reduce insertion losses of the commercial fiber filters. A sketch with the layout of the freespace setups is shown in Figure 2.7. The cavities are designed to have free spectral ranges of 18 - 19 GHz at 1550 nm wavelength, corresponding to a length of 8.3 mm and 8.8 mm between the two mirrors. The length is defined by the aluminum housing (see inset in Figure 2.7). One of the lenses is mounted on a piezo tube, such that the cavity resonance can be scanned and parked at the required frequency. The input voltages of ± 10 V are directly derived from a NI-DAQ card. The reflectivity of the mirrors is chosen to be 99.3%, resulting in a Finesse of ~450 or a FWHM filter bandwith of ~40 MHz. Each filter setup contains two cavities, resulting in an expected suppression of >80 dB for light that is detuned by 5 GHz from one of the resonances. Given that a typical readout pulse during the experiments contains around 100k photons after being reflected from the cavities, we expect less than one photon per 1000 trials to leak through the cavities. Given the optomechanical interaction strengths and setup efficiencies, this typically results to about one leaked photon in ten optomechanically detected ones (see chapters 5 and 6). Adding a third cavity, even with much lower finesse, could reduce this in future experiments.

As shown in Figure 2.7, light from the device is coupled from a fiber collimator and passes a telescope to adjust the beam-waist for matching to the cavity. A mode matching lens focuses the light into cavity 1, details of which can be found in Ref. [49]. The error signal for cavity locking is generated from the light that is reflected from the cavity. After passing PBS1, the linearly polarized beam is changed to a circular polarization with the half-wave plate. Light that is reflected from the cavity performs a second polarization rotation back to linear polarization, this time only 90 degrees off the input orientation. As such it is now reflected from PBS1 and can be detected on a photodiode. Resonant light is transmitted through the cavity, after which it is collimated and its polarization is aligned to PBS2. The second cavity works exactly as the first one, whereas the error signal for locking is now generated on another photodiode. Finally, light that is transmitted though both of the cavities is mode-matched to the output coupler. Continuous-wave transmission efficiencies exceeding 90% though all freespace components are achieved by proper mode matching to the cavities. The main source of loss of the filter setup as a whole is the coupling back into the fiber. Typical efficiencies that were achieved are around 70% on both of the filter setups.

The filters cannot be continuously locked during the measurements, since any light that passes the cavities is detected on the SNSPDs and cannot be distinguished from the optomechanically generated fields. We therefore do not continuously stabilize the filters but rather pause the measurements every 5 seconds to reset the cavities to the

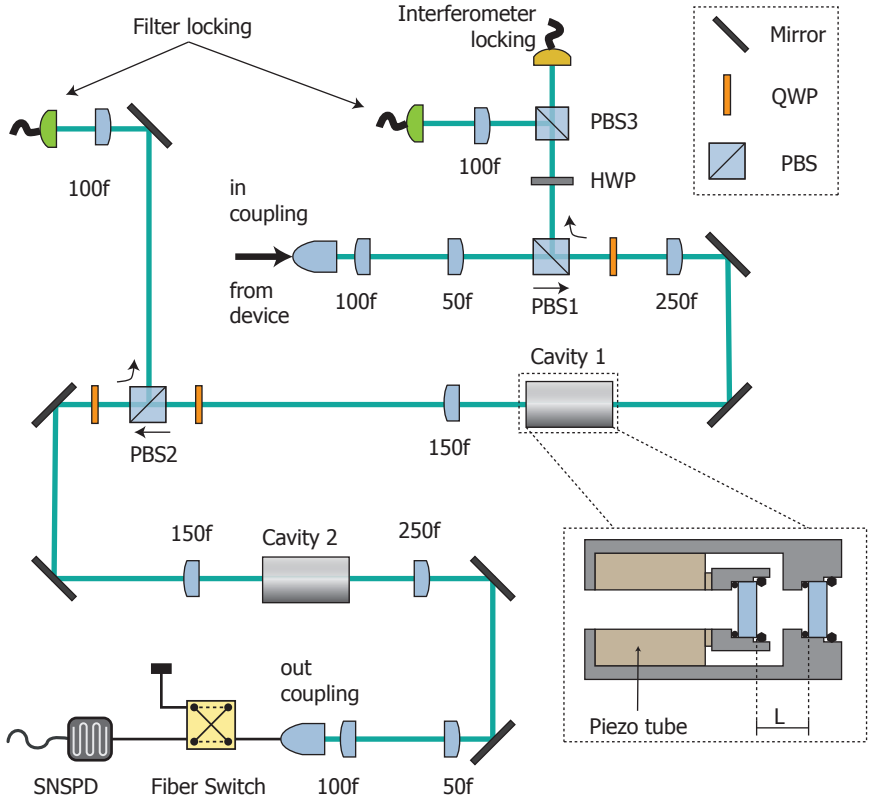

Figure 2.7: Freespace filter setup in the detection path. Light is coupled from a fiber collimator and mode matched to the first filter cavity. The beam passes a polarizing beam splitter (PBS) and a quarter-wave plate (QWP), which together act as a circulator. The light reflected from the off-resonant cavity can be detected on a photodiode (green) with minimal losses, such that the cavities can be tuned to resonance. By aligning the polarization to PBS2 using a half-wave plate (HWP), a part of the light can be routed to one of the inputs of a balanced detector (yellow) which is used to lock the phase of the interferometer in the entanglement experiments. The second input is done in the same way in the second filter setup (see also section 2.2.2). A second cavity is used to increase the overall suppression of the optical drives before the light is finally coupled back into fiber. An fiber-optic switch is used to block the light during re-alignment of the filter cavities and is switched to transmit to the superconducting nanowire single photon detector (SNSPD) during the measurement.

correct setpoint. The error signal is measured in reflection from the cavities as shown in Figure 2.7 and feedback is applied though python software. If the reflected intensity is below 5% of the off-resonant reflection, the cavity is said to be locked and no action is taken. If it is just slightly higher but is still within 25%, the filters are stepped left and right using a small optimization algorithm to find the correct setpoint again. Only if the power is off by more than 25%, the filters are scanned and the full resonance is recorded such that the correct setpoint can be found again. The filter transmission typically stays above 80–90% during the 5 sec of measurements and the re-scan is seldom performed. Scanning the cavities typically results in much faster drifting of the resonances after-

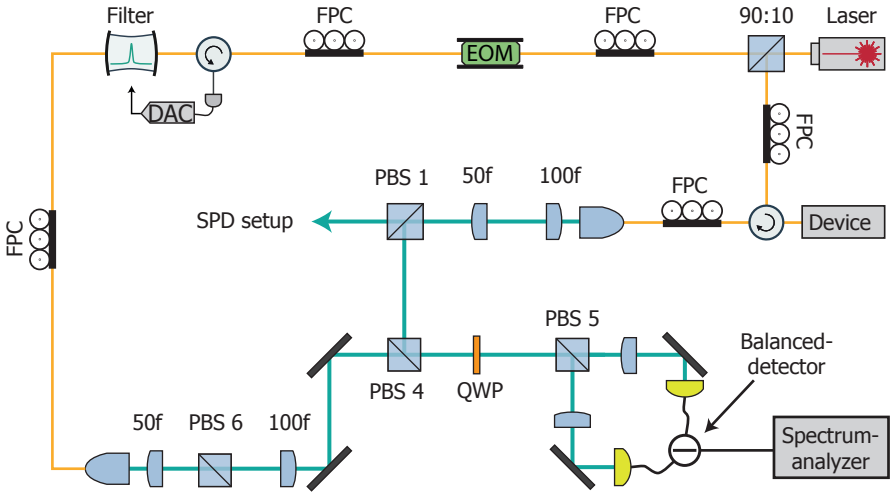

Figure 2.8: Sketch of the heterodyne setup, which is an option in one of the filter setups. The generation of the local oscillator (LO) is in fiber (yellow), whereas the actual detection setup is free-space (green). The laser is stabilized with either red or blue detuning from the device, such that the LO can be generated in an electro-optic modulator (EOM) by driving at the approximate mechanical frequency. A fiber filter is used to select only the sideband with correct detuning. Fiber polarization controllers (FPC) are used to align the polarization of the light to polarization sensitive devices, which include the polarizing beamsplitters (PBS). Note that PBS1 is the same as in Figure 2.7 where the optical path of the SPD setup is shown. The signal is aligned with the local oscillator on PBS2 and after a polarization rotation with the quarter-wave plate (QWP) interfered on PBS3.

wards. The main goal is therefore to move the cavities as little as possible during each cycle to keep them as stable during the measurement interval. The two filter cavities are aligned after one another, whereas the locking of the two filter setups is done in parallel. Re-locking of the two filter lines with two cavities each takes takes on average 0.7 sec including switching of the optical path, hence it consumes ~15% of the total measurement time.

2.2.4. HETERODYNE MEASUREMENTS

One of the filter lines has an additional heterodyne setup for measurements of the mechanical linewidth. As shown in Figure 2.8, the light from the device can either be routed towards the SPD setup, Figure 2.7, or to the heterodyne detection by alignment of the polarization to PBS1. Here, it is mixed with a local oscillator which is generated from the same laser as the one used to interrogate the device. We shift the frequency by generating optical sidebands with an EOM and select the one with correct detuning using a fiber filter. We typically apply a frequency offset between the local oscillator and the optomechanical sideband of ~5 MHz. The mixing of signal and local oscillator is done using PBS4 and PBS5 with a quarter wave plate in between to be able to precisely adjust the splitting ratio. The detection is done on a home-built balanced photodetector with a bandwidth of ~30 MHz. The mechanical frequency and linewidth can be evaluated on a spectrum analyzer.

3

HERALDED MECHANICAL QUANTUM STATES

The optomechanial two-mode squeezing interaction correlates the number of excitations in the mechanical mode and the Stokes field. Detecting the Stokes photons on highly efficient single photon detectors can herald the mechanical mode close to a single phonon Fock state. A reliable preparation of such states is both of interest for testing quantum mechanical predictions on collective degrees of freedom as well as to develop new quantum technologies. Here we discuss such an experiment step-by-step, starting with a characterization of the device after being cryogenically cooled to the motional groundstate. We measure the cross-correlation of Stokes and anti-Stokes fields from the device and discuss the requirements that it attains non-classical values. We finally probe the quantum nature of the mechanical mode directly by performing a Hanbury-Brown and Twiss measurement on the anti-Stokes field.

Parts of this chapter have been published as *Hanbury Brown and Twiss interferometry of single phonons from an optomechanical resonator.* S. Hong, R. Riedinger, I. Marinković, A. Wallucks, S. G. Hofer, R. A. Norte, M. Aspelmeyer, and S. Gröblacher. Science **358**, 203 – 206 (2017)

3.1. CW DEVICE CHARACTERIZATION

This first section describes measurements that are performed to characterize a device before the actual quantum experiments. Once the fridge is cooled to 4 K or below, we select a device using the fiber coupling methods described in chapter 2.1.1. The optical resonance frequency of the structure is found using a wavelength scan with a continuous probe laser as shown in Figure 3.1. Fitting the device response with a Lorentzian function lets us extract the FWHM loaded linewidth κ. This linewidth is composed of the intrinsic linewidth κ_i and the external coupling κ_e to the coupling waveguide as $\kappa = \kappa_i + \kappa_e$. These two can be separated from the ratio of resonant and off-resonant reflected power P_0 and P_∞ as [50]

$$D = \frac{P_0}{P_\infty} = \frac{(\kappa/2 - \kappa_e)^2}{\kappa^2/4}. \tag{3.1}$$

Critical coupling with $\kappa_e = \kappa_i$ is thus indicated by a depth D approaching zero. For non-zero D, there is an ambiguity in the amplitude response of Eq. 3.1, such that the cavity could either be under coupled $\kappa_i > \kappa_e$) or overcoupled $\kappa_i > \kappa_e$. The coupling strength is defined in the design of the cavity [42] and, although it is subject to fabrication imperfections, can therefore in most cases be distinguished. In the cases the ambiguity cannot be resolved by relying on the expected coupling regime, the phase response of the cavity can be measured [43] revealing much larger phase jumps in the overcoupled regime. Slightly overcoupled devices are generally favorable since this results in an increased collection efficiency of the optomechanically scattered photons into the waveguide. The amount of external coupling κ_e has to be limited, however, such that the device remain is the sideband resolved regime $\kappa << \Omega$.

Additionally, the coupling of the fiber to the waveguide η_{fc} for a given device is determined by reflecting off-resonant from the device and measuring the reflected power (see also chapter 2.1.1 for the coupling strategies). While not a performance metric of the device itself, it is one of the most variable parameters for the detection efficiency and thus the expected measurement times.

Besides the spectroscopy of the optical mode, the mechanical mode can be detected and characterized under continuous driving. A direct detection of the optomechanically generated sideband is possible by stabilizing the drive on the red or blue sidebands of the cavity in the setup of Figure 3.1. The reflected light is amplified in a erbium-doped fiber amplifier (Amonics), detected on a fast photodiode (EoT) and analyzed on a real-time spectrum analyzer (R&S). This measurement is relatively easy to perform and and fully sufficient to find the resonance frequency of the mode. It is, however, only of limited use for analyzing the mechanical linewidth due to its poor sensitivity. As such, the mechanical line is often only seen when driving the device close to or at the mechanical lasing threshold [6]. An alternate scheme is a heterodyne measurement, where the optomechanical sideband is amplified by a frequency shifted strong local oscillator and detected on a balanced photodiode with reduced bandwidth (see chapter 2.2.4). A much higher gain at lower technical noise figures is possible leading to far superior sensitivity, allowing in principle more accurate studies on the mechanical linewidth. Another approach that can be used is a measurement of the optomechanically induced transparency (OMIT). This techniques is a two-tone spectroscopy where the mechanical mode itself is coherently driven by the beatnote of a strong pump and weak probe

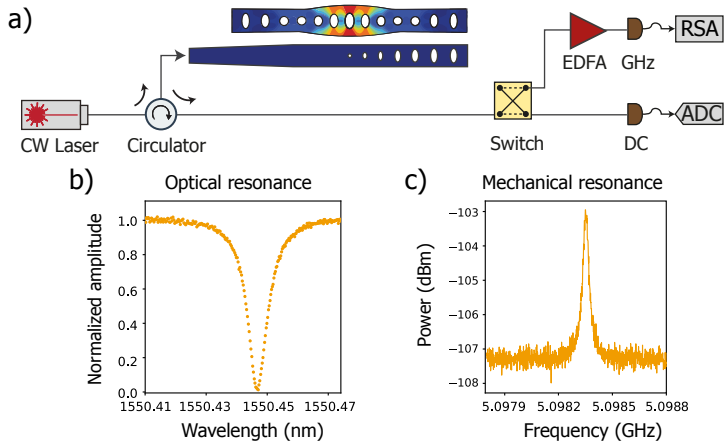

Figure 3.1: a) Optical setup for the characterization of the device under continuous wave (CW) driving. The optical switch routes the reflected light either to a low bandwidth photodiode (DC), which is read out by an analog to digital converter (ADC), or via an erbium doped fiber amplifier (EDFA) to a high speed detection setup (GHz) where the mechanical sideband can be detected on a real-time spectrum analyzer (RSA). b) A scan of an optical resonance to determine the cavity frequency ω_c with the background level normalized to one. The width and the depth of the resonance are used to determine the intrinsic linewidth κ_i and external coupling rate κ_e as described in the main text. Shown is a roughly critically coupled device with $\kappa_i \approx \kappa_e$. c) A direct measurement of the mechanical sideband used to determine the mechanical resonance frequency Ω. The data in b) and c) is taken from Ref. [51].

tone [13]. Finally, the mechanical resonance can also be detected by monitoring the clickrates on the single photon detectors while sweeping the filter cavities in the detection arm (see SI chapter 4)). Since the resulting lineshape is a convolution with the filter response, only limited information about the mechanical lineshape itself can be gained.

3.2. PULSED DEVICE CHARACTERIZATION

The following section describes the characterization of the devices using optical pulses. An overview of the setup used here is shown in Figure 3.2, whereas details on the individual parts can be found in chapter 2.

3.2.1. OPTOMECHANICAL COUPLING RATE

While the optomechanical coupling rate g_0 can be measured under continuous wave driving using the optical spring effect [6], we typically resort to a pulsed scheme. The general idea is that the optomechanical coupling strength can be extracted from the Stokes and anti-Stokes scattering probabilities p_S and p_{aS} after the detection efficiencies are calibrated. We note that $n_{phot} = E_p/\hbar\omega$ is the number of photons in an optical pulse with Energy E_p at frequency ω. The intracavity photon number under a detuning of Ω is given by $n_{phot}\kappa_e/(\Omega^2 + (\kappa/2)^2)$ where κ and κ_e are again the total and the external loss rates of the optical cavity. In the limit of $p_S, p_{aS} \ll 1$, we can explicitly write the

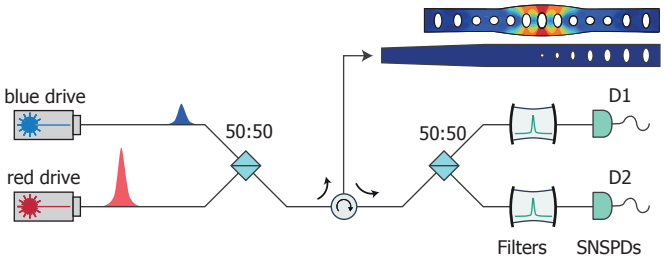

Figure 3.2: Setup for the pulsed device characterization and heralded preparation and detection of a single phonon Fock state. Blue and red-detuned drives are pulsed, as described in chapter 2.2.1, and the detection is using the free-space filter setups of chapter 2.2.3 before detection on superconducting nanowire single photon detectors (SNSPD). The detection is in a Hanbury Brown and Twiss configuration to measure the auto-correlation of the anti-Stokes field in section 3.3.2.

scattering probabilities as [52]

$$p_{\mathrm{S}} = \exp\left[\frac{\kappa_{\mathrm{e}}}{\kappa}\frac{4g_0^2 E_{\mathrm{p}}}{\hbar\omega(\Omega^2+(\kappa/2)^2)}\right] - 1, \tag{3.2}$$

$$p_{\mathrm{aS}} = 1 - \exp\left[-\frac{\kappa_{\mathrm{e}}}{\kappa}\frac{4g_0^2 E_{\mathrm{p}}}{\hbar\omega(\Omega^2+(\kappa/2)^2)}\right]. \tag{3.3}$$

Experimentally, we can access the detector clickrates C_{S} of Stokes and C_{aS} of anti-Stokes photons. They are related to the scattering probabilities by introducing the total detection efficiencies η_i with $i = 1,2$ for the two detectors. We write

$$C_{\mathrm{S}} = (\eta_1+\eta_2)\times p_{\mathrm{S}}\times(1+n), \tag{3.4}$$

$$C_{\mathrm{aS}} = (\eta_1+\eta_2)\times p_{\mathrm{aS}}\times n \tag{3.5}$$

where, additionally, we note a dependency on the number of excitations of the mechanical mode $n = \langle\hat{n}_{\mathrm{m}}\rangle = \langle\hat{a}^\dagger\hat{a}\rangle$, where we define the mechanical operators as in chapter 1.2. This ultimately stems from the effect of creation and annihilation operators of Fock states as $\hat{a}^\dagger|n\rangle = \sqrt{n+1}|n+1\rangle$ and $\hat{a}|n\rangle = \sqrt{n}|n-1\rangle$ during the optomechanical interactions. This will be used in section 3.2.3 as it is the basis for the so called asymmetry measurement [47, 53]. Knowing η_i in Eq. 3.5, we can therefore calculate the optomechanical scattering probabilities p_{S} and p_{aS} from the experimentally measured scattering rates.

We can calibrate the efficiencies η_i for the two detection lines by performing a series of independent measurements. First, the fiber-to-device coupling efficiency η_{fc} is measured by sending light with a detuning from the resonance and a known power to the device and then measuring the reflected power as in section 3.1. The extraction efficiency of cavity photons η_{dev} is obtained from the device impedance ratio $\eta_{\mathrm{dev}} = \kappa_{\mathrm{e}}/\kappa$ of the optical cavity. Furthermore, we measure the efficiency of detecting photons coming from the device for each SNSPD. We launch weak, off-resonant optical pulses with an average of around one photon to the device and measure the photon count rate of each SNSPD. This measurement gives the quantities $\eta_{\mathrm{fc}}^2 \times \eta_{\mathrm{trans},i} \times \eta_{\mathrm{QE},i}$, where $\eta_{\mathrm{trans},i}$ is the

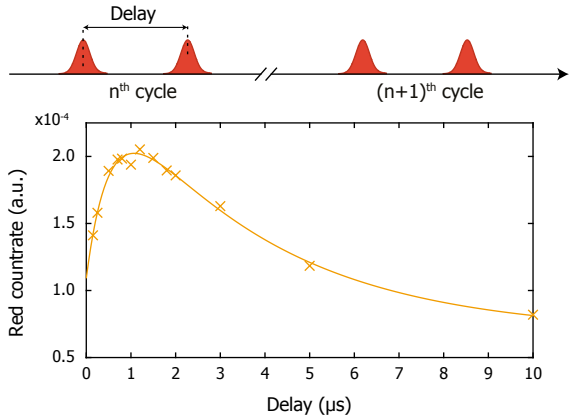

Figure 3.3: Thermalization curve of a medium-Q device with damping time of 3.6 μs, acquired with a pump-probe scheme. Two red pulses with equal strength are employed, such that the first one causes a temperature rise of the mode which increases the scattering rate of the second pulse depending on the delay. The plot data is generated with the device from chapter 5.

transmission efficiency of the detection path to each SNSPD, while $\eta_{\mathrm{QE},i}$ is their quantum efficiency. As η_{fc} is measured independently, $\eta_{\mathrm{trans},i} \times \eta_{\mathrm{QE},i}$ can be calculated from these results. Finally, this allows us to obtain $\eta_i = \eta_{\mathrm{dev}} \times \eta_{\mathrm{fc}} \times \eta_{\mathrm{trans},i} \times \eta_{\mathrm{QE},i}$. The values of the total detection efficiency $\eta_1 + \eta_2$ vary between the different experiments between 0.9% in Ref. [52] up to 13% in chapter 6.

3.2.2. THERMALIZATION DYNAMICS

Driving of the nanobeams is accompanied by optical absorption in the silicon host material, as is the case for all solid state optical devices. Silicon is in principle a relatively low-absorbing material, owing to the 1 eV indirect bandgap of the material. In integrated waveguides, however, the surface properties play a decisive role for the absorption because of a high exposure of the optical mode to the surface. Defects due to microfabrication imperfections cause a variety of electronic intra-bandgap states which, once they are excited, decay non-radiatively in phonon assisted processes [8]. It is found that the subsequent phonon relaxation process cause an increase in the occupancy of the 5 GHz mode which we can measure using a pump-probe experiment.

Variations to the experimental procedure exist but in the simplest case we pump and probe the device using a single laser tone with red-sideband detuning in the setup of Figure 3.2. We use Eq. 3.5 for the optomechanical scattering probability under the assumption that the anti-Stokes scattering is proportional to the number of excitations of the mode, i.e. $C_{\mathrm{aS}} \propto n = \langle \hat{n}_{\mathrm{m}} \rangle$. Prior to the arrival of the first pulse, we let the device thermalize to the bath environment such that the optomechanical interaction due to a red-pulse is largely suppressed. All dynamics in the mode occupation are thus due to the heating. An example data set is shown in Figure 3.3. We see an increase in the temperature on the timescale of around a microsecond and a later ringdown of the mode when the device re-thermalizes to the bath. This decay fits well to an exponential decay

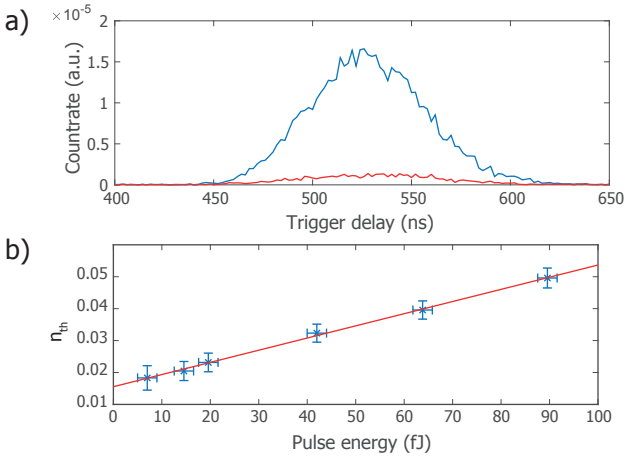

Figure 3.4: a) A sideband asymmetry measurement to extract the thermal phonon mode occupation n_{th}. We plot the rate of detected photons for blue-detuned (blue) and red-detuned (red) driving versus an arbitrary trigger delay for a pulse energy of ~15 fJ. Two pulses with a clear asymmetry in clickrates can be seen, from which the thermal occupation can be calculated as described in the main text. Unwanted contributions from leaked pump photons and detector dark counts can in principle independently be measured and subtracted, though is not done here. b) Power dependence for the inferred thermal occupation n_{th} of the device. The plot data is generated with the device from chapter 5.

function such that the method is additionally well suited to determine the mechanical Quality factor. The full dynamics at times t are found to be captured well by a double exponential function of the form

$$C(t) = C_0 + a\mathrm{e}^{-t/\tau_{\mathrm{abs}}} - b\mathrm{e}^{-t/\tau_{\mathrm{dec}}}, \tag{3.6}$$

where we fit the decay times τ_{dec} as well as absorption rise times τ_{abs}. The value for τ_{abs} is typically found to be between 600 to 800 ns with only minimal changes from device to device or even after adding a phononic shield (see chapter 6). The offset C_0 is due to the absorption background within the pulses. The parameters a and b are free fit parameters related to the amount of heating. They are typically not evaluated, as this measurement is typically taken at relatively high optical powers, causing excessive absorption heating in the device.

3.2.3. SIDEBAND ASYMMETRY

The quantum protocols employed in the following require that the mechanical mode is initialized to its quantum groundstate $|\Psi\rangle_{\mathrm{m}} = |0\rangle_{\mathrm{m}}$. This in principle a valid approximation for the mode with frequency of 5 Ghz at temperature $T \approx 10$ mK. Using the Boltzmann constant k_{B} and reduced Planck constant $\hbar$, we expect a mean phonon number of[1]

[1] We can write a density matrix for a thermal mechanical state as $\rho_{\mathrm{m}} = \frac{1}{Z}\sum_j \exp(-jk_{\mathrm{B}}T/\hbar\omega)|j\rangle\langle j|_{\mathrm{m}}$ with partition sum $Z = \sum_j \exp(-k_{\mathrm{B}}T/\hbar\omega)$ [54] and calculate the expected number of phonons as $n_{\mathrm{th}} = \langle\hat{n}_{\mathrm{m}}\rangle = \mathrm{Tr}(\rho_{\mathrm{m}}\hat{n})$.

$$n_{\mathrm{th}} = \frac{e^{-k_{\mathrm{B}}T/\hbar\Omega}}{1-e^{-k_{\mathrm{B}}T/\hbar\Omega}} \approx 10^{-9}. \tag{3.7}$$

We can experimentally measure this occupation using what is called the sideband asymmetry [6, 53]. We employ a pulsed scheme in which we send either red-detuned or blue detuned pulses with identical pulse energies to the devices. Each trial consists of a single pulse and the repetition rate is chosen to be much longer than the device energy decay, such that the device is well thermalized to the environment prior to each interaction. As seen in Eq. 3.5, the optomechanical scattering attains different rates in the vicinity of the groundstate. Assuming identical pulse energies and small interaction strengths, the anti-Stokes scattering goes as $\propto n_{\mathrm{therm}}$ whereas Stokes scattering has a $\propto n+1$ dependence. Intuitively this can be explained by noting that it is always possible to Stokes scatter hence amplify the mechanical motion. Close to the groundstate, however, the anti-Stokes scattering is suppressed since further cooling of the mode is not possible.

Figure 3.4a shows an example of the clickrates that we get from blue and red detuned driving of a device at 10 mK bath temperature. A pronounced asymmetry can be seen from which the thermal occupation can be calibrated using Eq. 3.5 as $n_{\mathrm{th}} = C_{\mathrm{aS}}/(C_{\mathrm{S}} - C_{\mathrm{aS}})$. This holds for $p_{\mathrm{S}}, p_{\mathrm{aS}} << 1$, such that Stokes and anti-Stokes scattering rates are roughly equal $p_{\mathrm{S}} \approx p_{\mathrm{aS}}$ (see Eqs. 3.2 and 3.3). A power sweep (Figure 3.4b) in the limit of small scattering rates reveals an additional dependency of the measured occupation on the amount of optical power that is used. The reason is a remaining amount of optical absorption which thermally populates the modes during the pulses. While the measured occupation is well below one and the device is thus firmly initialized in the groundstate, we still do not measure the actual base temperature. An extrapolation to zero from a power sweep as in Figure 3.4b can yield a better approximation to the bath temperature. The axis offset is, however, still dominated by leaked drive photons through the filters.

3.3. QUANTUM CORRELATIONS

After the device performance is sufficiently characterized, we can now turn to study its quantum behavior. For complete theoretical descriptions of the dynamics in the optomechanical system under pulsed driving, the reader is referred to Refs. [55, 56]. Here, we focus on experimental aspects and introduce two measurements of the non-classicality of the optomechancial states generated from blue sideband driving together with single photon counting.

3.3.1. CROSS-CORRELATION

The cross-correlation is a measurement of the non-classicality of the correlations between Stokes and anti-Stokes fields. In second quantization, we can define it as

$$g^{(2)}_{\mathrm{ab}} = \frac{\langle \hat{a}^\dagger \hat{a} \hat{b}^\dagger \hat{b} \rangle}{\langle \hat{a}^\dagger \hat{a} \rangle \langle \hat{b}^\dagger \hat{b} \rangle}. \tag{3.8}$$

We define the cross-correlation for two arbitrary fields a and b with respective annihilation operators $\hat{a}$ and $\hat{b}$.

The mode a refers to the Stokes field and mode b is used for the anti-Stokes field, which in the following theoretical description is interchangeable with the mechanical mode itself. It can be shown that the cross correlation is limited for any two classical fields by a Cauchy Schwartz inequality according to

$$R = \frac{\left(g^{(2)}_{\mathrm{ab}}\right)^2}{g^{(2)}_{\mathrm{aa}}\, g^{(2)}_{\mathrm{bb}}} \leq 1 \tag{3.9}$$

where the auto-correlation functions $g^{(2)}_{\mathrm{aa}}$ and $g^{(2)}_{\mathrm{bb}}$ are defined by substitution in equation 3.8. It can be shown that $R < 1$ if the P-representation of the states of the modes attain negative values [57, 58]. For all classical fields, i.e. mixtures of coherent states, the P-representation always stays positive and thus Eq. 3.9 is not violated. To illustrate this, two thermal states result in R=0.25 and two coherent states in R=1, both satisfying the inequality. Quantum states with expressed particle nature, such as bi-photon Fock states $|11\rangle_{\mathrm{a,b}}$, however, lead to a maximal violation with $R \to \infty$.

The cross-correlation is exceptionally useful to quantify the amount of quantum correlations produced by the two-mode squeezing interaction, which we can see by an explicit calculation. We start with the ideal case where both the optical and mechanical mode are initially in a vaccuum state. The two-mode squeezing with Stokes scattering probability p_{S} results in a state of the form

$$|\psi\rangle_{\mathrm{ab}} = \frac{1}{\sqrt{\sum_k p_{\mathrm{S}}^k}} \sum_k \sqrt{p_{\mathrm{S}}}^k |kk\rangle, \tag{3.10}$$

where we use a and b as placeholders for the mechanical mode and Stokes field. We calculate the number of excitations in the Stoked field as

$$\begin{aligned}
\langle \hat{a}^\dagger \hat{a} \rangle &= \frac{1}{\sum_k p_{\mathrm{S}}^k} \sum_k p_{\mathrm{S}}^k \langle kk|\hat{a}^\dagger \hat{a}|kk\rangle && (3.11)\\
&= \frac{1}{\sum_k p_{\mathrm{S}}^k} \sum_k k p_{\mathrm{S}}^k && (3.12)\\
&= \frac{1}{1/(1-p_{\mathrm{S}})} \frac{p_{\mathrm{S}}}{(1-p_{\mathrm{S}})^2} && (3.13)\\
&= \frac{p_{\mathrm{S}}}{1-p_{\mathrm{S}}}. && (3.14)
\end{aligned}$$

Similarly, we get the number of mechanical excitations $\langle \hat{b}^\dagger \hat{b} \rangle = p_{\mathrm{S}}/(1-p_{\mathrm{S}})$, which we treat as equal to the number of anti-Stokes photons for simplicity. We also calculate the

cross-term

$$\langle \hat{a}^\dagger \hat{b}^\dagger \hat{b} \hat{a} \rangle = \frac{1}{\sum_k p_S^k} \sum_k p_S^k \langle kk | \hat{a}^\dagger \hat{b}^\dagger \hat{b} \hat{a} | kk \rangle \tag{3.15}$$

$$= \frac{1}{\sum_k p_S^k} \sum_k k^2 p_S^k \tag{3.16}$$

$$= \frac{1}{1/(1-p_S)} \frac{p_S(1+p_S)}{(1-p_S)^3} \tag{3.17}$$

$$= \frac{p_S(1+p_S)}{(1-p_S)^2}. \tag{3.18}$$

Combining those, we get the cross correlation as

$$g_{ab}^{(2)} = \frac{\langle \hat{a}^\dagger \hat{b}^\dagger \hat{b} \hat{a} \rangle}{\langle \hat{a}^\dagger \hat{a} \rangle \langle \hat{b}^\dagger \hat{b} \rangle} = 1 + \frac{1}{p_S}. \tag{3.19}$$

We can see that the non-classicality of the optomechanical state is approximately inversely proportional to the Stokes scattering probability. As we have seen before, higher order excitation terms reduce the amount of non-classical correlations in the state, such that it looses its particle nature. A similar reduction of the cross-correlation is expected due to a non-negligible thermal occupation n_{th} of the mechanical mode. Assuming that this background affects the cross correlation similarly to higher order excitation terms in the two-mode squeezing, we write this as [52]

$$g_{ab}^{(2)} \approx 1 + \frac{1}{p_S + n_{th}}. \tag{3.20}$$

We can use numerical methods [59, 60] to verify this approximation. To do so, we define an initial state as product state of an optical mode a in the vacuum and a mechanical mode b in a thermal state of initial occupation n_{th}:

$$\rho_{ab,init} = \frac{1}{2} |0\rangle \langle 0|_a \otimes \frac{1-S}{2} \sum_k S^k |k\rangle \langle k|_b \tag{3.21}$$

with $S = n_{th}/(1+n_{th})$. We use the two-mode squeezing Hamiltonian $\hat{H}_{TMS} = -i\hbar(\hat{a}^\dagger \hat{b}^\dagger + \hat{a}\hat{b})$ and propagate it with $\hat{U} = \exp\left(-i/\hbar \hat{H}_{TMS} t\right)$. Using the Stokes scattering probability p_S, we calculate explicitly

$$\rho_{ab} = e^{i\sqrt{p_S}(\hat{a}^\dagger \hat{b}^\dagger + \hat{a}\hat{b})} \rho_{ab,init} e^{-i\sqrt{p_S}(\hat{a}^\dagger \hat{b}^\dagger + \hat{a}\hat{b})}. \tag{3.22}$$

Finally, we calculate the expectation values as $\langle \hat{A} \rangle = \mathrm{Tr}\left(\hat{A} \rho_{ab}(t_f)\right)$ to get the cross-correlation of Eq. 3.8, once again setting the mechanical mode equal to the anti-Stokes field for simplicity. We plot the numerical values in Figure 3.5 alongside the analytical approximation. We find reasonable agreement for small temperatures below 0.2 phonons, validating the approximate Eq. 3.20. We can thus use this analytical formula in practice to predict an expected cross correlation of a device from the temperature measurements of section 3.2.3. This allows for greatly reduced measurement times while predicting

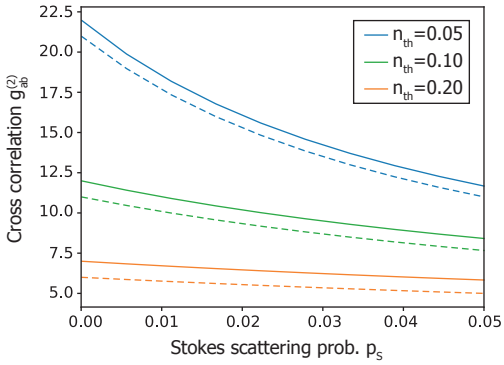

Figure 3.5: Simulated of the cross-correlation $g^{(2)}_{ab}$ (full lines) compared to the analytical approximation of Eq. 3.20 (dashed lines). We show the solutions for three different values of thermal occupation n_{th}=0.05, 0.10 and 0.20 and for Stokes scattering probabilities up to 5% which covers the experimentally relevant parameter regime. The relative error reduces to a few percent for strongly non-classical values of $g^{(2)}_{ab} >> 2$. As such, Eq. 3.20 is sufficient to predict the expected cross-correlation for a device from the asymmetry measurement of section 3.2.3.

.

the performance of a given device, as the asymmetry is calculated from the bare click-rates while the cross correlation requires coincidences of Stokes and anti-Stokes photons. This is most relevant in the entanglement experiments of chapters 4 and 5, where we use the cross-correlation in turn to predict the interferometric visibilities with pairs of resonators.

Experimentally, we evaluate this cross-correlation onto the Stokes (S) and anti-Stokes (aS) fields from the device. This can be conveniently translated into the single photon counting experiments as the probability per trial to get a click in either of the two individually, $P(\mathrm{S})$ and $P(\mathrm{aS})$, or within the same trial $P(\mathrm{S} \wedge \mathrm{aS})$. We thus measure

$$g^{(2)}_{\mathrm{S,aS}} = \frac{P(\mathrm{S} \wedge \mathrm{aS})}{P(\mathrm{S})P(\mathrm{aS})}. \tag{3.23}$$

As shown above, a value of $R > 1$ in the Cauchy-Schwartz inequality 3.9 confirms non-classical correlations between the Stokes and the anti-Stokes field as produced by the two-mode squeezed state. A rigorous measurement would require to evaluate the auto-correlation functions of Stoked fields $g^{(2)}_{\mathrm{S,S}}$ and anti-Stokes fields $g^{(2)}_{\mathrm{aS,aS}}$. For practical purposes, we often assume the auto-correlation functions for Stokes and anti-Stokes fields are $g^{(2)}_{\mathrm{ii}} = 2$ such that the measurement can be done even using only one single photon detector. This assumption has been experimentally verified in Refs. [52, 57] and is also discussed in detail in [58].

3.3.2. AUTO-CORRELATION

While the cross-correlation measurements allow to detect non-classical correlations between Stokes and anti-Stokes photons, we can also directly confirm of the quantum nature of the mechanical state in a Hanbury Brown and Twiss experiment. While we still

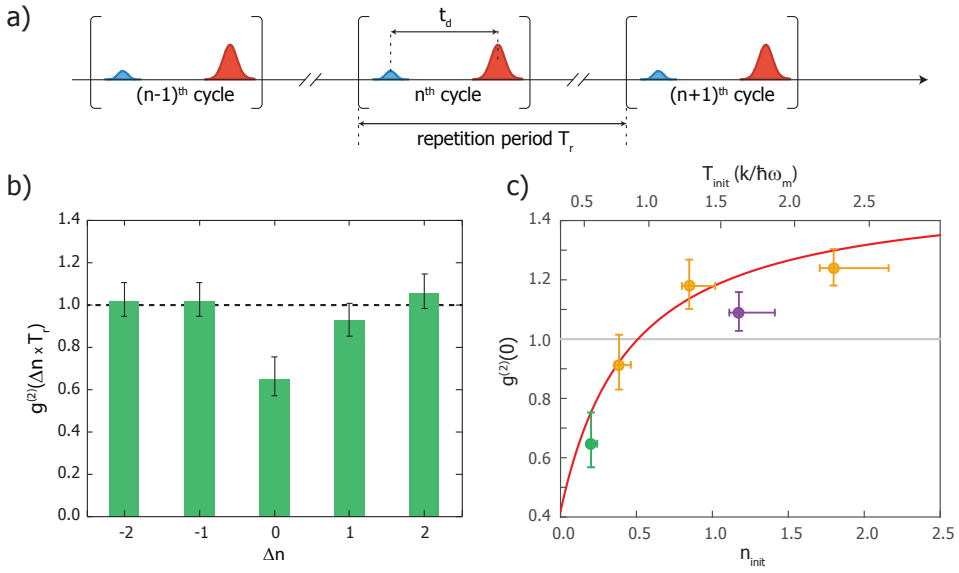

Figure 3.6: a) Pulse sequence used in the experiments, consisting of a blue-detuned pump pulse and a subsequent red-detuned read pulse delayed by t_d. b) The measurement of the second-order correlation function $g^{(2)}(\tau = \Delta n \times T_\mathrm{r})$ of the heralded phonons, with $g^{(2)}(0) < 1$ being a direct measure of their non-classicality. In this measurement, we set $t_d = 115$ ns and $T_\mathrm{r} = 50\ \mu$s. $g^{(2)}(\Delta n \times T_\mathrm{r})$ with $\Delta n \neq 0$ depicts the correlations between phonons read from separate pulse sequences with the cycle difference of Δn. While phonons from independent pulses show no correlation $g^{(2)}(\Delta n \times T_\mathrm{r}; \Delta n \neq 0) \approx 1$, those from the same read pulse are strongly anti-correlated with a $g^{(2)}(\tau = 0) = 0.65^{+0.11}_{-0.08}$. c) The influence of an incoherent phonon background on the $g^{(2)}(0)$ of the generated mechanical states. We plot several measurements for a range of different effective initial temperatures of the nanomechanical oscillator. The first data point (green) is taken with a delay $t_\mathrm{d} = 115$ ns and a repetition period $T_\mathrm{r} = 50\ \mu$s. We control the initial mode occupation n_init utilizing the long lifetime of the thermally excited phonons stemming from the delayed absorption heating by pump and read pulses. This allows to increase n_init while keeping the bulk temperature and properties of the device constant, causing an increase of $g^{(2)}(0)$, as the state becomes more thermal. The red line shows the simulated $g^{(2)}(0)$ as discussed in [52]. For technical reasons all data points (yellow, purple) except the leftmost (green) were taken with $t_\mathrm{d} = 95$ ns. In addition, the second from the right (purple) was taken at an elevated bath temperature of $T_\mathrm{bath} = 160$ mK. Figure adapted from Ref. [52]

do require a detection of a Stokes photon to herald the successful preparation of the mechanical mode, the actual measurement in this case is only performed on the anti-Stokes photons. Experimentally, the light is detected on a pair of detectors, $D1$ and $D2$ after being split by a beamsplitter as in Figure 3.2. Due to amplitude fluctuations, all classical fields will produce coincidence clicks on both detectors even for vanishing intensities. If the mechanical mode and hence the anti-Stokes field is close to the first excited Fock state, however, then the chance of clicks on both detectors is greatly reduced. We can assess this by evaluating the auto-correlation $g^{(2)}_\mathrm{aS,aS}$, which can be expressed as

$$g^{(2)}_\mathrm{aS,aS} = \frac{P(\mathrm{D1} \wedge \mathrm{D2})}{P(\mathrm{D1})P(\mathrm{D2})}. \tag{3.24}$$

In here, we write the probability to detect on D1 or D2 as $P(\mathrm{D1})$ and $P(\mathrm{D2})$ and the probability of a coincidence as $P(\mathrm{D1} \wedge \mathrm{D2})$. We note that for classical fields, the auto-correlation is bound to $g^{(2)}_{\mathrm{aS,aS}} \geq 1$, whereas for single phonon Fock states in the mechanical mode $g^{(2)}_{\mathrm{aS,aS}} = 0$.

In Ref. [52] we perform such an auto-correlation measurement using a blue pulse energy of 27 fJ, such that $p_{\mathrm{S}} = 1.2\%$. The mean read pulse energy is set to 924 fJ, corresponding to a state-swap efficiency $p_{\mathrm{aS}} \approx 32.5\%$ for the device in use. Taking into account subsequent optical scattering losses, this yields an absolute quantum efficiency for the detection of phonons of 0.9%. The pulse repetition period of $T_{\mathrm{r}} = 50\ \mu$s is long compared to the mechanical damping time of 11 μs, providing ample time for dissipating any excitation or unwanted heating generated by optical absorption. This ensures that each experimental cycle starts with the mechanical mode well in the quantum ground state. The pulse sequence is repeated more than 7×10^9 times in order to acquire enough statistics. In our first experiment, we set a delay between the blue and the red pulse of $t_d = 115$ ns and measure a $g^{(2)}(0)$ of $0.65^{+0.11}_{-0.08}$ (Figure 3.6b), clearly demonstrating the non-classical character of the mechanical state.

The observed $g^{(2)}(0)$ is considerably higher than what we expect in the ideal case $g^{(2)}_{\mathrm{ideal}}(0) \approx 4 \times p_{\mathrm{S}} = 0.045$ [56]. We attribute this to heating induced by the absorption of the optical drives. Including an estimation of the initial thermal phonon number n_{init}, which is inferred from the unconditional photon counts associated with the pump and read pulses, we construct a theoretical model (see [52]) that predicts $g^{(2)}(0)$ as a function of p_{S}, the initial thermal ocuupation n_{init}, and the absorption induced occupation $\dot{n}_{\mathrm{abs}}$. Given the measured $n_{\mathrm{init}} \approx 0.20$ and an n_{abs} which is discussed in the supplementary material of Ref. [52], our model predicts $g^{(2)}(0) \approx 0.76$, which is consistent with the experimental value. To further probe the effect of thermal phonons, we perform a set of experiments with reduced repetition periods T_r, while keeping the other settings for the pump pulses the same. This effectively increases n_{init}, because the absorbed heat does not have enough time to dissipate before the next pair of pulses arrives. As expected, as T_r is reduced, we observe an increase in $g^{(2)}(0)$. With the measured n_{init} and $\dot{n}_{\mathrm{abs}}$ from the same data set, we can plot the predicted $g^{(2)}(0)$ values. As is shown in Figure 3.6 c), the experimental values and theoretical bounds on $g^{(2)}(0)$ are in good agreement.

4

REMOTE QUANTUM ENTANGLEMENT BETWEEN MICROMECHANICAL OSCILLATORS

Ralf RIEDINGER, Andreas WALLUCKS, Igor MARINKOVIĆ, Clemens LÖSCHNAUER, Markus ASPELMEYER, Sungkun HONG, Simon GRÖBLACHER

Entanglement is a crucial resource for quantum communication networks [3]. Of particular relevance is the ability to distribute entanglement between remote systems that can also serve as quantum memories. Previous realizations have utilized atomic systems including warm [61, 62] and cold vapors [63, 64], individual atoms [65] and ions [66, 67] and defects in solid state systems [68–70], amongst others. Here we introduce a purely micromachined solid-state platform in the form of chip-based nano-optomechanical resonators. We create and demonstrate entanglement between two nanomechanical devices across two chips that are separated by 20 cm. By transferring the mechanical quantum state to a laser field at telecom wavelength we also demonstrate the feasibility of directly incorporating our system into a real quantum network.

This chapter has been published as *Remote quantum entanglement between two micromechanical oscillators.* R. Riedinger, A. Wallucks, I. Marinković, C. Löschnauer, M. Aspelmeyer, S. Hong, and S. Gröblacher. Nature **556**, 473 – 477 (2018)

4.1. INTRODUCTION

In recent years, nanofabricated mechanical oscillators have emerged as a promising platform for quantum information processing. The field of opto- and electromechanics has seen great progress, including ground state cooling [53, 71], quantum interfaces to optical or microwave modes [57, 72], mechanical squeezing [73] and single phonon manipulation [16, 17, 52, 74]. The demonstration of distributed mechanical entanglement however, was so far limited to intrinsic material resonances [75] and the motion of trapped ions [67]. Entanglement of engineered (opto-)mechanical resonances on the other hand would offer a new compelling route towards scalable quantum networks. The freedom of designing and choosing the optical resonances would allow for operation in the entire frequency range of the technologically important C-, S- and L-band of fiber optic telecommunication. Together with dense wavelength division multiplexing (on the ITU-T grid), this could enable quantum nodes separated by long distances (~100 km) to communicate with large bandwidths. State of the art energy lifetimes for these engineered mechanical elements typically range between micro- [57] and milli-seconds [76], which would allow for entanglement distribution on a regional level [77]. In addition, these entangled mechanical systems could be interfaced with microwaves [23], opening up the possibility to integrate superconducting quantum processors in the local nodes of the network.

In this letter, we report on the observation of distributed entanglement of two nanomechanical resonators, mediated by telecom photons. We employ a protocol first proposed by Duan, Lukin, Cirac and Zoller (DLCZ) [10], which was experimentally pioneered with ensembles of cold atoms [63]. The entanglement is generated probabilistically by heralding a single phonon through the detection of a signal photon that could originate from either of the two identical optomechanical oscillators. Fabrication imperfections have previously limited the use of artificial structures, requiring external tuning mechanisms to render the systems indistinguishable. Here we demonstrate not only that obtaining sufficiently identical devices is in fact possible through nanofabrication but that our method should also allow scaling to more than two systems.

4.2. METHODS

The mechanical oscillators we use in our experiment are nano-structured silicon beams with co-localized mechanical and optical resonances. Radiation pressure forces and the photoelastic effect couple the optical and mechanical mode with a rate g_0, causing the optical frequency to shift under the displacement of the mechanical oscillator [7]. This effect can be utilized to selectively address Stokes and anti-Stokes transitions by driving the optical resonance with detuned laser beams, resulting in a linear optomechanical interaction. As was recently shown, this technique can be used to create non-classical mechanical and optomechanical states at the single quantum level for individual devices using photon counting and postselection [52, 57].

In order to apply the DLCZ scheme to the entanglement of two separate optomechanical crystals, a critical requirement is that the photons emitted from the optomechanical cavities have to be indistinguishable. This can be achieved by creating a pair of nanobeams with identical optical and mechanical resonances. To date, however, fab-

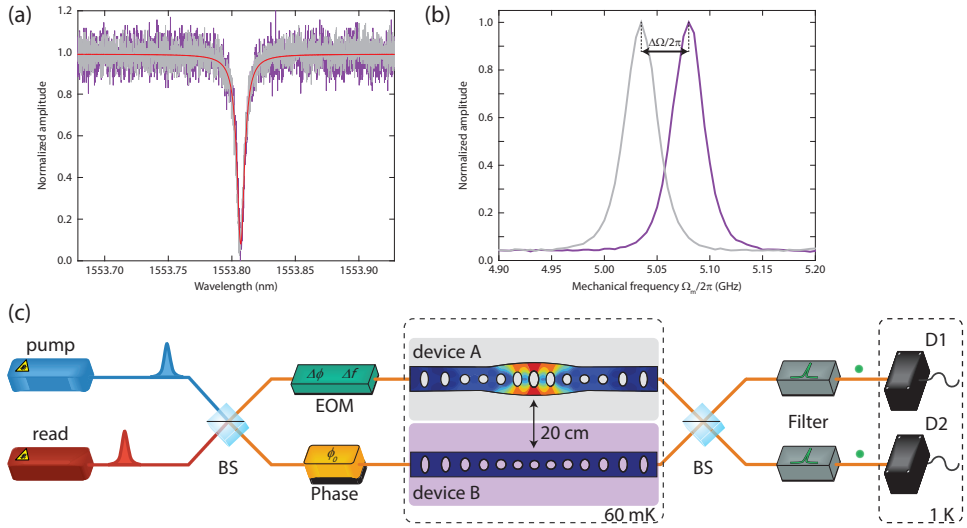

Figure 4.1: Devices and experimental setup.(a) Optical resonances. Plotted are the optical resonances of device A (gray) and device B (magenta). The Lorentzian fit result (red line) yields a quality factor for each cavity of around $Q = 2.2 \cdot 10^5$. (b) Mechanical resonances. The normalized mechanical resonances are measured through the optomechanical sideband scattering rates. The linewidth is limited by the bandwidth of the optical pulses and filters. Their frequencies differ by $\Delta\Omega_m/2\pi = 45$ MHz, which could result in distinguishable photons potentially reducing the entanglement in the system. We compensate for this shift by tuning the optical pump fields accordingly through serrodyning, erasing any information that could lead to a separable state. (c) Sketch of the experimental setup. We create optical pulses from two lasers, which are detuned to the Stokes (pump) and anti-Stokes (read) transition of the optomechanical cavities. They are then combined on a 50/50 beamsplitter (BS), which forms an interferometer with a second combining beamsplitter. Each arm contains one of the mechanical oscillators cooled to their groundstate in a dilution refrigerator. The phase of the interferometer ϕ_0 is stabilized using a fiber stretcher (Phase), while the phase between the pulses $\Delta\phi$ is controlled using an electro-optic modulator (EOM). The same EOM is also used for serrodyning. Optical filters in front of two superconducting single-photon detectors (D1, D2) ensure that only photons scattered onto cavity resonance are detected, while the original laser pulses are completely surpressed. The mechanical devices are physically separated by 20 cm, while their optical separation is around 70 m.

rication variations have inhibited the deterministic generation of fully identical devices and the current design of our oscillators does not include any tuning capabilities. Considering the optical mode alone, typical fabrication runs result in a spread of the resonance frequency of about 2 nm around the respective center wavelength. Finding a pair of matching optical resonances on two chips close to a target frequency therefore currently relies on fabricating a large enough set, where the probability of obtaining an identical pair is sufficiently high. In fact, this is achievable with a few hundred devices per chip (see SI for details). In addition, a small mismatch in the mechanical frequencies, which is typically around 1%, can readily be compensated by appropriate manipulation of the optical pulse frequencies in the experiment.

For the experiments presented here, we choose a pair of devices with optical resonances at $\lambda = 1553.8$ nm ($Q = 2.2 \cdot 10^5$, $g_0/2\pi = 550$ and 790 kHz for device A and B, re-

spectively, see Figure 4.1). For these particular structures, the mechanical resonances are centered around $\Omega_m/2\pi \approx 5.1$ GHz and have a relative difference of $\Delta\Omega_m/2\pi = 45$ MHz. The two chips are mounted 20 cm apart in a dilution refrigerator. While we use a single cryostat, there is in principle no fundamental or technical reason for keeping the devices in a common cold environment. For our specific setup, if the telecom fibers linking the two devices were to be unwrapped, our setup would already allow for bridging a separation of ~70 m between the two chips without further modification.

The protocol [10] for the creation and verification of the remote mechanical entanglement consists of three steps (for a schematic see Figure 4.2). Firstly, the two mechanical resonators are cryogenically cooled, initializing them close to their quantum ground states [52, 57, 76] (see SI). As a second step, a weak "pump" pulse tuned to the upper mechanical sideband ($\omega_{\text{pump}} = 2\pi c/\lambda + \Omega_m$, c - speed of light), is sent into a phase stabilized interferometer (with a fixed phase difference ϕ_0, see Figure 4.1 and SI) with one device in each arm. This drives the Stokes process, i.e. the scattering of a pump photon into the cavity resonance while simultaneously creating a phonon [57]. The presence of a single phonon is heralded by the detection of a scattered Stokes photon in one of our superconducting nanowire single-photon detector (SNSPD). The two optical paths of the interferometer are overlapped on a beamsplitter and a variable optical attenuator in one of the arms is set such that a scattered photon from either device is equally likely to go to each of the detectors. The heralding detection event therefore contains no information on which device the scattering took place and thus, where the phonon was created. The energy of the pulse is tuned such that the scattering probability $p_{\text{pump}} \approx 0.7\%$ is low, making the likelihood of creating phonons in both devices at the same time negligible. The heralding measurement therefore projects the mechanical state into a superposition of having a single excitation in device A $|A\rangle = |1\rangle_A|0\rangle_B$ or device B $|B\rangle = |0\rangle_A|1\rangle_B$, while the other one remains in the ground state. The joint state of the two mechanical systems

$$|\Psi\rangle_{=} \frac{1}{\sqrt{2}}\left(|1\rangle_A|0\rangle_B \pm e^{i\theta_m(0)}|0\rangle_A|1\rangle_B\right) \tag{4.1}$$

is therefore entangled, where $\theta_m(0) = \phi_0$ is the phase with which the mechanical state is initialized at time $\tau = 0$. It is determined by the relative phase difference that the pump beam acquires in the two interferometer arms [63], which we can choose using our interferometer lock. However, since the two mechanical frequencies differ by $\Delta\Omega_m$, the phase of the entangled state will continue to evolve as $\theta_m(\tau) = \phi_0 + \Delta\Omega_m\tau$. The sign in Eq. (4.1) reflects which detector is used for heralding.

In the third step of our protocol, we experimentally verify the entanglement between the two mechanical oscillators. To achieve this, we map the mechanical state onto an optical field using a "read" pulse after a variable delay τ. This relatively strong pulse is tuned to the lower mechanical sideband of the optical resonance ($\omega_{\text{read}} = 2\pi c/\lambda - \Omega_m$). At this detuning the field drives the anti-Stokes transition, i.e. a pump photon is scattered onto the cavity resonance while annihilating a phonon [57]. Ideally, this state transfer will convert $|\Psi\rangle$ into

$$|\Phi\rangle_{=} \frac{1}{\sqrt{2}}\left(|1\rangle_{r_A}|0\rangle_{r_B} \pm e^{i(\theta_r+\theta_m(\tau))}|0\rangle_{r_A}|1\rangle_{r_B}\right), \tag{4.2}$$

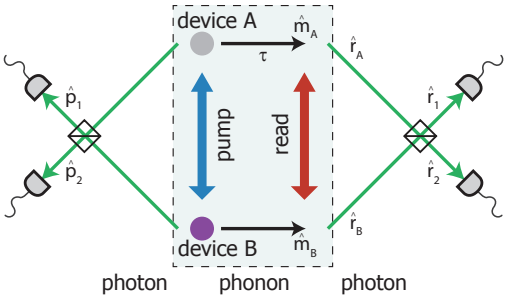

Figure 4.2: Schematics for creating and detecting entanglement between two remote mechanical oscillators. A pump pulse detuned to the Stokes sideband of two identical optomechanical resonators is sent into an interferometer, creating a single excitation in either device A or B. This process emits a photon on resonance with one of the cavities, where the two possible paths are super-imposed on a beamsplitter when exiting the interferometer (left). Detection of this photon in one of the single-photon detectors projects the two mechanical systems into an entangled state, in which neither device can be described separately. In order to verify this non-separable state, an optical read pulse tuned to the anti-Stokes sideband is sent into the interferometer with a delay of τ, de-exciting the mechanical systems and emitting another on-resonance photon into modes $\hat{r}_i$ (i = A,B). The two optical paths are again super-imposed on the same beamsplitter (right), and the photon is detected, allowing to measure various second-order correlation functions, which are used to test an entanglement witness. The operators $\hat{p}_j$, $\hat{r}_j$, and $\hat{m}_i$, with $j = 1,2$ and i = A,B, denote the optical modes created from the pump and the read pulses after recombination on a beamsplitter, as well as the mechanical modes, respectively. Note that in our experimental realization, the detectors for the pump and read photons are physically identical (see Fig. 4.1).

where r_A and r_B are the optical modes in the two interferometer arms. The state of the optical field will now contain the mechanical phase as well as the phase difference θ_r acquired by the read pulse. We can add an additional phase offset $\Delta\phi$ to the read pulse in one of the interferometer arms such that $\theta_r = \phi_0 + \Delta\phi$. Experimentally, this can be done by an electro-optic phase modulator (EOM) as shown in Figure 4.1. Sweeping $\Delta\phi$ allows us to probe the relative phase $\theta_m(\tau)$ between the superpositions $|A\rangle$ and $|B\rangle$ of the mechanical state for fixed delays τ. To avoid significant absorption heating, we limit the energy of the read pulse to a state swap fidelity of ~3.4%, reducing the added incoherent phonons to ~0.07 at a delay of τ = 123 ns (see SI).

So far we have neglected the consequence of slightly differing mechanical resonance frequencies for our heralding scheme. To compensate for the resulting frequency offset in the scattered (anti-) Stokes photons and to erase any available “which device" information, we shift the frequency of the laser pulses by means of serrodyning (see SI). Specifically, we use the EOM, which controls the phase offset $\Delta\phi$, to also shift the frequency of the pump (read) pulses to device A by $+\Delta\Omega_m$ ($-\Delta\Omega_m$). The frequency differences of the pulses in the two opposing paths exactly cancel out the difference in mechanical frequencies, ensuring indistinguishably of the scattered photons at the output of the interferometer.

In order to unambiguously demonstrate that the measured state is indeed entangled, we need to distinguish it from all possible separable states, i.e. the set of all states for which system A and B can be described independently. A specifically tailored mea-

sure that can be used to verify this non-separability of the state is called an "entanglement witness". Here we use a witness that is designed for optomechanical systems [78]. In contrast to other path-entanglement witnesses, such as the concurrence, it replaces measurements of third-order coherences $g^{(3)}$ by expressing them as second-order coherences $g^{(2)}$, under the assumption of linear interactions between Gaussian states (except the detection itself). This greatly simplifies the requirements and measurement times for the experiments we present here. The assumptions are satisfied for our system as our devices' initial mechanical states are in fact thermal states close to their quantum ground states (step 1 of our protocol, see SI) and we use the linearized optomechanical interactions, described in step 2 and 3 [79]. The upper bound for this witness of mechanical entanglement is given by [78] (see SI)

$$R_{\mathrm{m}}(\theta, j) = 4 \cdot \frac{g^{(2)}_{r1,pj}(\theta) + g^{(2)}_{r2,pj}(\theta) - 1}{(g^{(2)}_{r1,pj}(\theta) - g^{(2)}_{r2,pj}(\theta))^2}, \tag{4.3}$$

in a symmetric setup, with $\theta = \theta_{\mathrm{r}} + \theta_{\mathrm{m}}$, $j = 1,2$ denoting the heralding detectors and $g^{(2)}_{ri,pj} = \langle \hat{r}^\dagger_{\mathrm{i}} \hat{p}^\dagger_{\mathrm{j}} \hat{r}_{\mathrm{i}} \hat{p}_{\mathrm{j}} \rangle / \langle \hat{r}^\dagger_{\mathrm{i}} \hat{r}_{\mathrm{i}} \rangle \langle \hat{p}^\dagger_{\mathrm{j}} \hat{p}_{\mathrm{j}} \rangle$ the second order coherence between the photons scattered by the pump pulse ($\hat{p}^\dagger_{\mathrm{j}}$ creation operator of the mode going to detector $j = 1,2$) and the converted phonons from the read pulse ($\hat{r}^\dagger_{\mathrm{j}}$ creation operator of the mode going to detector $j = 1,2$). For all separable states of the mechanical oscillators A and B the witness yields $R_{\mathrm{m}}(\theta, j) \geq 1$ for any θ and j. Hence, if there exists a θ and j, for which $R_{\mathrm{m}}(\theta, j) < 1$, the mechanical systems must be entangled.

While entanglement witnesses are designed to be efficient classifiers, they typically depend on the individual characterstics of the experimental setup. If for example, the second beamsplitter (see Figure 4.1) were to malfunction and act as a perfect mirror, i.e. all photons from device A (B) were transmitted to detector 1 (2), $R_{\mathrm{m}}(\theta, j)$ could still be below 1 for separable states. This is due to the fact that the witness in Eq. (4.3) is estimating the visibility of the interference of $|A\rangle$ and $|B\rangle$ from a single measurement, without requiring a full phase scan of the interference fringe. To ensure the applicability of the witness, we therefore experimentally verify that we fulfill its assumptions. We first check that our setup is balanced by adjusting the pump laser power in each arm, as described above. This guarantees that the scattered photon flux impinging on the beamsplitter is equal from both arms (see SI). In order to symmetrize the detection, we use heralding detection events from both SNSPDs, i.e. we obtain the actual bound on the entanglement witness $R_{\mathrm{m,sym}}(\theta)$ from averaging measurements of $R_{\mathrm{m}}(\theta, 1)$ and $R_{\mathrm{m}}(\theta, 2)$ (see SI). By choosing the phase θ such that the correlations between different detectors $i \neq j$ exceed the correlations on the same detectors $j = 1,2$, $g^{(2)}_{ri,pj} > g^{(2)}_{rj,pj}$, we avoid that our measurements are susceptible to unequal splitting ratios of the beamsplitter.

4.3. RESULTS

In Figure 3 we perform a series of measurements of the second order coherence $g^{(2)}$, sweeping $\Delta\phi$ with a readout delay of $\tau = 123$ ns, verifying the coherence between $|A\rangle$ and $|B\rangle$. Using this data, we choose an optimal phase setting $\theta = \theta_{\mathrm{opt}}$ with $\Delta\phi = 0.2\pi$ for the main experiment. We obtain $R_{\mathrm{m,sym}}(\theta_{\mathrm{opt}}) = 0.74^{+0.12}_{-0.06}$ well below the separability

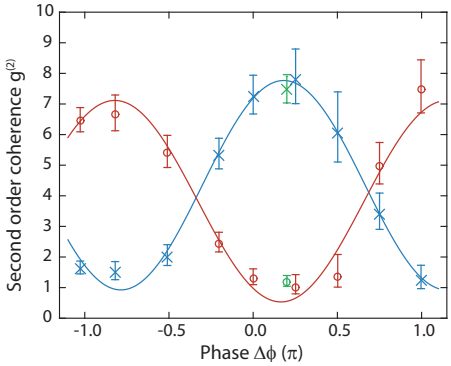

Figure 4.3: Phase sweep of the entangled state. We vary the phase between the pump and the read pulses, $\Delta\phi$, and measure the second order coherence of the Raman scattered photons for a fixed delay between the pulses $\tau = 123$ ns. Blue crosses represent the measurements of $g^{(2)}_{ri,pj}$ $(i \neq j = 1,2)$, while red circles are the results of $g^{(2)}_{ri,pi}$ $(i = 1,2)$. We fit simple sine functions (shown as solid lines) to each of the dataset as guides to the eyes. The sinusoidal dependence on the phase clearly highlights the coherence of the entangled mechanical state. We observe a periodicity of 1.95π, in good agreement with the expected 2π for single particle interference (see Eq. (4.2)) [78]. The phase sweep allows to identify the optimal phase $\Delta\phi = 0.2\pi$ for maximum visibility, at which we acquire additional data to obtain the entanglement witness with statistical significance. All error bars represent a 68% confidence interval.

bound of 1. Including the measurements at the non-optimal adjacent phases $\Delta\phi = 0$ and 0.25π, the statistical uncertainty improves, and we obtain $R_{\mathrm{m,sym}}([\theta_{\mathrm{opt}} - 0.2\pi, \theta_{\mathrm{opt}} + 0.05\pi]) = 0.74^{+0.08}_{-0.05}$. Hence, we experimentally observe entanglement between the two remote mechanical oscillators with a confidence level above 99.8%.

The coherence properties of the generated state can be characterized through the decay of the visibility $V = (\max(g^{(2)}_{ri,pj}) - \min(g^{(2)}_{ri,pj}))/\max(g^{(2)}_{ri,pj}) + \min(g^{(2)}_{ri,pj}))$. We therefore perform a sweep of the delay time τ between the pump pulse and the read pulse. The mechanical frequency difference $\Delta\Omega_m$ allows to sweep a full interference fringe by changing the delay τ by 22 ns. Due to a technically limited hold time of our cryostat this sweep had to be performed at a higher bath temperature of $T \approx 80 - 90$ mK, yielding a slightly lower, thermally limited, visibility at short delays, when compared to the data in Figure 4.3. We can vary the delay further and observe interference between $|A\rangle$ and $|B\rangle$, i.e. $V > 0$, up to $\tau \approx 3$ μs (see Fig. 4.4). The loss of coherence can be explained by absorption heating and the mechanical decay (see SI) and appears to be limited at long delays τ by the lifetime $1/\Gamma_{\mathrm{A}} \approx 4$ μs of device A, the shorter one of the two devices.

We have experimentally demonstrated entanglement of two engineered mechanical oscillators, separated spatially by 20 cm and optically by 70 m. Imperfections in the fabrication process and the resulting small deviations of optical and mechanical frequencies for nominally identical devices are overcome through statistical selection of devices and optical frequency shifting, using a serrodyne approach. The mechanical systems do not interact directly at any point but are remotely interfaced through optical photons in the telecom wavelength band. The coherence time of the entangled state of several microseconds appears to be limited by the mechanical lifetime and absorption heat-

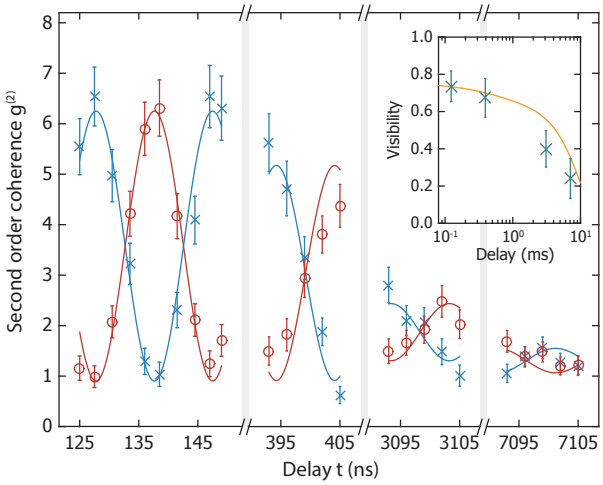

Figure 4.4: Time sweep of the entangled state. Shown is the interference of the entangled mechanical state at different delays τ between the pump and read pulses, with ϕ_0 and $\Delta\phi$ fixed. The blue crosses represent the measurements of $g^{(2)}_{ri,pj}$ $(i \neq j = 1,2)$, while red circles are the results of $g^{(2)}_{ri,pi}$ $(i = 1,2)$. The solid lines are sinusoidal fits, averaged over the two out-of-phase components for each delay window, serving as a guide to the eye. The coherence of the entangled state reduces over time, which can be seen by the decay of the interference visibility. This decoherence is consistent with a delayed optical absorption heating and the mechanical decay time of ~4 μs of device A. The inset shows the visibility of the interference (green crosses) and the expected upper bound to the visibility due to heating and the mechanical decay (orange line, see SI). All error bars represent a 68% confidence interval.

ing. Both can be significantly improved, e.g. by adding a phononic bandgap shield [76] and the use of intrinsic, desiccated silicon [80], respectively. While our devices are engineered for short mechanical lifetimes [52, 81], it can in principle be greatly increased. Early designs including such a phononic shield have reached $1/\Gamma \approx 0.5$ ms [76], and should still allow for further improvements. Combined with reduced optical absorption, allowing for efficient laser cooling, this can potentially put our devices on par with other state of the art quantum systems [82].

4.4. CONCLUSION

Our experiment demonstrates a protocol for realistic, telecom-compatible entanglement distribution using engineered mechanical quantum systems. When tolerating a drop in the interference visibility by 5%, current parameters would allow for a device separation of 75 km using commercially available telecommunication fibers (see discussion in SI for more details). The system presented here is directly scalable to more devices (see SI) and could be integrated into a real quantum network. Combining our results with optomechanical devices capable of transferring quantum information from the optical to the microwave domain, a highly active field of research [23, 83, 84], could provide a backbone for a future quantum internet using superconducting quantum computers.

Acknowledgments We would like to thank Vikas Anant, Klemens Hammerer, Se-

bastian Hofer, Richard Norte, Kevin Phelan and Joshua Slater for valuable discussions and help. We also acknowledge assistance from the Kavli Nanolab Delft, in particular from Marc Zuiddam and Charles de Boer. This project was supported by the European Commission under the Marie Curie Horizon 2020 initial training programme OMT (grant 722923), Foundation for Fundamental Research on Matter (FOM) Projectruimte grants (15PR3210, 16PR1054), the Vienna Science and Technology Fund WWTF (ICT12-049), the European Research Council (ERC CoG QLev4G, ERC StG Strong-Q), the Austrian Science Fund (FWF) under projects F40 (SFB FOQUS) and P28172, and by the Netherlands Organisation for Scientific Research (NWO/OCW), as part of the Frontiers of Nanoscience program, as well as through a Vidi grant (016.159.369). R.R. is supported by the FWF under project W1210 (CoQuS) and is a recipient of a DOC fellowship of the Austrian Academy of Sciences at the University of Vienna.

4.5. SUPPLEMENTARY INFORMATION

4.5.1. DEVICE FABRICATION AND CHARACTERIZATION

The devices in the main part are fabricated as described in reference [52]. The most crucial steps for generating two identical chips are the electron beam lithography and the inductively coupled plasma reactive ion etching. We beamwrite and etch on a single proto-chip containing two sets of devices. This chip is then diced into two halves, each with several hundred nominally identical resonators. The structures are subsequently released in 40% hydrofluoric acid and cleaned with the RCA method, followed by a dip in 2% hydrofluoric acid. When characterizing the two chips, we find the center wavelengths to be 1552.4 nm on chip A and 1550.0 nm on chip B (see Figure 4.5). The standard deviation on the spread of the optical resonances is around 2 nm on both chips. For the experiments in the main text, we search for resonances that overlap to within 10% of their linewidth, which is equal to around 100 MHz. We find a total of 5 pairs fulfilling this requirement within 234 devices tested per chip.

In order to verify that finding identical devices is not just lucky coincidence and that this can even be done with a smaller sample size per chip, one can estimate the number of devices needed for a birthday paradox type approach. Therefore, we assume a pair of chips with 234 devices each that are centered at the same target wavelength. Taking similar parameters as found in our actual chips, we use a spread in resonance wavelength of 2 nm and we define resonances to be identical if they match to within 100 MHz. While the probability of obtaining a single device exactly at the center wavelength is only 0.03%, the probability of finding two matching devices at any wavelength within this distribution is 99.9996%. This is reduced if an offset in the mean wavelength of the two chips is introduced. For an offset of 2.5 nm, the probability is 99.98%, and for 5 nm, it is still 92.7%. By extending this approach to, for example, four chips, with the same parameters as above, no offset in the center wavelength and 500 devices per chip, we calculate the probability of finding four identical resonances to be 51.6%. Such a quartet would directly enable experiments on entanglement swapping and tests of a Bell inequality, as proposed by DLCZ. Further improvements could include post-fabrication wavelength tuning, as has recently been demonstrated for similar devices [85]. This could signifi-

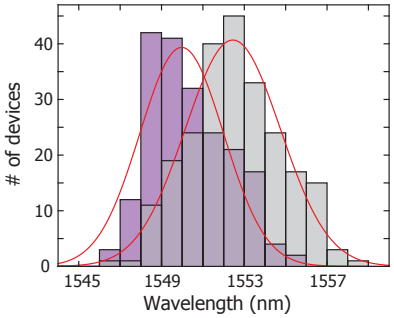

Figure 4.5: Distribution of optical wavelengths. We plot a histogram (bin size 1 nm) of the optical resonance wavelengths for a large set of devices on each of the chips containing devices A (gray) and B (magenta). The fits of a Gaussian distribution to the data sets (red solid lines) give a standard deviation of 2.3 nm and 2.0 nm, respectively. The large overlap of the optical resonance frequencies highlights the feasibility of extending the entanglement to even more optomechanical devices in the future.

cantly improve the prospect of scalability of our approach, as it would allow to fabricate identical devices more deterministically.

In addition, the mechanical resonances are also susceptible to fabrication errors and vary by up to 50 MHz for our devices. To overcome this mismatch, we use serrodyne frequency shifting (see sections below).

4.5.2. EXPERIMENTAL SETUP

A detailed drawing of the experimental setup is shown in Figure 4.6. The light sources for our pump and read beams are two New Focus 6728 CW lasers, tuned and stabilized on their respective sideband of the optical resonance. The beams are filtered by MicronOptics FFP-TF2 tunable optical filters in order to reduce the laser phase noise in the GHz regime. We then proceed to generate the actual pump and read pulses by driving acousto-optic modulators (Gooch&Housego T-M110-0.2C2J-3-F2S) with an arbitrary function generator (Tektronic AFG3152C). These pulses are then combined on a variable ratio coupler (Newport F-CPL-1550-N-FA). The combined optical mode is subsequently split by another variable ratio coupler and fed into the Mach Zehnder interferometer. The coupling ratio is adjusted to primarily compensate for a small difference in total losses between two paths. The power in the interferometer arms can additionally be balanced by an electrically driven variable optical attenuator (Sercalo VP1). We reflect the pulses from the two devices via optical circulators and recombine on a 50/50 coupler (measured deviation of 0.6%, see below). The strong pump pulses are filtered with two MicronOptics FFP-TF2 fiber filters per detection arm, tuned to transmit only the scattered (anti-) Stokes photons (bandwidth 50 MHz). We detect the resonant photons with superconducting nanowire single photon detectors (Photonspot) and register their arrival times on a TimeHarp 260 NANO correlation board.

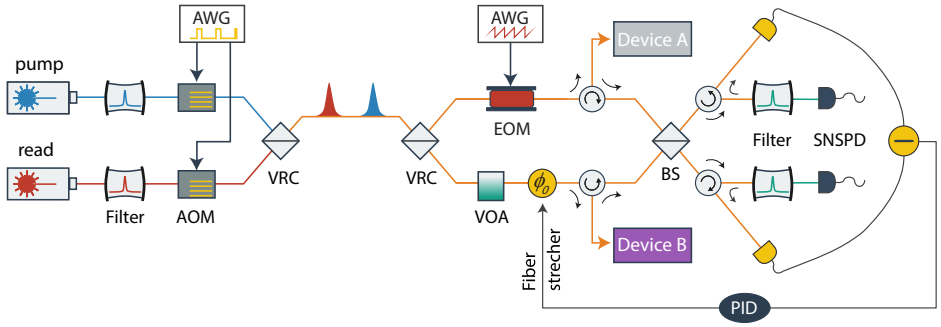

Figure 4.6: Experimental setup. A detailed schematics of our setup is shown here and described in the text. AOM are the acousto-optic modulators, AWG the arbitrary waveform generators, VRC the variable ratio couplers, EOM the electro-optic modulator, VOA the variable optical attenuator, BS the 50/50 beamsplitter and SNSPD the superconducting nanowire single-photon detectors.

4.5.3. SERRODYNE FREQUENCY SHIFTING

In our experiment, the mechanical frequency of device B ($\Omega_{m,B}$) is greater than of device A ($\Omega_{m,A}$) by $\Delta\Omega_m = 2\pi \cdot 45$ MHz. If we were to send pump pulses with exactly the same frequency ω_{pump} to both of the devices, they would produce scattered photons with frequencies $\omega_{o,A} = \omega_{pump} - \Omega_{m,A}$ and $\omega_{o,B} = \omega_{pump} - \Omega_{m,B} = \omega_{o,A} - \Delta\Omega_m$. This frequency mismatch of scattered photons from the two devices would make them distinguishable, therefore preventing the entangled state. A simple solution is to shift the frequency of the pump pulse going to the device A by $\Delta\Omega_m$, i.e. $\omega_{pump,A} = \omega_{pump} - \Delta\Omega_m$. We experimentally realize this by electrically driving the electro-optic phase modulator on the path to device A, with a sawtooth waveform. This so-called serrodyne modulation with frequency $\omega_s = \Delta\Omega_m$ and peak-to-peak phase amplitude of 2π results in an optical frequency shift of ω_s [86, 87]. We use an arbitrary waveform generator (Agilent 81180A, bandwidth DC to 600 MHz) to generate the sawtooth voltage signal, amplify it with a broadband amplifier (Minicircuits TVA-R5-13A+, bandwidth 0.5 to 1000 MHz) and apply it to the optical phase modulator (Photline MPZ-LN-10-P-P-FA-FA-P, bandwidth DC to 12 GHz). We also apply an additional DC-bias to the serrodyne signal in order to generate a fixed phase offset $\Delta\phi$ in the interferometer arms. Due to the high analog bandwidth of the AWG compared to the frequency shift of 45 MHz, higher order sidebands were negligible and were not observed in the experiment.

4.5.4. PHASE STABILIZATION OF THE INTERFEROMETER

For stabilizing the phase of the interferometer, we use an additional laser pulse ~5 μs after the read pulse. To produce these auxiliary pulses, we also use the red-detuned laser that generates the read pulses and send them along the same beam paths. After being reflected from the optical filters in the detection line, the pulses are re-routed by optical circulators and picked up by a balanced detector (see Figure 4.6). These signals are then sent to a PID controller, which regulates a fiber stretcher to stabilize the relative path length and therefore locking the phase of the interferometer on a slow timescale (i.e.

with the experiment repetition period of 50 μs).

In principle, the read or pump pulses that are reflected off the filter cavities could also be used for the phase locking. However, the serrodyne modulation during pump and read results in a beat signal of the pulses behind the beam splitter. This beating requires more sophisticated signal processing, which we avoid by using the auxiliary pulses, during which the serrodyne modulation is off. We note that the auxiliary pulses also induce some absorption heating of the devices. However, the 50 μs repetition period is sufficiently long compared to the decay times of the devices for the extra heating not to influence our experimental result.

4.5.5. ENTANGLEMENT WITNESS AND SYSTEMATIC ERRORS

The entanglement witness [88]

$$R(\tau, j) = \frac{\left\langle \hat{m}_{\mathrm{A}}^{\dagger}(\tau)\hat{m}_{\mathrm{A}}(\tau)\hat{m}_{\mathrm{B}}^{\dagger}(\tau)\hat{m}_{\mathrm{B}}(\tau)\right\rangle_j}{\left|\left\langle \hat{m}_{\mathrm{A}}^{\dagger}(\tau)\hat{m}_{\mathrm{B}}(\tau)\right\rangle_j\right|^2} \tag{4.4}$$

derived in reference [78] is based on the concurrence [89] of the bipartite mechanical system. Here, the conditional average $\langle\hat{o}\rangle_j = \langle\hat{o}\,\hat{p}_j^{\dagger}\hat{p}_j\rangle/\langle\hat{p}_j^{\dagger}\hat{p}_j\rangle$ for an operator $\hat{o}$ is its expectation value of the state heralded by a Stokes photon detected by detector j. The $\hat{m}_i$ ($\hat{m}_i^{\dagger}$) are the mechanical annihilation (creation) operators of device $i = \mathrm{A},\mathrm{B}$. While R is experimentally not directly accessible, the upper bound to this witness R_{m}, see Eq. (3), is a measurable quantity in our interferometry setup. The derivation of the inequality $R_{\mathrm{m}} \geq R$, as described in reference [78] and its supplementary material, is based on several of assumptions: The unheralded state must be Gaussian at all times, and the interference on the combining beamsplitter must be symmetric. In this section, we would like to discuss the validity of each of these assumptions in more detail.

To obtain R_{m}, threefold coincidence measurements are re-expressed as twofold coincidences, which can be done for Gaussian states. Note that as the degrees of second order coherence in Eq. (3) are measured between the pump and the read pulse, they are applied to this Gaussian state, not to the heralded, non-Gaussian entangled state $|\Psi\rangle \sim |A\rangle + e^{i\theta}|B\rangle$. We ensure that the mechanical states at the beginning of our protocol are Gaussian by allowing sufficiently long thermalization times (7x the mechanical decay time) prior to any optical manipulations. Consequently, the initial state is thermal, which for a bosonic system [52, 57] implies Gaussian quadrature statistics [79]. Next, all optomechanical interactions involved in our protocol are linear [55], therefore conserving the Gaussianity of the state [79]. Specifically, the Stokes process is described by the linear interaction Hamiltonian $\hat{H}_S \propto g_0\hat{m}_i^{\dagger}\hat{o}_i^{\dagger} + h.c.$ and the anti-Stokes process by $\hat{H}_{AS} \propto g_0\hat{m}_i\hat{o}_i^{\dagger} + h.c.$ for device $i = \mathrm{A},\mathrm{B}$ with the annihilation (creation) operator of optical resonance $\hat{o}_i$ ($\hat{o}_i^{\dagger}$).

Unintentional interactions, like absorption heating, happen probabilistically and in a remote frequency regime, such that it effectively acts as a Gaussian thermal bath [52, 76]. Though not strictly contributing to the mechanical state, we also consider false positive detection events: drive photons leaking through the filter stages can be described by a coherent state (with Gaussian intensity fluctuations). Detection of stray photons

and electrically caused false positive events are rare (~0.3% of the total count rate in the detection window) and uncorrelated (autocorrelation $g^{(2)}(0) = 1.05 \pm 0.09$), such that it is reasonable to model them as a Gaussian process as well. More specifically, we observe an average added noise of ~0.14 phonons during the measurement, from which the individual contributions of leaked drive photons, background detection events, and optical absorption heating can be estimated with additional measurements (for details see the section on "Second Order Coherence and Entanglement"). With the latter being a thermal process and therefore yielding Gaussian quadrature statistics, and an estimation of the initial thermal occupation from the nominal cryostat temperature, this leaves $\sim 4^{+2.8}_{-2.7} \cdot 10^{-2}$ phonons in device A and $\sim 0^{+1.4}_{-0} \cdot 10^{-2}$ in device B of unidentified origin. These are likely thermal phonons stemming from the non-ideal thermalization of the chips with their environment [52, 57].

For the modes leaving the interferometer $\hat{r}_j$, $\hat{p}_j$, reference [78] assumes an ideal 50/50 beamsplitter with equal powers on each input. Small experimental deviations from this idealized scenario result in quadratic corrections to the witness. For example, when the ratio of read photons at the beamsplitter originating from devices A and B is $1+\delta$, the measurable upper bound changes to $R_m(1+\delta^2/2) \geq R$ for small δ. In our experimental setup, we choose a fused fiber beamsplitter with a measured deviation of 0.6%, leading to a relative correction on the order of 10^{-5}. Experimentally, we cannot achieve power balancing at the input of the beamsplitter for photons scattered from the pump and the read pulses at the same time because the devices have slightly different thermal occupation. We choose to match the detection rates of heralding photons, i.e. photons scattered by the pump pulse. This preserves the unknown origin of the heralding photons. Differences in the optomechanical coupling strength and optical losses on the path from the device to the combining beamsplitter are compensated by adjusting the drive power in each path. After the balancing procedure, the relative difference in count rates of heralding photons is below 2%, limited by the measurement precision during the balancing run and laser power fluctuations during the measurements. This leads to a relative correction of the witness below 10^{-3}. The slightly different heating dynamics between devices A and B result in a measured flux ratio deviation of the scattered readout photons of $\delta \sim 5-10\%$. It can easily be seen from Eq. 4.3 that an increased heating will increase the witness R_m, and therefore the heating induced imbalance does not limit the validity of the witness. Yet, neglecting the thermal origin of the imbalancing, employing the correction $R_m(1+\delta^2/2) \geq R$, we obtain a relative systematic correction of 0.5% to our result in the worst case scenario. Adding all systematic errors, we obtain a conservative upper bound of all relative systematic corrections of ~0.5%. Consequently, we use a reduced classicality bound of $R_m \geq 0.995$ instead of 1, reducing the confidence level slightly from 99.84% to 99.82%.

4.5.6. STATISTICAL ANALYSIS

Results in the text and figures are given as maximum likelihood values and, where applicable, with a confidence interval of ±34% around this value. For the second order coherences $g^{(2)}_{ri,pj}$, $(i,j = 1,2)$, we apply binomial statistics based on the number of counted two-fold coincidences, which dominates the statistical uncertainty [57]. The entanglement witness $R_m(\theta, j)$ in Eq. (3) is a non-trivial function of multiple such $g^{(2)}_{ri,pj}$, ex-

pressed here as $R_{\mathrm{m}}(\theta, j) \equiv \mathcal{R}_{\mathrm{m}}\left(g^{(2)}_{r1,pj}(\theta), g^{(2)}_{r2,pj}(\theta)\right)$. To estimate its confidence intervals, we discretize the probability density function of the second order coherences $P(g^{(2)}_{ri,pj} \in [a; a+\delta a])$ at equidistant $a = n\delta a, n \in \mathbb{N}$. The probabilities for finding R_{m} in an interval $[f, f+\delta f]$ is then given by $P(R_{\mathrm{m}} \in [f, f+\delta f]) = \sum_{(a,b)\in\mathcal{M}} P(g^{(2)}_{r1,pj} \in [a, a+\delta a]) P(g^{(2)}_{r2,pj} \in [b, b+\delta b])$ on the set $\mathcal{M}$ for which $\mathcal{R}_{\mathrm{m}}(a,b) \in [f, f+\delta f] \forall (a,b) \in \mathcal{M}$. For the optimal read phase θ_{opt} we obtain as maximum likelihood values for the witness bounds $R_{\mathrm{m}}(\theta_{\mathrm{opt}}, 1) = 0.612^{+0.152}_{-0.057}$ and $R_{\mathrm{m}}(\theta_{\mathrm{opt}}, 2) = 0.846^{+0.210}_{-0.090}$. We obtain the symmetrized witness by treating the experimentally observed $R_{\mathrm{m}}(\theta_{\mathrm{opt}}, 1)$ and $R_{\mathrm{m}}(\theta_{\mathrm{opt}}, 2)$ as two independent measurements of the expectation value $R_{\mathrm{m,\,sym}}(\theta) \equiv \langle R_{\mathrm{m}}(\theta, 1)\rangle \stackrel{!}{=} \langle R_{\mathrm{m}}(\theta, 2)\rangle$ of the optomechanical state in a symmetric setup with no detector noise. For a realistic setup with detectors exhibiting different noise properties, without loss of generality, let detector j have more false positive detection events than detector i. We then find the symmetrized witness $\langle R_{\mathrm{m}}(\theta_{\mathrm{opt}}, i)\rangle \leq R_{\mathrm{m,\,sym}} \leq \langle R_{\mathrm{m}}(\theta_{\mathrm{opt}}, j)\rangle$ to be an upper bound to the entanglement witness of the state heralded by the better detector i. Consequently $1 > R_{\mathrm{m,\,sym}} \geq R_{\mathrm{m}}(\theta_{\mathrm{opt}}, i) \geq R$ implies entanglement between the two remote mechanical oscillators. The observed values yield a confidence level for $R_{\mathrm{m,\,sym}} < 1$ of 98.4%. When correcting for the conservative upper bound of systematic errors, see above, the confidence level for having observed entanglement remains at 98.3%.

The complete counting statistics of the witness measurement at θ_{opt} are accumulated over $N = 1.114 \cdot 10^9$ trials (i.e. sets of pulses). We obtain $C(p_1) = 111134$ and $C(p_2) = 184114$ counts for photons scattered by the pump pulse on detectors $i = 1,2$ and $C(r_1) = 108723$ and $C(r_2) = 167427$ counts from the read pulse. This yields the coincidence counts $C_{ri,pj}$, $(i, j = 1,2)$ for counts on detector i, heralded by detector j, $C_{r1,p1} = 9$, $C_{r2,p1} = 130$, $C_{r1,p2} = 129$, $C_{r2,p2} = 37$.

For non-optimal phases $\theta \neq \theta_{\mathrm{opt}}$, $R_{\mathrm{m}}(\theta, i) \geq R_{\mathrm{m}}(\theta_{\mathrm{opt}}, i)$. Consequently, by adding the photon counts of measurements from an interval $[\theta_1, \theta_2]$, the resulting $R_{\mathrm{m}}([\theta_1, \theta_2], i) \geq R_{\mathrm{m}}(\theta \in [\theta_1, \theta_2], i)$ serves as an upper bound to any phase θ within that interval. Including the measurements at the non-optimal phase $\Delta\phi = 0$, we obtain $R_{\mathrm{m}}([\theta_{\mathrm{opt}} - 0.2\pi, \theta_{\mathrm{opt}}], 1) = 0.66^{+0.114}_{-0.055}$ and $R_{\mathrm{m}}([\theta_{\mathrm{opt}} - 0.2\pi, \theta_{\mathrm{opt}}], 2) = 0.806^{+0.129}_{-0.071}$, resulting in $R_{\mathrm{m,\,sym}}([\theta_{\mathrm{opt}} - 0.2\pi, \theta_{\mathrm{opt}}]) = 0.74^{+0.08}_{-0.05} \geq R_{\mathrm{m,\,sym}}(\theta_{\mathrm{opt}})$. The confidence level for $R_{\mathrm{m,\,sym}} < 1$ is 99.84%, dropping to 99.82% when correcting for the conservative upper bound for systematic errors. Note that for states heralded only with the more efficient detector 1, we already have a confidence level for entanglement between the two mechanical oscillators of 99.50%, including corrections for systematic errors.

The statistics of the witness within the extended phase region are obtained from $N = 1.949 \cdot 10^9$ experimental trials. We get $C(p_1) = 196080$ and $C(p_2) = 322608$ counts for photons scattered by the pump pulse on detectors $i = 1,2$ and $C(r_1) = 194023$ and $C(r_2) = 300373$ counts from the read pulse. This yields the coincidence counts $C_{ri,pj}$, $(i, j = 1,2)$ for counts on detector i, heralded by detector j, $C_{r1,p1} = 16$, $C_{r2,p1} = 223$, $C_{r1,p2} = 242$, $C_{r2,p2} = 67$.

4.5.7. SECOND ORDER COHERENCE AND ENTANGLEMENT

The second order coherence between the scattered photons from the pump pulse and signal phonons transferred by the read pulse after a delay t, $g^{(2)}_{i,rp}(t) = \langle \hat{r}^\dagger_{\mathrm{j}} \hat{p}^\dagger_{\mathrm{j}} \hat{r}_{\mathrm{j}} \hat{p}_{\mathrm{j}} \rangle / \langle \hat{r}^\dagger_{\mathrm{j}} \hat{r}_{\mathrm{j}} \rangle \langle \hat{p}^\dagger_{\mathrm{j}} \hat{p}_{\mathrm{j}} \rangle$,

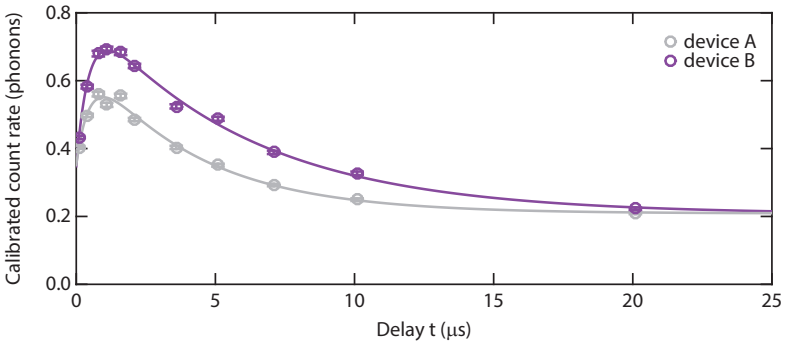

Figure 4.7: Pump-probe experiment. The experiment reveals the response of the devices mechanical modes to the initial optical pump. See text for details. Error bars are s.d.

of the individual devices $i = A, B$, allows to us quantify the total noise contribution limiting the interference visibility. The measurements are performed the same way as described in the main text, however with the optical path to the other device blocked (see Fig. 2). Though there is no fundamental difference between the detectors $j = 1, 2$, we only use detector $j = 2$ for the single device measurements. Following [90] and starting from a thermal state for the mechanical system ρ_m and vacuum $|0\rangle\langle 0|_o$ in the optical sidebands we obtain in the low temperature limit

$$g^{(2)}_{i,rp}(t) \approx 1 + \frac{e^{-\Gamma_i t}}{n_{i,\mathrm{th}}(t) + p_{\mathrm{pump},i} \cdot e^{-\Gamma_i t} + n_{\mathrm{leak}} + n_{\mathrm{bg}}}, \tag{4.5}$$

where $n_{i,\mathrm{th}} \ll 1$ is the mean phonon occupation of the device, $p_{\mathrm{pump},i} \ll n_{\mathrm{th}}$ is the Stokes excitation probability, $n_{\mathrm{leak}} \ll n_{\mathrm{th}}$ is the average number of leaked pump photons per transferred phonon, and $n_{\mathrm{bg}} \ll n_{\mathrm{th}}$ is the average number of background counts per detected phonon. At a delay of $\tau = 123$ ns $\ll 1/\Gamma_i$ we measure $g^{(2)}_{\mathrm{A,rp}} = 7.1^{+1.2}_{-0.9}$ and $g^{(2)}_{\mathrm{B,rp}} = 9.6^{+1.1}_{-0.9}$. With calibrated rates of $n_{\mathrm{bg}} = 3 \cdot 10^{-3}$, $p_{\mathrm{pump,A}} = 0.56 \cdot 10^{-2}$, $p_{\mathrm{pump,B}} = 0.80 \cdot 10^{-2}$ and leaks at detector 1 $n_{\mathrm{leak},1} = 4.2 \cdot 10^{-2}$ and detector 2 $n_{\mathrm{leak},2} = 3.2 \cdot 10^{-2}$ we can estimate the number of incoherent phonons to be $n_{\mathrm{th,A}} = 11.9^{+2.8}_{-2.7} \cdot 10^{-2}$ for device A and $n_{\mathrm{th,B}} = 6.9^{+1.4}_{-1.3} \cdot 10^{-2}$ for device B. In a more detailed analysis, including the mechanical decay measurement (see below), we can estimate that absorption by the pump pulse contributes $n_{\mathrm{pump}} \sim 3 \cdot 10^{-2}$ phonons and absorption from the read pulse contributes $n_{\mathrm{read}} \sim 5 \cdot 10^{-2}$ phonons. This suggest, that the performance of device A is limited by imperfect thermalization with the cryostat at a temperature of 60 mK.

The interference contrast of the entangled state, i.e. $C_{\mathrm{e}}(t) = \max(g^{(2)}_{ri,pj}(t,\theta)) - \min(g^{(2)}_{ri,pj}(t,\theta))$ is bound by the cross correlation of the individual devices $C_{\mathrm{e,max}}(t) \approx \min(g^{(2)}_{\mathrm{A},rp}(t), g^{(2)}_{\mathrm{B},rp}(t)) - 1$ [91]. A pump-probe measurement of the thermal response of the devices [57] allows us to predict the cross correlations and thus an upper bound to the interference contrast. We excite the devices with a blue detuned pump pulse with $p_{\mathrm{pump,A}} = 2.8\%$ ($p_{\mathrm{pump,B}} = 4.0\%$) and vary the delay of a read (or probe) pulse with 5.6% (8.0%) state

swap fidelity for device A (B). Note that for this experiment, we deliberately choose pulse energies higher than for the interference experiments in order to reduce the measurement time. As is done for sideband asymmetry [52, 57], the scattering rate of the probe pulse can be converted into the number of phonons at time t, when using the rate of the pump pulse (after scaling the signal according to the pump-to-probe power ratio) as a reference signal of single-phonon strength. This is only valid when $n_{\mathrm{th}} \ll 1$ at the time of pump pulse, which we find is the case later in the section. The results of these measurements are shown in Figure 4.7. We observe an initial rise in phonon occupation after the pump pulse, followed by a decay to an equilibrium state. The delayed heating can be understood by the presence of long lived high frequency phonons, which weakly couple to the 5 GHz modes under investigation. We model these high frequency phonons by an effective thermal bath, exponentially decaying with rate γ_i. This results in the rate equation $\dot{n}_i(t) = -\Gamma_i n_i(t) + k_i e^{-\gamma_i t} + \Gamma_i n_{i,\mathrm{init}}$ of the mean occupation number n_i of device i = A,B. The additional bath couples with strength k_i, and the thermal environment of the chip has an equilibrium temperature of $n_{i,\mathrm{init}}$. The detected signal of the probe pulse $d_i(t) = n_{i,\mathrm{pump}}(t) + n_{i,\mathrm{final}}$ contains the average phonon number $n_{i,\mathrm{pump}}(t) = n_i(t) - n_{i,\mathrm{init}}$ induced by the pump beam, as well as a constant offset $n_{i,\mathrm{final}} = n_{i,\mathrm{init}} + n_{\mathrm{i,probe}} + n_{\mathrm{leak}} + n_{\mathrm{bg}}$ given by the thermal environment $n_{i,\mathrm{init}}$, the false positive events n_{leak} and n_{bg} and the heating during the probe pulse itself $n_{\mathrm{i,probe}}$. Consequently, we fit the pump-probe data with the general solution of the above differential equation $d_i(t) = a_i \cdot e^{-\Gamma_i t} - b_i \cdot e^{-\gamma_i t} + n_{i,\mathrm{final}}$, with a_i, b_i fitting parameters and including the offset $n_{i,\mathrm{final}}$ of the probe pulse detection rate. We obtain $1/\Gamma_A = 4.0$ μs, $1/\Gamma_B = 5.8$ μs, $1/\gamma_A = 0.5$ μs and $1/\gamma_B = 0.5$ μs. Using the calibrated false positive detection rates and estimating the equilibrium occupation from the thermal environment $n_{i,\mathrm{init}} \sim 1/(e^{\hbar\Omega/k_B T} - 1)$, with the Boltzmann constant k_B and cryostat temperature T, we can obtain the individual contributions to the absorption heating by the pump ($n_{i,\mathrm{pump}}$) and the probe pulse ($n_{i,\mathrm{probe}}$) for any given delay t. Adapting the number of phonons added by the optical drive pulses $n_{i,\mathrm{pump}}$ and $n_{i,\mathrm{probe}}$ for the lower energies, under the assumption of linear absorption and optomechanical processes, we obtain an estimate of the thermal occupation $n_{i,\mathrm{th}}(t) = n_i(t) + n_{i,\mathrm{probe}} - p_{\mathrm{pump},i} e^{-\Gamma_i t}$ during the entanglement experiment. Using the calibrated rates and equation (4.5), we can obtain an upper bound to the interference contrast $C_{\mathrm{e,max}}$ (see above) and therefore also for the visibility $V_{\mathrm{max}} = C_{\mathrm{e,max}}/(C_{\mathrm{e,max}} + 2)$, which is shown in Figure 4.4.

4.5.8. RATES AND EXTRAPOLATION OF RESULTS

In order to highlight the scalability of the mechanical entanglement, we recapitulate the detection rates in the entanglement witness measurement. The experiment is repeated every 50 μs, limited by the thermalization time of the mechanical modes. Using the counting statistics of the measurement at the optimal phase θ_{opt}, see above, we have a probability of $p_{\mathrm{herald}} \approx 2.7 \cdot 10^{-4}$ and the unconditional probability to also detect the anti-Stokes photon from the readout pulse of $p_{\mathrm{read}} \approx 2.8 \cdot 10^{-7}$. These probabilities contain the optomechanically generated photons, leaked pump photons and background counts. In the current setup these rates are limited by losses in the filtering setup and low optomechanical scattering rates to retain the effects of absorption heating. When the two mechanical devices are placed in two separate refrigerators and placed in different loca-

tions, additional fiber would be inserted, causing additional losses. While the detection rate of leaked pump photons reduces in the same manner as the of the optomechanical photons, the rate of background counts stays the same. Consequently, the signal-to-noise ratio reduces, lowering the normalized cross-correlation between Stokes and anti-Stokes photons. In the present measurements, the inverse signal-to-background ratio is $n_{\mathrm{bg},1} = 2.9 \cdot 10^{-3}$ ($n_{\mathrm{bg},2} = 3.2 \cdot 10^{-3}$) for detectors 1 (2). The most reliable estimate of the second order coherence of device A, which has worse properties, can be extracted from the observed interference contrast, resulting in $g^{(2)}_{A,\mathrm{rp}} \sim 7.5 \pm 0.35$, as it has better statistics than the direct measurement. For device B, we use the direct measurement $g^{(2)}_{B,\mathrm{rp}} = 9.6^{+1.1}_{-0.9}$. To maintain an interference contrast of 95% of the current level, the second order coherence of both devices is allowed to decrease to ~7.1. With equation (4.5) we can estimate that an additional loss of 5.4 dB (10.6 dB) loss in the optical path from device A (B) to the combining beamsplitter decreases the signal-to-background ratio, such that $g^{(2)}_{A,rp} \approx g^{(2)}_{B,rp} \approx 7.1$. Using the nominal attenuation of commercial low-loss telecom fiber (Corning SMF-28 ULL ~0.17 dB/km), we can estimate that an additional fiber length of 94^{+8}_{-12} km could be inserted between the devices. The projected entanglement witness in this configuration is $R_m \sim 0.76$ and would need roughly the same number of coincidence events to clear the classicality bound of 1 by 3 standard deviations. Including the reduced scattering rates from matching both paths, this would require ~170 days of integration time, including a 15% overhead time for stabilization of filters and interferometer as well as data management. Reducing the separation distance to 75 km, i.e. an additional fiber length of 32 km (43 km) between device A (B) and the beamsplitter, requires 38 days of continuous measurement time for a statistically significant demonstration of remote entanglement. While our cryostat currently only allows for a few weeks of measurements at a time due to technical limitations, much longer times should in principle be easily achievable.

5

AN OPTOMECHANICAL BELL TEST

Igor MARINKOVIĆ, Andreas WALLUCKS, Ralf RIEDINGER, Sungkun HONG, Markus ASPELMEYER, Simon GRÖBLACHER

Over the past few decades, experimental tests of Bell-type inequalities have been at the forefront of understanding quantum mechanics and its implications. These strong bounds on specific measurements on a physical system originate from some of the most fundamental concepts of classical physics – in particular that properties of an object are well defined independent of measurements (realism) and only affected by local interactions (locality). The violation of these bounds unambiguously shows that the measured system does not behave classically, void of any assumption on the validity of quantum theory. It has also found applications in quantum technologies for certifying the suitability of devices for generating quantum randomness, distributing secret keys and for quantum computing. Here we report on the violation of a Bell inequality involving a massive, macroscopic mechanical system. We create light-matter entanglement between the vibrational motion of two silicon optomechanical oscillators, each comprising approx. 10^{10} *atoms, and two optical modes. This state allows us to violate a Bell inequality by more than 4 standard deviations, directly confirming the non-classical behavior of our optomechanical system under the fair sampling assumption.*

This work was published in *Optomechanical Bell Test.* I. Marinković, A. Wallucks, R. Riedinger, S. Hong, M. Aspelmeyer, and S. Gröblacher. Phys. Rev. Lett. **121**, 220404 (2018)

5.1. INTRODUCTION

Bell's theorem [92] predicts that any local realistic theory is at variance with quantum mechanics. It was originally conceived to settle an argument between Einstein [93] and Bohr [94] on locality in physics, and to investigate the axioms of quantum physics. First tests of the Clauser-Horne-Shimony-Holt (CHSH) inequality [95], an experimentally testable version of Bell's original inequality, were performed with photons from cascaded decays of atoms [96, 97] and parametric down-conversion [98–100]. Subsequent experiments reduced the set of assumptions required for the falsification of classical theories, closing, e.g., the locality [101] and detection loopholes [102], first individually and recently simultaneously [70, 103–105]. In addition to the fundamental importance of these experiments, the violation of a Bell-type inequality has very practical implications – in particular, it has become the most important benchmark for thrust-worthily verifying entanglement in various systems [106, 107], including mesoscopic superconducting circuits [108], for certifying randomness [109, 110], secret keys [111], and quantum computing [112].

While the standard form of quantum theory does not impose any limits on the mass or size of a quantum system [113], the potential persistence of quantum effects on a macroscopic scale seems to contradict the human experience of classical physics. Over the past years, quantum optomechanics has emerged as a new research field, coupling mechanical oscillators to optical fields. While these systems are very promising for quantum information applications due to their complete engineerability, they also hold great potential to test quantum physics on a new mass scale. Recent experiments have demonstrated quantum control of such mechanical systems, including mechanical squeezing [73], single-phonon manipulation [16, 17, 52, 74], as well as entanglement between light and mechanics [72] and entanglement between two mechanical modes [75, 114, 115]. However, explaining the observed results in these experiments required assuming the validity of quantum theory at some level. A Bell test, in contrast, is a genuine test of non-classicality without quantum assumptions.

Here we report on the first Bell test using correlations between light and microfabricated mechanical resonators, which constitute massive macroscopic objects, hence verifying non-classical behavior of our system without relying on the quantum formalism. Bell-tests do not require assumptions about the physical implementation of a quantum system such as the dimension of the underlying Hilbert space or the fundamental interactions involved in state preparation and measurement [116]. The violation of a Bell-inequality is hence the most unambiguous demonstration of entanglement with numerous important implications. From a fundamental perspective, the robust entanglement between flying optical photons and a stored mechanical state rules out local hidden-variables, which can be used for further tests of quantum mechanics at even larger mass scales [117, 118]. From an application perspective, the presented measurements also imply that optomechanics is a promising technique to be used for quantum information processing tasks including teleportation, quantum memories and the possibility of quantum communication with device-independent security [111].

5.2. METHODS

The optomechanical structures used in this work are two photonic crystal nanobeams on two separate chips. They are designed to have an optical resonance in the telecom band that is coupled to a co-localized, high-frequency mechanical mode [119]. Each device is placed in one of the arms of an actively stabilized fiber interferometer (see [114] and SI for additional details). The resonators are cryogenically cooled close to their motional ground state inside a dilution refrigerator. Our entanglement creation and verification protocol consists of two optical control pulses that give rise to linearized optomechanical interactions, addressing the Stokes and anti-Stokes transitions of the system (see Figure 5.1). Both types of interactions result in scattered photons that are resonant with the cavity and can be efficiently filtered from the drive beams before being detected by superconducting nanowire single photon detectors (SNSPDs).

A blue detuned, ~40 ns long laser pulse with frequency $\nu_b = \nu_o + \nu_m$ (ν_o optical resonance, ν_m mechanical resonance) generates photon-phonon pairs. The interaction in this case is described by $\hat{H}_b = -\hbar g_0 \sqrt{n_b}\hat{a}^\dagger \hat{b}^\dagger + \text{h.c.}$, with the intracavity photon number n_b, the optomechanical single photon coupling g_0 and the optical (mechanical) creation operators $\hat{a}^\dagger$ ($\hat{b}^\dagger$). This correlates the number of mechanical and optical excitations in each of the arms of the interferometer as

$$|\psi\rangle \propto (|00\rangle_{om} + \epsilon|11\rangle_{om} + \mathcal{O}(\epsilon^2)), \tag{5.1}$$

where o denotes the optical and m the mechanical mode, while $p = \epsilon^2$ is the excitation probability. For small $p \ll 1$, states with multiple excitations are unlikely to occur, and can therefore be neglected in the statistical analysis. Driving the devices simultaneously and post-selecting on trials with a successful detection of both the Stokes-photon and the phonon, we approximate the combined state as

$$\begin{aligned} |\Psi\rangle &= \frac{1}{\sqrt{2}}(|11\rangle_A|00\rangle_B + e^{i\phi_b}|00\rangle_A|11\rangle_B) \\ &= \frac{1}{\sqrt{2}}(|AA\rangle_{om} + e^{i\phi_b}|BB\rangle_{om}), \end{aligned} \tag{5.2}$$

again neglecting higher order excitations. Here ϕ_b is the phase difference that the blue drives acquire in the two interferometer paths A and B, including the phase shift of the first beam splitter. Expressing the state in a path basis $|A\rangle_x = |10\rangle_{AB}$, where x is o for the photonic and m for the phononic subsystem in arm A and B, allows to identify the Bell-state, similarly to polarization entanglement in optical down-conversion experiments. Unlike the two mode entangled mechanical state in [114], this four-mode entangled optomechanical state allows us to realize a Bell measurement of the type suggested by Horne, Shimony and Zeilinger [120] and first demonstrated by Rarity and Tapster [99] involving two-particle interference between four different modes. In order to access interferences between the mechanical modes, we convert the phonons into photons using a red detuned laser pulse (duration ~40 ns, drive frequency $\nu_r = \nu_o - \nu_m$). This realizes an optomechanical beamsplitter interaction which allows for a state transfer ($\hat{H}_r = -\hbar g_0 \sqrt{n_r}\hat{a}^\dagger \hat{b} + \text{h.c.}$, with the intracavity photon number n_r). Note that this can also be described as a classical mapping process. The optical readout fields in the interferometer arms are again recombined on a beam splitter, after which the state of Stokes

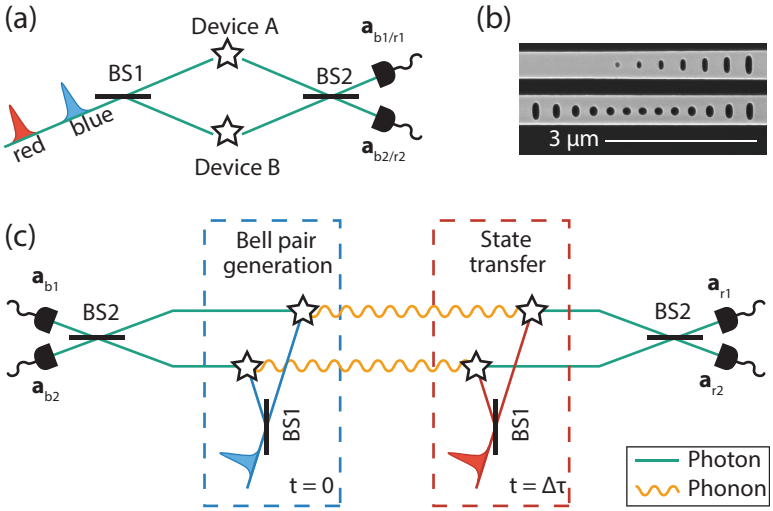

Figure 5.1: (a) Schematic of the setup: blue detuned drive pulses interact with the mechanical resonators (devices A & B) producing entangled photon-phonon pairs. The light-matter entanglement is in the path basis (A or B), corresponding to the device in which the Stokes scattering event took place. The generated photons are detected in single-photon detectors giving the measurement results a_{b1} and a_{b2}. The detection of the phonons is done by transferring their states to another optical mode by using a red drive after some time $\Delta\tau$ and subsequently obtaining the results a_{r1} and a_{r2}. Note that for technical reasons the photons created by the blue and red drives are detected on the same pair of detectors, but with a time delay $\Delta\tau = 200$ ns. Therefore we have time-separation of the two parties of the Bell test instead of space-separation (as commonly done). BS1/2 represent beamsplitter 1/2. (b) Scanning electron microscope image of one of the optomechanical devices, represented with a star-symbol in (a) and (c), next to the coupling waveguide (top). (c) Illustration of our experimental sequence: one party of the Bell test measures in which detector path the Stokes photon is found at time $t = 0$, while the other performs the same measurement for the anti-Stokes photon after a time $t = \Delta\tau$. We probe their correlations in order to violate the CHSH inequality. Since the two photons never interacted directly (only through the mechanics), the observed correlations are a direct consequence of the correlations between the Stokes photons and phonons.

/ anti-Stokes field is

$$|\Phi\rangle = \frac{1}{2\sqrt{2}}[(1-e^{i(\phi_b+\phi_r)})(\hat{a}^\dagger_{r1}\hat{a}^\dagger_{b1} - \hat{a}^\dagger_{r2}\hat{a}^\dagger_{b2}) + i(1+e^{i(\phi_b+\phi_r)})(\hat{a}^\dagger_{r1}\hat{a}^\dagger_{b2} + \hat{a}^\dagger_{r2}\hat{a}^\dagger_{b1})]|0000\rangle. \quad (5.3)$$

Here we express the detected fields in terms of their creation operators with labels b (r) for photons scattered from the blue (red) drive and 1 (2) for the two detectors (cf. Figure 5.1). Furthermore ϕ_r is the phase difference that the red detuned pulse photons acquire in the two arms of the interferometer. Since experimentally the mechanical frequencies of the devices differ by a small offset $\Delta\nu_m$ (see below), the state acquires an additional phase $\Omega = \Delta\nu_m\Delta\tau$, where $\Delta\tau$ is the delay between the blue and red pulses. In all data below, however, we keep $\Delta\tau$ fixed such that we can treat it as constant and set $\Omega = 0$. Typically, Bell experiments are done by rotating the measurement basis in which each particle is detected. Equivalently, the state itself can be rotated, while keeping the measurement basis fixed. In our experiment we choose the latter option, as this

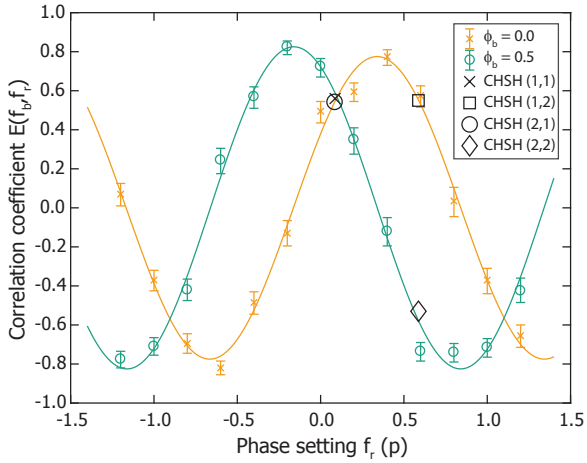

Figure 5.2: Correlation coefficients for various phase settings. We set the blue phase parameter ϕ_b to 0 (orange) and 0.5π (green), while we scan the red pulse's phase setting ϕ_r over more than 2π. The optimal angles to test the CHSH inequality are shown with different symbols. The associated measured values can be found in Table 5.1.

5

is simpler to implement in our setup. We achieve this by applying a phase shift with an electro-optical modulator (EOM) in arm A of the interferometer, with which we can vary ϕ_b and ϕ_r independently (see SI). This allows us to select the relative angles between the photonic and phononic states.

In our experiment, the optical resonances are at a wavelength of $\lambda = 1550.4$ nm with a relative mismatch of $\Delta\nu_o \approx 150$ MHz. The mechanical modes have frequencies of $\nu_m = 5.101$ GHz and 5.099 GHz for device A and B, respectively. The bare optomechanical coupling rate $g_0/2\pi$ is 910 kHz for device A and 950 kHz for device B. While the optical mismatch is much smaller than the linewidth $\Delta\nu_o \ll \kappa \sim 1$ GHz such that the devices are sufficiently identical, the mechanical mismatch requires optical compensation. This is realized using the EOM in arm A of the interferometer to ensure that the scattered photons from each arm interfere with a well defined phase on the second beamsplitter (see also SI).

At the base temperature of the dilution refrigerator of around 12 mK we obtain the phonon temperature of the mechanical modes by performing sideband asymmetry measurements [57]. The measured thermal occupations for both devices is $n_{init} \leq 0.09$. We determine the lifetimes of the phonons in our structures to be $\tau_A = 3.3 \pm 0.5$ μs and $\tau_B = 3.6 \pm 0.7$ μs using a pump-probe type experiment in which we excite the devices and vary the delay to the readout pulse. To re-initialize the devices in their groundstates prior to each measurement trial, we repeat the drive sequence every 50 μs, leaving more than 10 times their lifetime for thermalization with the environment. Furthermore, we set the delay between the blue and red detuned pulses to $\Delta\tau = 200$ ns. The pulse energies for the Bell inequality experiment are chosen such that the excitation probability is 0.8% (1%), while the readout efficiency is 3% (4.1%) for device A (device B). These probabilities match the number of optomechanically generated photons for each device at the

Settings i,j	$\phi_b^i[\pi]$	$\phi_r^j[\pi]$	$E(\phi_b,\phi_r)$
(1,1)	0.0	0.087	$0.561^{+0.019}_{-0.020}$
(1,2)	0.0	0.587	$0.550^{+0.020}_{-0.022}$
(2,1)	0.5	0.087	$0.542^{+0.018}_{-0.021}$
(2,2)	0.5	0.587	$-0.523^{+0.021}_{-0.021}$

Table 5.1: Correlation coefficients for the optimal CHSH angles. The violation of the inequality can be computed according to Eq. (5.5) and results in a S value of $S = 2.174^{+0.041}_{-0.042}$, corresponding to a violation of the classical bound by more than 4 standard deviations.

beamsplitter.

To characterize the performance of the devices, we first perform cross-correlation measurements of the photons scattered from blue and red drives on each individual optomechanical system. With the above mentioned settings, we obtain normalized cross-correlation values of $g^{(2)}_{\mathrm{br,A}} = 9.3 \pm 0.5$ and $g^{(2)}_{\mathrm{br,B}} = 11.2 \pm 0.6$ [57]. We can use this to estimate the expected interferometric visibility for the experiments below as $V_{\mathrm{xpcd}} = \frac{g^{(2)}_{\mathrm{br}}-1}{g^{(2)}_{\mathrm{br}}+1}$ [121]. As there is a small mismatch in the observed cross-correlations of the two devices, we use the smaller value of device A, which results in an expected visibility of around $V_{\mathrm{xpcd}} = 81\%$.

In order to experimentally test a Bell inequality, we then drive the two devices simultaneously in a Mach-Zehnder interferometer (see Figure 5.1 and SI). We define the correlation coefficients

$$E(\phi_b,\phi_r) = \frac{n_{11}+n_{22}-n_{12}-n_{21}}{n_{11}+n_{22}+n_{12}+n_{21}}. \tag{5.4}$$

Here n_{ij} represents the number of detected coincidences scattered from blue (i) and red (j) pulses on the two detectors ($i,j = 1,2$), such that e.g. n_{21} is the number of trials where the blue drive resulted in an event on detector 2, whereas the consecutive red drive on detector 1. The visibility V is given as the maximum correlation coefficient $V = |E(\phi_b,\phi_r)|_{\mathrm{max}}$. We measure the correlation coefficients for various phase settings for the blue (ϕ_b) and red (ϕ_r) pulses, as shown in Figure 5.2. Strong correlations in the detection events by photons scattered from blue and red pump pulses can be seen, of which the latter are a coherent mapping of the mechanical state of the resonator. This sweep demonstrates that we are able to independently shift the phases for the Stokes and anti-Stokes states. The visibility $V = 80.0 \pm 2.5\%$ we obtain from fitting the data matches the prediction from the individual cross-correlation measurements very well. The interference furthermore shows the expected periodicity of 2π.

5.3. RESULTS

To test possible local hidden-variable descriptions of our correlation measurements we use the CHSH-inequality [95], a Bell-type inequality. Using the correlation coefficients $E(\phi_b,\phi_r)$, it is defined as

$$S = |E(\phi_b^1,\phi_r^1) + E(\phi_b^1,\phi_r^2) + E(\phi_b^2,\phi_r^1) - E(\phi_b^2,\phi_r^2)| \leq 2. \tag{5.5}$$

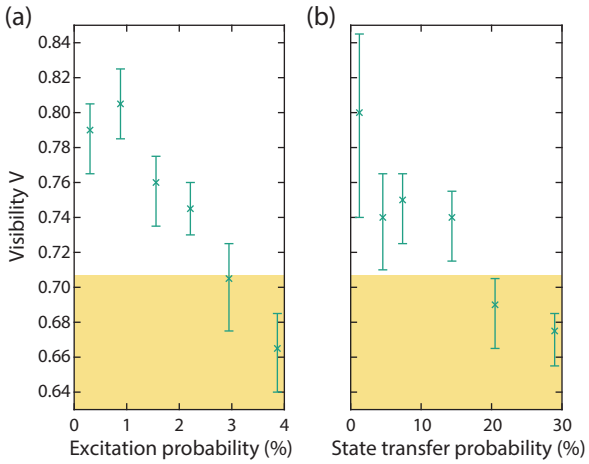

Figure 5.3: Visibility as a function of generation rate and state transfer probability. We sweep the power of the blue pulse while keeping the red state transfer probability fixed, inducing absorption of the optical field in the silicon structure, and see that for excitation probabilities up to around 3% the measured visibility exceeds the threshold to violate the CHSH inequality (left). When increasing only the red pump power (right) a similar behavior can be observed, allowing us to increase the state transfer probability beyond 14%, while still being able to overcome the classical bound (orange shaded region). The visibilities $V = |E(\phi_b, \phi_r)|_{max}$ are measured in a single phase setting at the optimal angles $\phi_b = 0$ and $\phi_r = 0.337\pi$.

A violation of this bound allows us to exclude a potential local realistic theory from describing the optomechanical state that we generate in our setup. The maximal violation $S_{QM} = 2\sqrt{2} \cdot V$ is expected for settings $\phi_b^i = [0, \pi/2]$ and $\phi_r^j = [-\pi/4 + \phi_c, \pi/4 + \phi_c]$, with $i, j = 1, 2$ [122]. Here $\phi_c = 0.337\pi$ is an arbitrary, fixed phase offset that is inherent to the setup. Our experimentally achieved visibility exceeds the minimal requirement for a violation of the classical bound $V \geq 1/\sqrt{2} \approx 70.7\%$. We proceed to directly measure the correlation coefficients in the four settings, as indicated in Figure 5.2, and obtain $S = 2.174^{+0.041}_{-0.042}$ (cf. Table 5.1). This corresponds to a violation of the CHSH inequality by more than 4 standard deviations, clearly confirming the non-classical character of our state. From the observed visibility of $V = 80.0\%$, we would expect a slightly stronger violation with $S \approx 2.26$. The reduction in our experimentally obtained value for S can be attributed to imperfect filtering of drive photons in front of one of the SNPSDs, which gives rise to varying amounts of leak photons at different phase settings (see discussion in SI).

For quantum network applications it is also important to analyze the quality of the detected optomechanical entanglement with regard to the detection rate. In our measurements we can achieve this by changing the energies of the drive beams to alter the optomechanical interaction strengths. An increase in the blue pulse energy is accompanied by two mechanisms that decrease the state fidelity. Firstly, the probability for higher order scattering events $\mathcal{O}(p_{A,B}^2)$ is increased. Secondly, higher pulse energies also result in more absorption, degrading the state through thermal excitations. As observed in previous experiments [57, 114], optical pumping of the devices creates a thermal population

of the mechanical modes with timescales on the order of several hundreds of nanoseconds (see also SI). While we keep the delay to the readout pulse short ($\Delta\tau$ = 200 ns), we cannot fully avoid these spurious heating effects. Hence the decrease in visibility with increased pulse energy, as seen in Figure 5.3(a), can be attributed mostly to this direct absorption heating. To further test the heating dynamics of our state, we also sweep the red pulse energies while keeping the excitation energy fixed at the value used in the main experiment (p_b = 0.8% and 1%). As expected, the increased readout pulse energies lead to substantial heating of the devices [52]. However, even for relatively large optical powers corresponding to ~14% read out efficiency, the correlation coefficient is above the threshold for violating a Bell inequality under the fair sampling assumption, see Figure 5.3(b).

Our system is fully engineered and hence we have complete control over the resonance frequencies and possibilities to integrate with other systems. While in our current structures we intentionally cap the mechanical quality factors to keep the measurement time short [81], recent experiments with very similar devices have observed lifetimes larger than 1 s [9]. Long lived non-classical states of large masses are interesting for fundamental studies of quantum mechanics. Combined with the fact that we can efficiently couple these states to photons in the telecom band could enable interesting experiments with Bell tests at remote locations. Employing fast optical switches that route one of the photons to a second set of detectors would furthermore allow us to close the locality loophole in the future. Our probabilistic scheme could, in principle, also be adapted to perform a 'loophole-free' Bell test [103], if in addition the detection loophole would be closed through a more efficient read-out.

5.4. CONCLUSION

In summary, we have demonstrated the violation of a Bell-type inequality using massive (around 10^{10} atoms), macroscopic optomechanical devices, thereby verifying the non-classicality of their state without the need for a quantum description of our experiment. The experimental scheme demonstrated here may also be employed in other, even more massive optomechanical systems. One outstanding challenge is to generate states of genuine macroscopic distinction, for example a macroscopic separation in the center of mass, to investigate fundamental decoherence mechanisms [123] or even the interplay between quantum physics and gravity [124, 125]. We also show that the created entangled states are relatively robust to absorption heating, which could lead to a realistic implementation of entanglement generation for a future quantum network using optomechanical devices. Violation of a CHSH inequality can also be used to verify long-distance quantum communication with device-independent security using mechanical systems.

5.5. SUPPLEMENTARY INFORMATION

5.5.1. EXPERIMENTAL SETUP

A sketch of the fiber-based setup used in the main text is shown in Figure 5.4. The pulse generation consists of two tunable diode lasers (Santec TSL550 and Toptica CTL1550), which are stabilized at the sidebands of device B using a wavelength meter. We suppress high frequency noise on both laser through optical filtering (linewidth ~50 MHz), before we generate the drive pulses using acousto-optic modulators (pulse length ~40 ns). The interferometer is formed by a variable ratio coupler and a calibrated 50:50 coupler (deviation below 3%). The interferometer has a free spectral range of 1.2 GHz and is phase-stabilized with a home built fiber stretcher. The EOM is used to select a desired phase on a fast timescale and simultaneously to compensate the frequency mismatch of the mechanical devices of $\Delta\nu_m = 2.3$ MHz. This mismatch is small enough to be compensated by a linear phase sweep during the pulses without the need of a serrodyne drive.

In order to achieve high efficiencies in our detection paths we use a home-built freespace filtering setup. Each filter line consists of two linear cavities which are actively stabilized to the resonance of the devices. The total detection efficiency for optomechanically scattered photons from device A is 3.4% for detector 1 and 2.9% for detector 2. The efficiency for device B is 2.9% for detector 1 and 2.3% for detector 2. The total loss budget consists of various contributions: photons that are created in one of the optomechanical cavities are transfered to an on-chip silicon waveguide with efficiencies of 65% and 55% for devices A and B, respectively. The transmission from the waveguide to the output of the circulator (59% and 55%) is dominated by waveguide to fiber coupling losses. The rest of the losses are due to a finite transmission through filters, optical components needed for feeding continuous locking light and finite detection efficiency of SNSPDs.

In order to evaluate the quality of our interferometer we record the first order interference of our lasers. For this, we detune the filters by ~2 GHz from the optomechanically scattered photons, such that we are only sensitive to leaked pump photons. We then lock the interferometer with the fiber stretcher and sweep the phase using the EOM as we do for the visibility sweep in Figure 5.1. The visibility we obtain of 98.4% matches well with the independently measured short term fluctuations of the interferometer lock of around $\sim\pi/25$ [126]. The main cause of these fluctuations is noise that is picked up by the fibers inside the dilution refrigerator stemming from the pulse tube cryo cooler.

5.5.2. PUMP FILTERING AND FALSE COINCIDENCES

To estimate the effect of erroneous coincidence clicks that do not stem from the optomechanical state, we perform calibration measurements to estimate the role of leaked drive photons. To do this, we slightly detune the filters away from the frequency of the optomechanicaly scattered photons, such that they are reflected from the filters and do not reach the SNSPDs. We find that during the main experiments around 17% of red counts detected on detector 2 are in fact imperfectly filtered drive photons. For detector 1 this number is around 7%. To understand this asymmetry, we note that the cavities in front of detector 1 both have linewidths of ~35 MHz, while the ones in front of detector 2 have a slightly larger linewidth of ~45 MHz. We estimate that perfect filtering would enable us to obtain roughly 12% higher cross correlation values for the individual

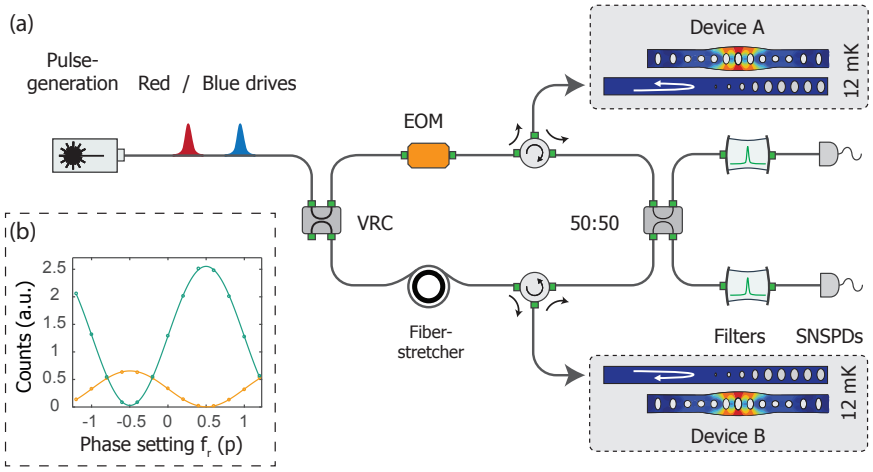

Figure 5.4: (a) Sketch of the setup. We first generate blue and red pulses that drive the optomechanical interactions. The devices are each placed in one arm of a fiber interferometer realized between a variable ratio coupler (VRC) and a 50:50 beamsplitter. We stabilize the overall phase with a fiber stretcher such that we can select particular phase settings with our EOM in arm A. The optomechanically generated photons are filtered from the drive pulses before finally being detected on single-photon superconducting nanowire detectors (SNSPDs). (b) Interferometer visibility. We detune the filter locking point from the device resonance such that we are only sensitive to pump photons that leak through the filters. Here we plot the rate of pump photons detected with detector 1 (orange) and detector 2 (green) as a function of phase difference of the interferometer arms. We observe the expected 2π periodicity with an interference visibility of 98.4%. The difference in amplitude stems from different degrees of suppression of pump photons through the two filter lines.

devices. Similarly, we measure that less than 2% of the detected photons during the blue pulses are leak photons.

The asymmetry in pump suppression has additional consequences for the experiments in which we drive the devices simultaneously. The total rate of leak photons varies with the selected phase setting ϕ_r. The angular dependency is proportional to the sum of the two curves in inset (b) of Figure 5.4. These unwanted photons result in additional coincidences in the second order interference of the main experiment, hence they distort the visibility sweeps of Figure 5.2. The purely sinusoidal fits are not capturing this accurately and therefore mostly serve as a guide to the eye. The values of the correlation coefficients $E(\phi_b, \phi_r)$ in Table 5.1 are affected in the same way. We measure at angles $\phi_r = 0.087\pi$ and 0.587π, of which the latter suffers more from the imperfectly filtered drive pulses. This is the main reason of why we observe a reduction in the Bell parameter S compared to the expected results from the visibility V in Figure 5.2 alone. Dark counts on the other hand are low enough (around 15 Hz) to only contribute by less than 1% to the detection events.

5.5.3. DEVICE FABRICATION AND CHARACTERIZATION

The optomechanical devices are fabricated from silicon-on-insulator wafers with a device film thickness of 250 nm as described in [52]. In order to reliably find identical devices on distinct chips, we optimized the electron-beam doses throughout the lithog-

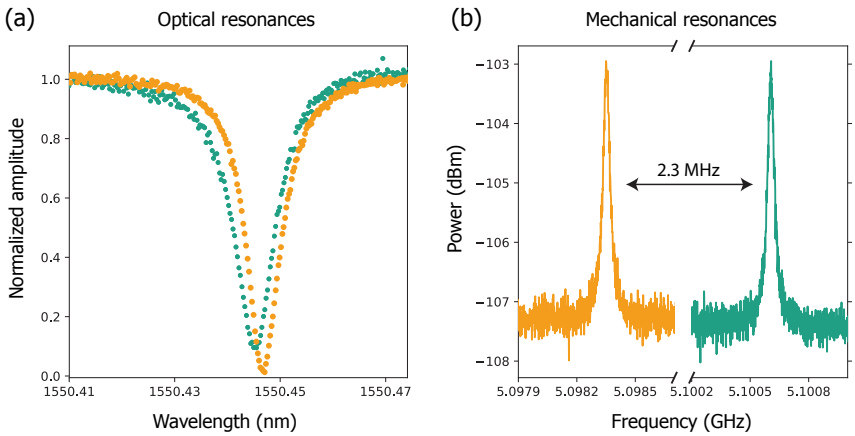

Figure 5.5: Spectroscopy of optomechanical devices A (green) and B (orange). Left: Optical cavity reflection spectrum of the cavities. Right: Mechanical resonances of the two devices.

raphy step, which allowed us to obtain a distribution of only 1 nm of the optical resonances. To further reduce the variability between different chips, we first fabricate a single large chip, fully process it, and then cleave it into smaller pieces as a last step. This optimized procedure results in two chips with excellent overlap of the optical resonances. Unlike in previous experiments [114], our fabrication method allowed us to perform the experiments without the need for serrodyne shifting of the photon frequencies in one of the arms of the interferometer but rather only apply a small linear ramp signal to the red and blue pulses using the EOM in arm A.

We characterize the optical resonances by sweeping a continuous-wave part of our laser and recording the reflected intensity resonances (cf. Figure 5.5(a)). As we use reflectors at the end of our waveguides (see Figure 5.1), we effectively couple in a single sided way to our devices and therefore expect to see resonances as dips in the reflected light. The measurements of the mechanical resonances are performed by locking the laser to the blue sideband of the optical resonances, amplifying the reflected light in a fiber amplifier and then detecting the optomechanically generated sideband on a fast photodiode (Figure 5.5(b)).

To evaluate the absorption heating dynamics, we perform a pump-probe experiment with the individual devices. Here we excite the devices with a blue and probe with a red drive pulse after a variable delay $\Delta\tau$, see Figure 5.6. The pulse energies are chosen similarly to the ones in the main text. As already observed in previous work [52, 57, 114], the devices see absorption caused heating with a rise time of several hundreds of nanoseconds. The highest temperature is reached in both cases at a delay of around 1 μs, after which the devices decay with their intrinsic quality factors. We fit the excitation dynamics $d_i(\Delta\tau)$ of the two devices (i = A, B) with a phenomenologically motivated double exponential model of the form $d_i(\Delta\tau) = a_i e^{-\Delta\tau/\tau_i} - b_i e^{-\Delta\tau/\eta_i} + n_{\mathrm{init},i}$ [114]. We can extract the energy lifetimes of our devices as $\tau_A = 3.3 \pm 0.5$ μs and $\tau_B = 3.6 \pm 0.7$ μs. Note that the final decay level $n_{\mathrm{init},i}$ does not represent the true base temperature, as we still observe counts from the intra-pulse heating. Nevertheless, we can bound the occupancy $n_{\mathrm{init},i}$

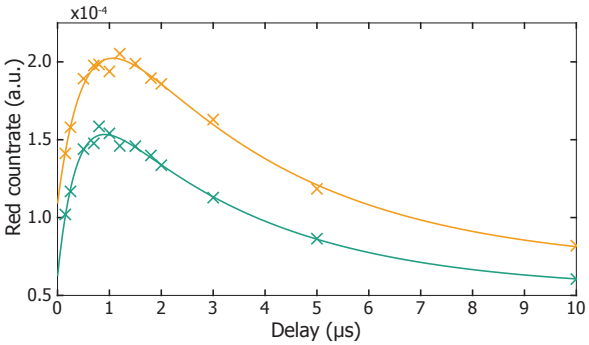

Figure 5.6: Absorption heating and mechanical decay. Heating dynamics of device A (green) and device B (orange) from a pump-probe experiment are plotted. We excite the devices with a blue pulse and read out the mechanical state after a variable delay $\Delta\tau$. Thermal phonons due to absorption of the blue drive occupy the mode on a timescale of several hundreds of nanoseconds, after which the excitations decay to the cold environment with the mechanical lifetimes.

from above using the asymmetry in the click rates of blue and red sideband scattered photons $C_{\mathrm{b},i}$ and $C_{\mathrm{r},i}$ as $n_{\mathrm{init},i} = C_{\mathrm{r},i}/(C_{\mathrm{b},i} - C_{\mathrm{r},i})$ [57]. We perform the measurements for blue and red pulses individually with a duty cycle of 50 μs each. For device A, we determine the initial occupation to be ~0.07 phonons if measured on detector 1 and ~0.09 phonons if measured on detector 2. Device B has similar apparent occupations of ~0.06 phonons on detector 1 and ~0.09 phonons if measured on detector 2. The difference in the measurements on the two detectors reflects the different amount of leak suppression as discussed above. However, both measurements also contain the intrapulse heating detection events, meaning we expect the real occupancy in the dark to be below these extracted numbers.

5.5.4. STATISTICAL ANALYSIS

The statistical analysis for the CHSH inequality is done using the same techniques as Ref. [114]. We apply binominal statistics on the number of coincidence events n_{ij} in Equation (5.4) and generate discrete probability distributions. We then treat the correlation coefficients E as non-trivial functions of two random variables ($n_{\mathrm{same}} = n_{11} + n_{22}$ and $n_{\mathrm{diff}} = n_{12} + n_{21}$) and numerically find their probability distributions via the cummulative density function method. We calculate the probability distribution for the Bell parameter S as a convolution of the probability distributions of the four correlation coefficients. Finally we calculate the expectation value and error bounds ($\pm 34\%$ confidence interval) by numerical integration of the resulting probability density function.

The data for the main experiment was acquired in with approx. 500−620 million trials per CHSH setting. Together with the duty time of 50 μs, this amounts to pure measurement times of 7.0 − 8.6 hours per setting, or ~31 hours in total. This time is excluding additional overhead that is needed to re-lock the filters or manage the acquired data. The total actual measurement time is about a factor of two larger. The data was taken in intervals of 20 minutes and the CHSH settings were cycled after each interval. During

CHSH setting	Trials	Heralding clicks	n_{00}	n_{01}	n_{10}	n_{11}
(1,1)	597302527	645858	708	194	175	611
(1,2)	500363903	546488	606	162	164	521
(2,1)	622224596	680260	752	212	185	589
(2,2)	540137661	592728	170	586	590	198

Table 5.2: Recorded coincidence clicks of the main experiment. Individual trials are performed every 50 μs. Heralding clicks are the detected photons scattered by the blue pulse. Coincidences $n_{i,j}$ are clicks that were registered after getting a heralding event in the same trial, with i, j indicating the detector for the blue and red scattered photons.

the experiment, a total of 6423 photon pairs were detected, which amounts to roughly 210 successful trials per pure measurement hour.

6

A QUANTUM MEMORY AT TELECOM WAVELENGTHS

Andreas WALLUCKS, Igor MARINKOVIĆ, Bas HENSEN, Robert STOCKILL, Simon GRÖBLACHER

Nanofabricated mechanical resonators are gaining significant momentum among potential quantum technologies due to their unique design freedom and independence from naturally occurring resonances. With their functionality being widely detached from material choice, they constitute ideal tools to be used as transducers, i.e. intermediaries between different quantum systems, and as memory elements in conjunction with quantum communication and computing devices. Their capability to host ultra-long lived phonon modes is particularity attractive for non-classical information storage, both for future quantum technologies as well as for fundamental tests of physics. Here we demonstrate a DLCZ-type mechanical quantum memory with an energy decay time of $T_1 \approx 2$ ms, which is controlled through an optical interface engineered to natively operate at telecom wavelengths. We further investigate the coherence of the memory, equivalent to the dephasing T_2^* for qubits, which exhibits a power dependent value between 15 and 112 µs. This demonstration is enabled by a novel optical scheme to create a superposition state of $|0\rangle + |1\rangle$ mechanical excitations, with an arbitrary ratio between the vacuum and single phonon components.

This work is submitted to peer review as *A quantum memory at telecom wavelengths.* A. Wallucks, I. Marinković, B. Hensen, R. Stockill and S. Gröblacher

6.1. INTRODUCTION

Quantum memories are a core quantum technology, which are at the very heart of building quantum repeaters enabling large quantum networks [3, 127]. Significant progress on realizing such memories has been made with ions [128, 129], atomic ensembles [130–132], single atoms [133], NV centers [134], and erbium-doped fibers [69]. The important characteristics of a memory, besides sufficiently long storage times, are the ability to store a true quantum state, such as a single photon, high read-out efficiency, on-demand retrieval and operation at low-loss telecommunication wavelengths around 1550 nm. So far, none of the realizations have simultaneously been able to demonstrate all of these requirements. In particular, native operation of memories in the telecom band has been limited to classical states [135, 136] or storage times in the tens of nanoseconds [137].

Recently, chip-based nanoscale mechanical resonators have emerged as promising components for future quantum technologies. Their functionality is principally based on geometry, allowing for great flexibility in materials and designs and creating unique opportunities for combining them with many other techniques such as integrated photonics and superconducting circuitry [19, 138]. Over the past few years, experiments have demonstrated an ever increasing control over quantum states of mechanical resonators both via optical as well as electrical interfaces. Experimental breakthroughs with radio-frequency drives include electromechanically induced entanglement [72, 115], phonon-number detection [139, 140] and single [16] as well as multi-phonon Fock state generation [18]. Optical control over the modes on the other hand has enabled the detection of non-classical optomechanical correlations [57, 141, 142], single phonon Fock state creation [52, 58], mechanical entanglement [75, 114], as well as an optomechanical Bell-test [51]. Excitingly, many of these chip-based devices have also been shown to host ultra long-lived mechanical modes with down to wavelength-scale footprints and low cross-talk [7, 9, 143]. Combined, these results demonstrate the key ingredients for the realization of a quantum optomechanical memory, potentially paving the way towards on-chip, integrated quantum transducers and repeaters, operating at telecom wavelengths [23, 28].

In this work, we demonstrate for the first time non-classical correlations from an engineered high-Q mechanical resonance and an optical interface in the conventional telecom band over the full decay time of the mechanical mode. To achieve this, the mechanical quantum memory is prepared in a single-phonon state, directly usable for a DLCZ-type quantum repeater scheme [10]. We show that we can store this state for approx. 2 ms without degradation due to induced thermal occupation of the mode, a limitation of several previous experiments [51, 52, 114]. We study the phase fluctuations of the mechanical mode in a classical continuous interference measurement and then by a pulsed dephasing experiment in the quantum regime. For the latter, we develop and experimentally demonstrate a scheme to herald superpositions of the first mechanical Fock state and the vacuum. This stored state is then optically retrieved and interfered with a weak coherent probe to measure the coherence of the mechanical mode.

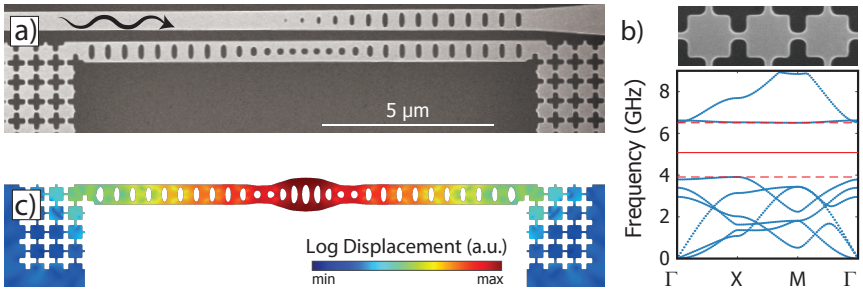

Figure 6.1: (a) Scanning electron microscope image of the optomechanical device. Light enters from the left through the coupling waveguide in the top part of the image. In the device below, an optical and a mechanical resonance are coupled through radiation pressure effects. The structure is fabricated from a 250 nm thick silicon layer and is undercut to produce free-standing devices. (b) Zoom in to the phononic shield region (top) and corresponding bandstructure simulation (bottom). Unlike the nanobeam itself, the shielding region exhibits a full bandgap of the phononic crystal around the resonance frequency Ω_m (solid red line). (c) Finite element simulation of the isolation through the phononic shield. Also shown is the mechanical mode of interest at 5.12 GHz in the center of the nanobeam.

6.2. METHODS

Our device design, shown in Figure 6.1, is based on previous experiments with silicon optomechanical crystals [7, 52, 57], which were optimized for low Q_m to speed up rethermalization with the cryogenic environment. In contrast, in our present work the mechanical mode serves as a phononic memory for optical states and we are hence looking for large quality factors. In particular, the mechanical decay time sets a bound on the distance over which light can travel while the stored state has not decayed yet. For a 1 ms decay time, for example, we can reach distances of around 200 km. The mechanical mode of the silicon nanobeam is confined within a phononic crystal mirror region which does not exhibit a complete bandgap. Fabrication imperfections typically couple the phonon mode of interest to leaky modes with different symmetries, such that the quality factor is limited by radiation loss. For this experiment, we surround the device with a two-dimensional phononic shield which features a complete bandgap [7] and can increase the decay time up to several seconds [9]. Figure 6.1a shows the fabricated device with the additional phononic shielding region on the sides and an optical waveguide on top used to probe the device. A simulation of the bandstructure of the shield region in Figure 6.1b shows a wide bandgap emerging between 4 GHz and 6 GHz.

The actual device used in this experiment has a mechanical resonance at $\Omega_m/2\pi = 5.12$ GHz with a measured decay time of the mode of $2\pi/\Gamma_m = 1.8$ ms (see Supplementary Information), corresponding to a quality factor of $Q_m \approx 10^7$ at mK temperatures. While we have fabricated structures with significantly better quality $Q_m \gtrsim 10^9$, this particular choice is a compromise between long memory time and a low re-initialization rate, which would in turn necessitate a prohibitively long measurement time. The optical resonance of the device is at $\omega_c/2\pi = 191.4$ THz, corresponding to a wavelength in the telecom band at 1566.4 nm, with an intrinsic optical linewidth of $\kappa_i/2\pi = 460$ MHz. As shown in Figure 6.1a, we couple to this resonance via an adjacent optical waveguide with a coupling rate of $\kappa_e/2\pi = 1840$ MHz. The optical and mechanical mode interact

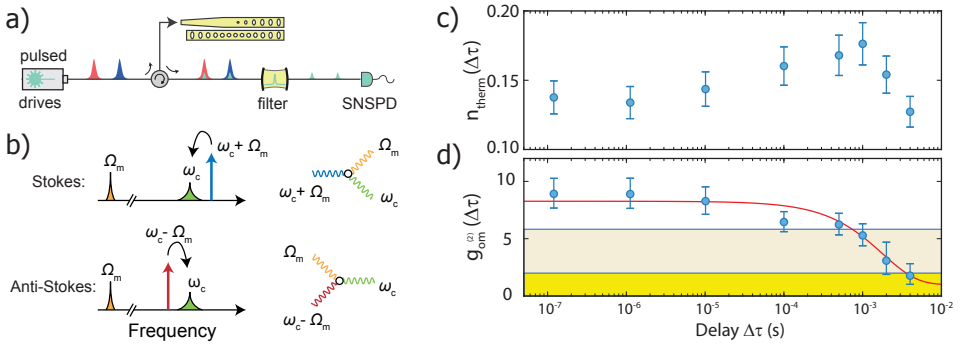

Figure 6.2: (a) Laser pulses are sent to the optomechanical device through an optical circulator. These pump pulses are subsequently filtered, allowing us to measure their Stokes- and anti Stokes-fields in superconducting nanowire single photon detectors (SNSPD).(b) Scattering scheme for the Stokes (top) and anti-Stokes (bottom) processes. Here Ω_m denotes the mechanical and ω_c the cavity frequencies. (c) Calibrated thermal mode occupancy, showing a delayed rise in the absorption heating from a blue-detuned pulse with energy 3 fJ and probed by a red-detuned pulse with energy of 280 fJ. The occupation contains a background of ~0.1 phonons added by the red drive during the readout. (d) We verify the suitability of our optomechanical device as a quantum memory by measuring the decay time of the cross-correlations between the Stokes- and anti Stokes-fields $g^{(2)}_{om}$ (see text for details). We find clear non-classical photon-phonon correlations up to $T_1 = 1.8 \pm 0.2$ ms. The classical bound, above which the single phonon that is stored in the mechanical mode still retains its quantum character is highlighted by the yellow-shaded region, while the beige region depicts the threshold for violating a Bell-type inequality. The red curve is the theoretically predicted decay, for which we use the thermal occupation measured in (c). All error bars are s.d.

with a single photon coupling rate $g_0/2\pi = 780$ kHz.

A sketch of the fiber-based optical setup is shown in Figure 6.2a, where the device is placed in a dilution refrigerator with a base temperature of 15 mK. We generate 40 ns long optical pulses with blue sideband detuning from the optical resonance $\omega_b = \omega_c + \Omega_m$, as well as red sideband detuning $\omega_r = \omega_c - \Omega_m$. Using linearized optomechanical interactions [55, 56], blue driving enables the optomechancial pair generation $\hat{H}_b = -\hbar g_0 \sqrt{n_b}\hat{a}^\dagger \hat{b}^\dagger + \text{h.c.}$, with n_b the intracavity photon number, $\hbar$ the reduced Planck constant and $\hat{a}^\dagger$ ($\hat{b}^\dagger$) the optical (mechanical) creation operator. Red detuning on the other hand enables a state-transfer between the optics and the mechanics, due to the beamsplitter-type interaction $\hat{H}_r = -\hbar g_0 \sqrt{n_r}\hat{a}^\dagger \hat{b} + \text{h.c.}$, where n_r is the intra-cavity photon number for the red pulses. After interacting with the device in the cryostat, the light passes an optical filter with 40 MHz bandwith which is locked to the optical resonance ω_c and the Stokes- / anti-Stokes fields are detected on a superconducting nanowire single photon detector (SNPSD).

6.3. RESULTS

As a first step, we perform a thermometry measurement to validate that the 5-GHz mode of the device is thermalized to its motional groundstate at the base temperature of the cryostat. This is performed by sending trains of either blue or red sideband detuned pulses to the device, such that an asymmetry in the scattering rates between the blue and the red drives allows us to infer the mechanical mode occupation [57, 144]. The mea-

sured mode temperature is elevated from the bath temperature due to heating caused by power-dependent optical absorption of the drives. We can thus use this measurement to determine our maximally attainable driving power for a given mechanical mode occupation. We limit the instantaneous heating caused by a single pulse to ~0.1 phonons, which we attain with a pulse energy of 280 fJ. This corresponds to a state-transfer probability of $p_r = 14\%$ between phonons and photons in the anti-Stokes field by the red detuned drive using the interaction of $\hat{H}_r$. The total detection efficiency of the scattered photons is 13%, as discussed in the SI, including contributions from the collection efficiency into the device waveguide, fiber coupling and losses in the filter setup.

To test the performance of the device as a quantum memory, we proceed to use a two-pulse protocol with a blue-detuned excitation followed by the red-detuned readout pulse. The first pulse enables the optomechanical pair generation according to $\hat{H}_b$, producing entanglement between the optical Stokes-field and the mechanical mode of the form

$$|\psi\rangle_{om} \propto |00\rangle_{om} + \sqrt{p_b}|11\rangle_{om} + \mathcal{O}(p_b), \tag{6.1}$$

where o (m) indicate the optical (mechanical) modes and p_b is the excitation probability. Due to the correlations in this state, detecting a Stokes photon after the blue pulse heralds the mechanical mode in a state close to a single phonon Fock state [52]

$$|\Psi\rangle_m \propto |1\rangle_m + \mathcal{O}(\sqrt{p_b}). \tag{6.2}$$

Crucially, the excitation probability p_b has to be kept small to avoid higher order excitation terms. Additionally, residual absorption heating causes an increased thermal background of the mechanical mode at delays far longer than the pulse length. We choose an energy of the blue-detuned pulse of 3 fJ, which corresponds to a scattering probability of $p_b = 0.2\%$. This optical power is chosen to limit the peak of the absorption heating to below 0.2 phonons occupancy at most. In Figure 6.2c, we show the calibrated mode occupation, highlighting an increase in phonon occupancy for delays of up to 1 ms before the device re-thermalizes.

With this limited thermal background, we are able to study the quantum nature of the optomechanically prepared state of Eq. (6.2). We do this using the cross-correlation $g^{(2)}_{om} = P(B \wedge R)/[P(B)P(R)]$, for which $P(B)$ ($P(R)$) is the probability to detect a Stokes (anti-Stokes) photon and $P(B \wedge R)$ is the joint probability to detect a Stokes and an anti-Stokes photon in one trial. We probe the ability of the mechanical mode to store non-classical correlations by evaluating $g^{(2)}_{om}(\Delta\tau)$ for pulse delays $\Delta\tau$ over the energy decay time of the mechanical resonance. Generally, we expect the cross-correlation to evolve like $g^{(2)}_{om}(\Delta\tau) = 1 + \exp(-\Gamma_m \Delta\tau/2)/n_{therm}(\Delta\tau)$ [114], where Γ_m is the inverse of the decay time and $n_{therm}(\Delta\tau)$ the number of thermal phonons in the mode. We note that this cross correlation has a classical bound given by a Cauchy-Schwarz inequality of $g^{(2)}_{om} \leq 2$ [57, 58]. An even stronger bound can be motivated by considering the threshold required to violate a Bell inequality for the entanglement present in the system (c.f. Eq. (6.1)), which is given by $g^{(2)}_{om} \geq 5.7$ [51, 121]. In Figure 6.2d, we show the measured cross-correlations together with the theoretically expected correlation (solid line) that we calculate using the measured thermal occupation. We find that the classical threshold (yellow shaded region) is violated by the Stokes and anti-Stokes fields for $T_1 = 1.8 \pm 0.2$ ms. Furthermore

the Bell-threshold (beige shaded region) is violated for ~500 μs, supporting the prospect of using mechanical quantum memories in a device independent setting [111].

The above measurements clearly demonstrate that, although absorption heating is still present in the device, we can limit its effects to be able to store and retrieve quantum states in the mechanical mode for its whole decay time. Since the scheme uses a phase-symmetrical state of the form of Eq. (6.2), we are, however, not sensitive to frequency fluctuations of the mechanical mode. We therefore proceed to test the ability of our device to preserve non-trivial quantum mechanical states.

We begin by assessing the frequency stability of the mechanical mode in the classical regime. As discussed in the SI, direct measurements of the mechanical sidebands on a fast photodector using a relatively strong continuous sideband drive show a broadened mechanical linewidth of several kHz. A frequency jitter of the mechanical mode is visible using fast scanning [9]. In order to determine the extent to which optical driving influences these dynamics, we require a measurement scheme that employs a minimum possible intracavity power. We devise an interferometric scheme based on coincidence detection in continuous wave driving, shown in Figure 6.3a. We probe the device with a single optical tone on either the red or the blue sideband, such that the reflected light contains an optomechanically generated sideband. This sideband is interfered with a probe field at roughly ω_c, which we create in-line from the reflected optical drives using an electro-optic amplitude modulator (EOM). To be able to detect photons using the SNSPDs, we remove the background with a 40-MHz bandwidth filter. The main idea of the measurement is that the mixing of the mechanically and electro-optically generated sidebands causes intensity modulations at their beat frequency, which can be observed in the coincidence rate $C^{(2)}(\Delta\tau)$ of the detected photons. The interference can explicitly be demonstrated by detuning the EOM drive by $\delta\Omega/2\pi = 100$ kHz from the mechanical frequency Ω_m, such that $C^{(2)}(\Delta\tau)$ shows oscillations of $2\pi/\delta\Omega = 10$ μs period (see Figure 6.3b). With the mechanical mode in a thermal state, we can measure the decay of this interference to extract a classical coherence time τ_{class} by fitting an exponentially decaying sine function to the data (solid line). Additional details on the data evaluation as well as measurements of the thermal bunching of the optomechnical photons are discussed in the SI.

Figure 6.3c shows the dependence of the coherence time τ_{class} for a sweep of the intracavity photon number n_c. Measurements for blue detuning (blue points) and red detuning (red points) split for increasing photon numbers due to optomechanical damping (see discussion in the SI). Inconsistent with residual optomechanical effects, however, is the decrease of the decay constant τ_{class} for the lowest photon numbers. A linear extrapolation to $n_c = 0$ results in $\tau_{class,min} = 16 \pm 3$ μs. The behavior for $n_c > 1$ can be explained by a saturation of the decay constant for high photon numbers. We fit the power dependence to a phenomenological model (solid line) that we discuss in the SI. From the model we obtain a saturation value of $\tau_{class,max} = 112 \pm 27$ μs.

The power dependence observed for the classical coherence decay τ_{class} invites an investigation of the coherence time in the quantum regime, where, additionally, the mode evolves in the dark. In contrast to the above pulsing scheme (c.f. Figure 6.2), we are now required to measure the phase stability of non-symmetric mechanical quantum states. A natural candidate are superpositions between the vacuum and single phonon

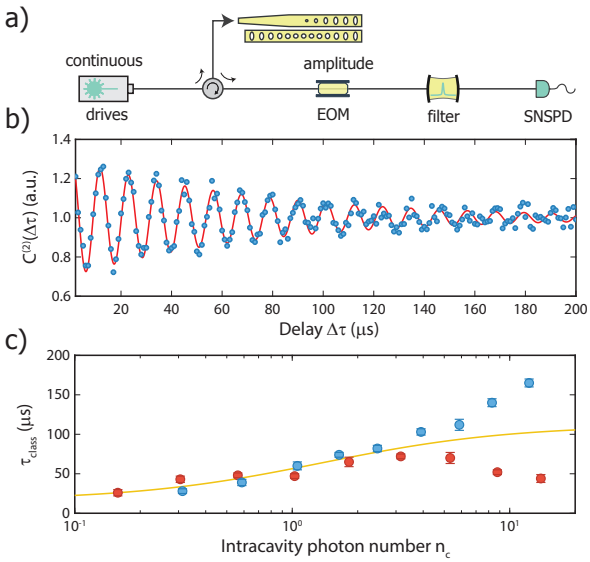

Figure 6.3: (a) Schematics of the setup for measuring the mechanical phase coherence with a CW laserby mixing Stokes and anti-Stokes fields from the device with an electro-optically generated tone. Under continuous driving the mechanical mode is highly excited and the measurement is therefore fully in the classical regime. The amplitude electro-optic modulator (EOM) is driven at a detuning of $\delta\Omega/2\pi = 100$ kHz from the mechanical frequency Ω_m. (b) Interference between the optomechancially and the electro-optically generated sidebands causes an oscillatory signature in the two-fold coincidence rate $C^{(2)}(\Delta\tau)$. Shown is an exemplary measured trace for ~3 intra-cavity photons (dots) and a fit to the data (solid curve) for a sinusoidal oscillation with exponentially decaying amplitude. The raw data and details on the post-processing can be found in the SI. (c) The extracted decay times τ_{class} as a function of intracavity photon numbers n_c for blue detuning (blue points) as well as for red detuning (red points). An increase in the measured coherence time, as a function of intracavity photon number, can clearly be seen (fit to the data as solid curve). For $n_c \gtrsim 2$ optomechanical effects become visible.

mechanical states of the form

$$|\Psi\rangle_m = \sqrt{1-n}\cdot|0\rangle_m + \sqrt{n}\cdot e^{i\phi}|1\rangle_m. \tag{6.3}$$

Here ϕ is an experimentally chosen phase during the state preparation and $\sqrt{n}$ the amplitude of the single phonon component, with $n = 1/2$ indicating a 50:50 superposition state. Once the mechanical mode is prepared in such a state, it can be read out after a variable delay $\Delta\tau$ and the anti-Stokes field can be interfered with a weak coherent state (WCS), for example. The visibility of this interference can then be used to assess the coherence time T_2^* over which the mechanical mode is able to preserve the phase of the superposition state. The scheme we describe below is conceptually similar to earlier experiments in quantum optics [145, 146] and enables the optical preparation of a massive mechanical superposition state for the first time.

We adapt the setup for the correlation decay measurements, adding an optical interferometer in the detection path (c.f. Figure 6.4a). The light is split by a 99:01 fiber coupler and enters a Mach-Zehnder interferometer with a high transmission upper arm and a low transmission lower arm. In the low transmission arm of the interferometer, an

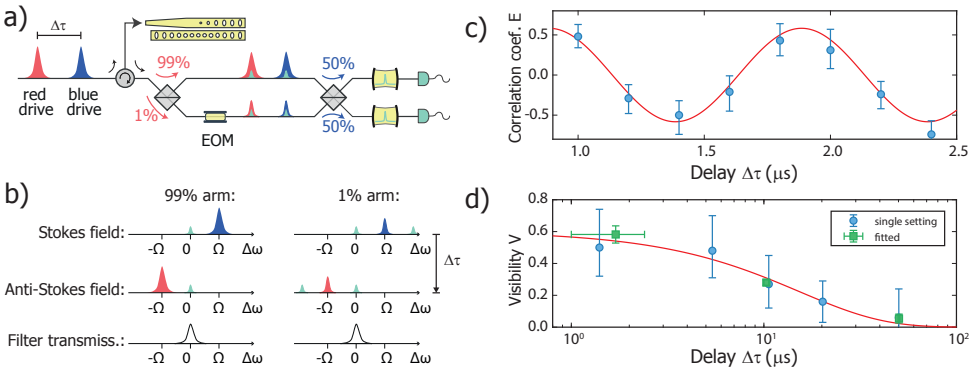

Figure 6.4: (a) Sketch of the experimental setup for the coherence measurement of the quantum memory. After being reflected from the device, the optical pulses are sent to an imbalanced Mach-Zehnder interferometer. In the lower, highly attenuated arm, an electro-optic modulator (EOM) creates a weak coherent state at the cavity frequency ω_c by sideband modulation of the reflected drives. The WCS is then interfered with the optomechanical Stokes field from the upper, weakly attenuated interferometer arm. All "which-path" information is erased, such that a detection event on either of the detectors (SNSPDs) heralds a superposition state of the form shown in Eq. (6.3). The state is retrieved from the device using a red-detuned drive and the interference of the anti-Stokes field with a second WCS generated with the same EOM is measured. (b) Schematic depicting the frequency components in the interferometer by their detuning $\Delta\omega$ from the optical resonance. The high transmission arm contains the optical drives as well as the Stokes or anti-Stokes fields. In the low-transmission arm, the sidebands generated by the EOM dominate over the optomechanically scattered photons. After filtering, only the light on resonance with the optical cavity is detected in the SNSPDs. (c) Interference of the anti-Stokes field with a WCS after a delay from the blue pulse of $\Delta\tau \approx 1\ \mu$s. The phase evolution over the delay is enabled by detuning the EOM drive by $\delta\omega/2\pi = 1$ MHz. A sinusoidal fit to the data (solid curve) yields a visibility $V = 58 \pm 5\%$. (d) Decay plot of the interference visibility. Blue are single delay measurements on the maxima and minima of the curve, whereas green data points are extracted from fits similar to (c). The solid curve is a fit to an exponential decay.

EOM modulates the reflected blue drive to produce a sideband at ω_c (more than 20 dB bigger than the optomechanical one in this arm). This weak coherent state is then interfered with the optomechanically generated sideband in the upper arm of the interferometer on a balanced fiber coupler. Both of its outputs pass 40 MHz bandwidth filter setups to remove unwanted frequencies to only detect fields at ω_c. A click on one of the SNSPDs heralds the superposition state of Eq. (6.3) of the mechanical mode, as the Stokes sideband is made indistinguishable from the electro-optically generated weak coherent state. In a quantum picture, the second beamsplitter removes all "which-path" information of the detected photons.

The detection is performed after a variable delay by interfering the anti-Stokes fields from the device with another weak coherent state, generated from the red drive with the EOM in the lower arm. The quantum interference of the two can be detected through oscillations of the correlation coefficient $E = \left(g^{(2)}_{\mathrm{om,sym}} - g^{(2)}_{\mathrm{om,asy}}\right) / \left(g^{(2)}_{\mathrm{om,sym}} + g^{(2)}_{\mathrm{om,asy}}\right)$ of the cross-correlations $g^{(2)}_{\mathrm{om,sym}}$ for detection events in the same and $g^{(2)}_{\mathrm{om,asy}}$ for different detectors. While we have to ensure phase stability of the Stokes and anti-Stokes fields and the respective weak coherent states, we only have to stabilize the Mach-Zehnder interferometer, since path-length fluctuations from the device to the first fiber coupler

are canceled due the fields propagating in common mode. Similar to the classical coherence measurement, the requirement to actively change the interferometer phase to detect the interference can be alleviated by slightly detuning the EOM drive frequency from Ω_m. We chose a relative detuning of $\delta\omega/2\pi = 1$ MHz, which is again much smaller than the bandwidth of the optical pulses of ~25 MHz but enables a full 2π phase sweep of E for delays of 1 μs.

The amplitude n of the superposition state can be chosen experimentally by adjusting the ratio of optomechanically to electro-optically generated photons in the sidebands. Without a thermal background on the mechanical mode, it is possible to prepare states of the form of Eq. (6.3) with a given single phonon amplitude n by matching the count rate due to the WCS C_{WCS} to the Stokes count rate C_b according to $C_{WCS}/C_b = (1-n)/n$. In our measurements the amplitude of the WCS is set to optimize for maximum visibility and detection rates at the same time, which allows us to perform the mechanical coherence measurements as quickly as possible. In the SI, we provide further numerical studies how the choice of amplitude affects the expected interference visibility in the presence of a thermal background on the mechanical mode. Experimentally, we choose the same pulse energies for the red and the blue drives as in the correlation measurement (c.f. Figure 6.2). We adjust the EOM drive power such that $C_{WCS}/C_b \approx 7$, which, for a thermal background of $n_{therm} = 0.1$, results in a single Fock amplitude $n = 0.56$. The second weak coherent state is matched in power to the anti-Stokes field. Figure 6.4c shows our experimentally measured correlation coefficient E. A clear oscillation in the signal with the expected period of $2\pi/\delta\omega = 1$ μs can be seen for small delays $\Delta\tau$ around 1 μs, demonstrating the successful interference of the superposition state in the anti-Stokes field with the WCS. We obtain a visibility of $V = 58 \pm 5\%$ by fitting the signal between 1 μs and 2 μs with a sinusoidal function. This visibility exceeds the classical threshold of $V_{class} = 50\%$ for the second order interference visibility of two coherent states and is in good agreement with the theoretically expected value of 63% (see SI).

We plot the decay of the interference visibility for extended delays in Figure 6.4d. The quantum coherence time of the state that we obtain from fitting an exponential decay is $T_2^* = 15 \pm 2$ μs. This decay happens much faster than the measured T_1 for the symmetrical state. The obtained value is in very good agreement with the classical coherence time $\tau_{class,min} = 16 \pm 3$ μs, considering the intracavity photon number averaged over the duty cycle in the pulsed experiment is $n_{pulse,avg} \approx 10^{-8}$ (c.f. Figure 6.3c). As shown before, the power dependence of the coherence time is not consistent with optomechanical effects. The observed saturation at $\tau_{class,max}$ indicates dispersive coupling of the mode to defect states such as two-level fluctuators in the host material, which are a source of noise and dissipation in amorphous materials [147]. The surface of silicon is known to host a variety of states that have been found to affect the performance of quantum devices [148] and mechanical modes [9, 12]. Optical driving of our particular device causes a saturation of the frequency jitter imposed on the mechanical mode. A more detailed study of the dynamics and prospects on an improved τ_q will be the focus of future work. Similar two-level fluctuator noise is already known for a wide variety of systems, for which saturation driving of the states by different experimental means could offer a way to reduce the induced noise on the mode of interest [149, 150].

In conclusion, we have measured the quantum decay T_1 and the coherence time T_2^*

of a high-Q mechanical system and demonstrated its suitability as a mechanical quantum memory. This was possible by employing a two-dimensional phononic shield for mechanical isolation, small absorption heating in the optomechanical device compared to previous experiments and by devising a novel way to create and characterize mechanical superposition states. We design our device to operate directly in the low-loss telecommunication band, with several orders of magnitude larger quantum memory coherence times than competing systems [137] while allowing an on-demand read-out. The memory is prepared in both a superposition and a single phonon state, which will allow it to be directly used in a DLCZ-type quantum network architecture. Combined with recent progress in coupling phonons to superconducting circuitry [22, 23], this approach will also allow to realize versatile hybrid architectures for quantum storage and transduction. We would like to note that, with improvements in the efficiencies, writing an arbitrary input state into the memory is in principle possible [151]. Our measurements show a clear power dependence of the coherence time, which is indicative of two-level systems on the surface of our structure. Future experiments will determine the nature and detailed properties of these surface states, which should lead the way to significant improvements of the coherence time of our devices.

We would like to thank Moritz Forsch, Beverly Li, Michail Vlassov, and Ian Yang for experimental support and Daniel Bothner for valuable discussions. We also gratefully acknowledge assistance from the Kavli Nanolab Delft. This work is further supported by the Foundation for Fundamental Research on Matter (FOM) Projectruimte grants (15PR3210, 16PR1054), the European Research Council (ERC StG Strong-Q, 676842), and by the Netherlands Organization for Scientific Research (NWO/OCW), as part of the Frontiers of Nanoscience program, as well as through a Vidi grant (680-47-541/994). B.H. and R.S. acknowledge funding from the European Union under a Marie Skłodowska-Curie COFUND fellowship.

6.4. SUPPLEMENTARY INFORMATION

6.4.1. SETUP FOR PULSED EXPERIMENTS

A sketch of the fiber-based setup used in the main text is shown in Figure 6.5. The pulsed optical drives are generated from two tunable diode lasers, which are stabilized using a wavelength meter. Both light sources are filtered with fiber filters of 50 MHz bandwidth to reduce the amount of classical laser noise at GHz frequencies. The 40 ns Gaussian shaped pulses used in the experiment are created by two 110 MHz accousto-optic modulators (AOMs 1 and 2), which, after the lines are combined, are additionally gated by AOM3 for a better pulse on-off ratio. All AOMs can be operated in CW mode to allow for device characterization and the CW coherence measurement. An electro-optical modulator (EOM2) is used to test the longterm stability of the setup (see text below). The light is routed into the dilution refrigerator and to the device via an optical circulator, whereas coupling to the device waveguide is achieved with a lensed fiber tip.

For the coherence measurements, we use an imbalanced Mach-Zehnder interferometer with a 99:01 and a 50:50 fiber coupler. The free spectral range of the interferometer is measured to be 5.4 GHz. The high transmission arm only contains an optical switch, whereas the low transmission arm contains EOM2 and a fiber stretcher to lock the interferometer phase. The fiber stretcher is home built and, including the feedback electronics, we achieve a locking bandwidth of 10 kHz. The light used for the locking is injected into the open port of the 99:01 fiber coupler. It is derived from a third laser, which is locked ~10 GHz away from the blue drive to operate at the maximum suppression point of the detection filters (see below). We use continuous light for locking the interferometer and blank it for 1 μs around the measurement pulses with AOM4. The amplitude modulator used for the continuous coherence measurement (c.f. Figure 6.3 of the main text) is shown in the dotted box in the upper interferometer arm.

The detection part of the setup consists of two lines with two filter setups each to suppress the reflected drives from the devices and two SNSPDs. The filter setups are free-space, with two ~40 MHz linear cavities each. The free spectral range of these home built cavities is designed to be between 17 GHz and 19 GHz in each line. The measurements are paused every 4 s and continuous light is injected to the filter lines via optical switches (not shown, see also [57]) such that the filters can be stabilized on resonance with the optical cavity. This re-locking step generally consumes about 10-15% of the measurement time, whereas the filter transmission stays within ~90% during the time the filters are allowed to drift freely.

The darkcounts in our filter lines are roughly 20 Hz on detector 1 and 25 Hz on detector 2. Our measurements contain additional background due to leakage of the sideband drives though the the filter setup. The suppression of the filter sets at 5 GHz is ~84 dB for filter set 1 and ~89 dB for set 2. We further measure our detection efficiency by using an off-resonant weak pulse from the device [52]. We achieve overall efficiencies of the filter setups and the SNSPDs of approximately 34% for setup 1 and 32% for setup 2 including the efficiencies of the respective detectors. The collection efficiency of the optomechanically generated sidebands consists of the device to waveguide coupling $\kappa_e/\kappa \approx 80\%$ as given in the main text and fiber coupling efficiency of 56%. The measurement also suffers additional loss of 30% from the fiber optic components in the detection lines (i.e. the circulator and Mach-Zehnder interferometer). The total detection efficiency dur-

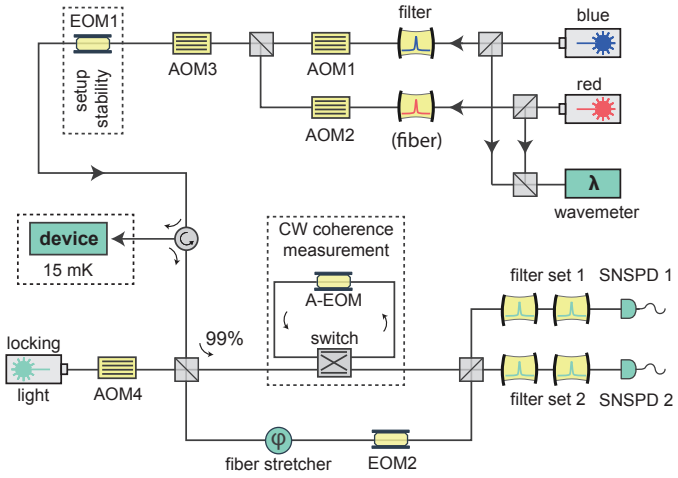

Figure 6.5: Schematic of the setup used in the experiment featuring all active elements, including acousto-optic modulators (AOM), electro-optic modulators (EOM) and one amplitude modulator (A-EOM). Elements for polarization alignment are not shown. The setup is based on low loss SMF-28 optical fibers, with the only exception being the filter setups in the detection path, which consist of two linear, optical free-space cavities each, for improved insertion losses compared to commercial fiber based components. The superconducting nanowire single photon detectors (SNSPDs) are placed at the 800 mK stage in the same cryostat as the device.

ing the experiments in Figure 6.4 of the main text is thus ~10%. In the non-classicality measurements of Figure 6.2, we do not use the interferometer but directly connect the circulator output to filter set 1. The loss of the fiber components in this case is reduced to 10% which results in a total detection efficiency for Stokes or anti-Stokes photons of $\eta_{\text{det}} \approx 13\%$.

6.4.2. DEVICE CHARACTERIZATION

We perform initial measurements of the mechanical linewidth in the cryostat with a continuous blue sideband drive and detection of the optomechanical sideband on a fast photodiode such that it can be evaluated on a real-time spectrum analyzer. We find the center frequency at Ω with a visible jitter when scanning for around 50 ms as shown in Figure 6.6b. We proceed to generate a histogram in Figure 6.6a by taking the frequency differences between each two successive measurements. The fit (solid line) to a Gaussian lineshape yields a broadened FWHM linewidth of about 1.6 kHz. As can be seen from the plot, we additionally observe slower drifts of the center frequency in the single digit kHz range, which can reduce the inferred coherence time during long measurement runs. For the pulsed coherence experiment of Figure 6.4d, the center frequency was monitored during the measurement for the delay of $\Delta\tau = 50\,\mu$s. While this drift does in principle limit the coherence of the device, it was found to be small enough not to have a significant influence on our data.

While the devices are well thermalized to the cryostat, optical absorption of the pulses causes the mechanical mode to couple to an additional hot phonon bath [9, 57, 76], thus limiting the maximal optomechanical interaction strengths without significant heating.

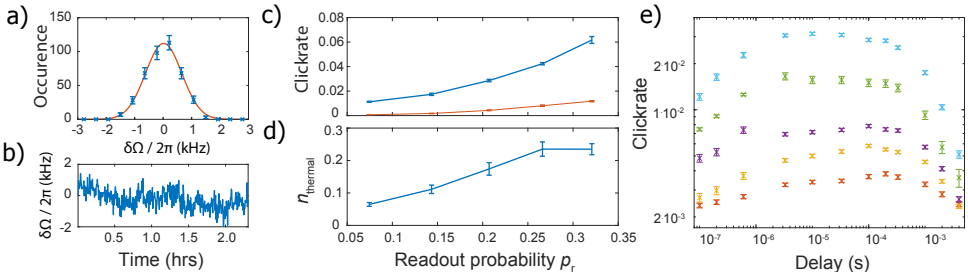

Figure 6.6: (a) Direct measurements of the mechanical line show a jitter $\delta\Omega$ around the center mechanical frequency (bottom), that results in a Gaussian lineshape of FWHM ~1.6 kHz when evaluating relative frequency differences between subsequent measurements. (b) Slow drifts of the frequency in the single digit kHz range over the course of hours can furthermore be seen. These drifts were not compensated for in the main measurements. (c) Measurements of the power dependence of the mechanical occupation. We plot the bare clickrates C_b (blue) and C_r (red) of blue- and red-detuned pulses. (d) Thermal occupation $n_{thermal}$ inferred as $n_{thermal} = C_r/(C_b - C_r)$. At low powers, the thermal occupation rises roughly linearly with the power due to an increase in optical absorption. The zero power offset is mainly determined by dark counts on the detectors and leakage of the optical drives through the filter set. The apparent saturation of the thermal occupation at higher optical powers is due to the onset of assisted scattering in the blue pulses. The asymmetry measurement method is not valid in this regime anymore. (e) Pump-probe experiment for different pulse energies showing the power-dependent rise of the mechanical mode temperature due to optical absorption and the rethermalization of the device to the cryogenic environment. The pulse energies from top to bottom are 280 fJ (cyan), 140 fJ (green), 56 fJ (purple), 28 fJ (yellow), 7 fJ (red).

We determine the increased mode temperature from absorption using a sideband asymmetry measurement. The optomechanical scattering probabilities $p_b \propto 1+n_{thermal}$ (blue) and $p_r \propto n_{thermal}$ (red) attain different values close to the groundstate of the mechanical mode for which the thermal occupation $n_{thermal}$ reduces to zero. This enables a self calibrated thermometry of the mechanical mode, as shown in Figure 6.6c for different optical powers. We limit the total induced phonon occupation to less than 0.2 phonons in order to be able to overcome the Bell non-classicality threshold in Figure 6.2. Using $g^{(2)}_{om} \approx 1 + 1/(p_b + n_{therm})$ [52], this is feasible up to occupations of $n_{therm} = (\sqrt{2}-1)/2 \approx 0.207$. In particular, we limit the Stokes scattering probability such that an additional 0.1 phonons due to absorption are added at most. The corresponding pulse energy is determined by sending a weak blue pulse 10 μs before the thermometry pulses, resulting in a Stokes scattering probability of $p_b = 0.2\%$. In a similar fashion, we also limit the readout rates by allowing for only 0.1 phonons to be added due to absorption, which is possible for state-transfer probabilities up to 14% (see Figure 6.6d). Together with the optical detection efficiency of $\eta_{det} \approx 13\%$ (see above), we thus obtain a total probability of converting and detecting the mechanical Fock states of 2%.

We proceed to measure the mechanical quality factor using a pulsed pump-probe experiment [52] with two red-detuned pulses of 40 ns length each. While the device is assumed to be thermalized upon arrival of the first pulse such that the optomechanical interaction is largely suppressed, absorption of the optical drive in the material causes a rise in the occupancy of the 5 GHz mechanical mode. The heating dynamics can then be studied using the second equally strong pulse to read out the temperature of the mode at

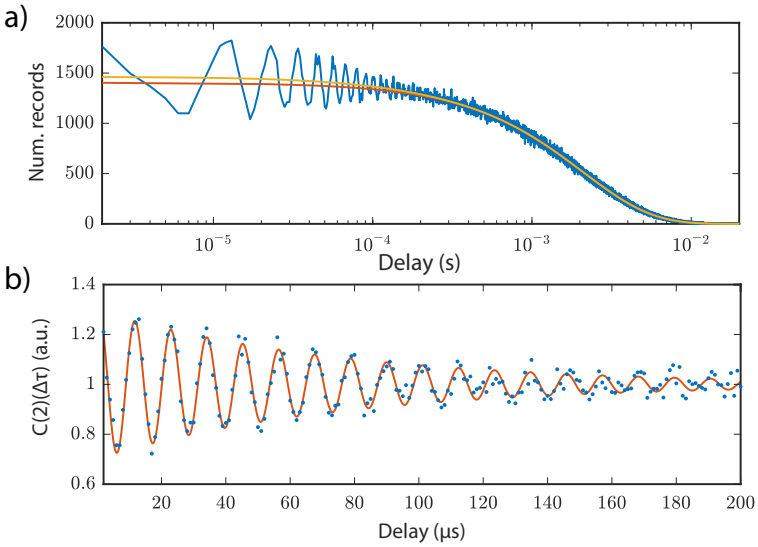

Figure 6.7: (a) Example of the CW coherence measurement. Beating of an electro-optically generated and the mechanical sideband can be seen in the statistics of the time difference between successive detection events. We process the raw data by taking an exponentially decaying background due to the finite count rate in the experiment (solid red line) into account, as well as an exponential count rate decay due to thermal bunching of the optomechanically scattered photons (solid yellow line). (b) Processed data showing the two-fold coincidence rate $C^{(2)}(\Delta\tau)$ after background correction, in which we fit an exponentially decaying sinusoidal function (solid line) to extract the time-constant of the dephasing.

6

a variable delay (c.f. Figure 6.6d). Unlike Figure 6.2c of the main text, this data is not calibrated in terms of phonon numbers of the mechanical mode. At relatively high optical powers, the absorption causes delayed heating effects which reaches a maximum occupation around several μs before the device re-thermalizes to the bath. Surprisingly, the dynamics of the delayed mode occupancy changes as well. For low powers, where the initial temperature rise around ~1 μs is reduced, a slower dynamic becomes apparent such that the temperature starts to peak around a few hundreds of μs. The mechanical decay on the other hand seems largely unaffected by this new feature.

6.4.3. CONTINUOUS WAVE COHERENCE MEASUREMENT

DATA EVALUATION

For the data evaluation of Figure 6.3b of the main text, we take ~ 4 million clicks for each measurement, save the timestamp for each click, then take the time difference between successive events and compute a histogram. The raw data is shown in Figure 6.7a, from which we extract the phase decay shown in Figure 6.7b in two steps (which is the same data as in Figure 6.3b). Most prominently, the number of detection events in Figure 6.7a decays to zero for delays much bigger than 1 ms. This decay occurs with a time-constant of roughly one over the count rate of the experiment. We experimentally set the count rate to be ~500 Hz for each of the driving powers by attenuating in the detection path

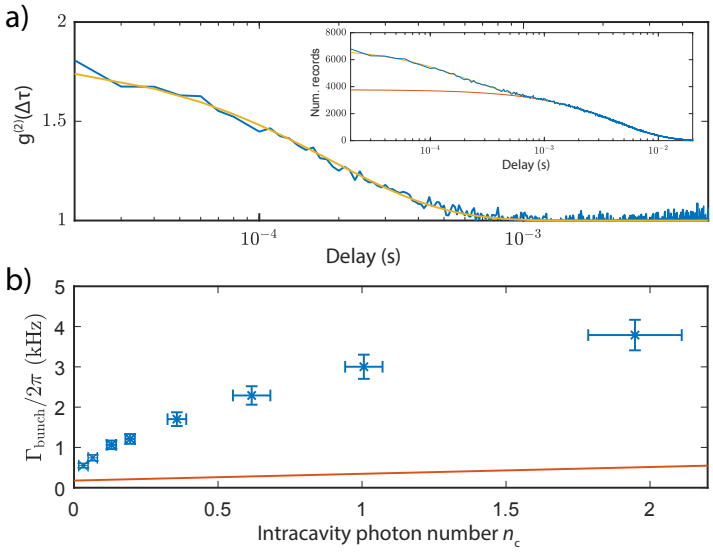

Figure 6.8: (a) Bunching data from the device measured in the anti-Stokes photons without EOM modulation. The raw data (inset) is processed in the same way as for the continuous coherence measurement. The fit (solid line) is an exponential decay to extract the decay timescale $2/\Gamma_{\mathrm{bunch}}$ of the bunching. (b) The measured Γ_{bunch} for a sweep of the intracavity power. The solid line is a theoretical power dependence based on optomechanical damping with a zero power offset of Γ_{m}.

if necessary. This is a tradeoff allowing us to detect on the relevant timescales of the mechanical mode while enabling a good signal to noise ratio by surpassing the optical background. We assume Poissonian statistics for the delayed clicks, such that we can account for the decay by fitting an exponential function to the data (orange line in Figure 6.7a).

A second decay of the count rate can be seen in the data (yellow line in Figure 6.7a). This is due to bunching of the optomechanically scattered photons since the device is in a thermal state. While rather small in the displayed trace, it can be fairly pronounced for higher driving powers (see also below). We account for this by fitting a second, faster exponential to the data. Accounting for both of these effects, we get the normalized two-fold coincidence rate $C^{(2)}(\Delta\tau)$ for delays $\Delta\tau$ which is shown in Figure 6.7b. We fit an exponentially decaying sine function to the processed data (solid line), from which we can confirm the expected period of the oscillation as well as extract the time-constant of the visibility decay. Deviations from the exponential decay of the visibility yield information on the decay time of the proposed two-level fluctuators as the physical mechanism of the decay. We find that the simple exponential fit captures the decay well for all measured powers.

We further fit the increase of the visibility decay τ_{class} in Figure 6.3c of the main text using a phenomenologically motivated model. We find a good agreement to a linear dependence at the lowest powers with the zero power offset $\tau_{\mathrm{class,min}}$. This dependence is only visible up to $n_{\mathrm{c}} \approx 1$, where the increase in coherence time slows down. We use a

model function for the decay constant $\tau(n_c)$ that is consistent with two-level fluctuators as the physical origin of the power dependence. We assume that coupling to fluctuating defects in the dark causes frequency fluctuations of the mechanical mode resulting in $\tau_{\text{class,min}}$. With the optical drives present, these frequency fluctuations take on a different, much smaller magnitude, resulting in $\tau_{\text{class,max}}$. Optical driving can transition between these two regimes, which we will refer to as states for simplicity. With the drive present, the transition occurs proportional to the relative population in the states, such that the rate is $g_{\text{def}} n_c \left(\tau_{\text{class,max}} - \tau\right)$, where g_{def} is an unknown optical defect coupling and n_c is the intracavity photon number. In the absence of the optical drive, we assume that the system exponentially decays towards the state corresponding to the the zero power decay constant. The relaxation rate is thus $-\Gamma_{\text{def}}\tau$ with the unknown defect decay constant Γ_{def}. Overall, we have

$$\dot{\tau} = g_{\text{def}} n_c \left(\tau_{\text{class,max}} - \tau\right) - \Gamma_{\text{def}}\tau, \tag{6.4}$$

which has a steady-state solution of

$$\tau(n_c) = \tau_{\text{class,min}} + \frac{\tau_{\text{class,max}} - \tau_{\text{class,min}}}{1 + \frac{\Gamma_{\text{def}}}{g_{\text{def}}} \frac{1}{n_c}}. \tag{6.5}$$

We apply this function to the background in Figure 6.3c in the main text, extracting estimates for $\tau_{\text{class,min}}$ and $\tau_{\text{class,max}}$ with $\frac{\Gamma_{\text{def}}}{g_{\text{def}}}$ being the final free fit parameter. We note that optomechanical effects are expected to cause a symmetric deviation from this background for blue and red detuned measurements (linearly with n_c). This optomechanical damping effect is seen in the data points deviating from the solid line in Figure 6.3c for $n_c > 1$. It can further be studied in a second similar experiment described in the following.

We use the scheme to observe photon bunching due to the thermal mechanical state, assuming that the two-fold count rate $C^{(2)}(\Delta\tau)$ is proportional to the second order coherence function $g^{(2)}(\Delta\tau)$. To this end we perform an experiment in which we do not mix the sidebands with an electro-optically generated probe, but rather detect scattered light from the device only using a red sideband drive. We show an example measurement in Figure 6.8a for an intracavity photon number of $n_c \approx 0.75$. The theoretically expected value of $g^{(2)}(0) = 2$ is reduced, which can easily be explained by dark counts in our detection as well as residual leakage of the sideband drive though the filter setup. Both of these have flat statistics over the shown range of delays. An exponential fit to the data lets us infer the time constant $2/\Gamma_{\text{bunch}}$ of the decay.

Its inverse relates to the mechanical linewidth and as such is expected to be subject to optomechanical damping Γ_{opt}. Since we are driving on the red sideband, we expect the damping to cause a linear increase according to $\Gamma_{\text{bunch,theory}} = \Gamma_m + \Gamma_{\text{opt}}$ with $\Gamma_{\text{opt}} = 4 n_c g_0^2/\kappa$ and an intrinsic zero power value Γ_m. In Figure 6.8b, we plot the measured values (crosses) together the expected effect (solid line) based on the device parameters and the damping rate Γ_m from the pulsed measurements (c.f. Figure 6.6). While a linear extrapolation of the datapoints to zero power does approach the expected value of Γ_m, the broadening of the line is much bigger than optomechanical effects can explain. We suspect that absorption heating of the continuous driving of the device causes

an increased temperature of the device which results in a broadening of the line [12]. As we do not have a simple model for this effect we abstain from taking it into account in the data in Figure 6.3c of the main text. We note that due to its presence, we expect the high power maximum coherence time $\tau_{\text{class,max}}$ inferred from the model to be a lower bound on the real value. We also note, however, that the effect cannot be responsible the low power drop towards $\tau_{\text{class,min}}$ in Figure 6.3c. With the measurement in Figure 6.8 we show that the magnitude of the effect is too low at small intracavity powers to affect the coherence measurement and that in any case, it could only cause an increase in coherence time with lower optical power rather than a decrease.

6.4.4. PULSED COHERENCE MEASUREMENT

PREDICTED VISIBILITY

We perform numerical studies using QuTiP [59, 60] to predict the interference visibility of the mechanical superposition states including a thermal background on the mechanical mode. We start from a thermal state of the mechanical mode with given initial occupation n_{init} and the optical vacuum state. For this simulation, we lump all thermal occupation of the mode as seen in the experiment into this single term, regardless whether it is present from the beginning or induced by the blue or the red pulse. The two-mode squeezed state is generated by applying the optomechanical pair generation Hamiltonian $\hat{H}_{\text{b}} = -\sqrt{p_{\text{b}}}\hat{a}^\dagger\hat{b}^\dagger + \text{h.c.}$, with $\hat{a}^\dagger$ ($\hat{b}^\dagger$) being the optical (mechanical) creation operator and the experimentally chosen scattering probability $p_{\text{b}} = 0.2\%$. We then define a WCS mode with creation operator $\hat{c}^\dagger$, which we prepare in a coherent state with variable amplitude $\alpha < 1$ and phase $\theta = 0$, representing the experimental interferometer phase. We then use a beamsplitter matrix $\hat{H}_{\text{BS}} = i/\pi\,\hat{a}^\dagger\hat{c} + \text{h.c.}$ to mix the two modes with equal splitting ratio. After this operation, our density matrix describes the modes of the beamsplitter output as well as the mechanical mode. Heralding is modeled by applying a projection matrix onto the Fock-state to one of the optical modes. Afterwards we trace out both of the optical modes, such that the remaining density matrix describes the mechanical mode in the superposition state. At this stage of the calculation we have prepared the state of Equation 6.3 of the main text including a thermal background.

To emulate the detection of the state, we define a second WCS mode with operator $\hat{d}^\dagger$ and coherent amplitude $\beta < 1$ and phase ϕ. We skip the optomechanical readout step and treat the mode $\hat{b}^\dagger$ as the anti-Stokes field. We apply another beamsplitter operation $\hat{H}_{\text{BS}} = i/\pi\hat{b}^\dagger\hat{d} + \text{h.c.}$ to model the interference of the anti-Stokes field and the WCS and finally calculate the expectation value for the number of excitations in the output. Sweeping the WCS phase ϕ, we find the intensity to fluctuate periodically between the two modes, from which we can infer the expected visibility of the interference.

The results of these calculations are shown in Figure 6.9. We find the analytically expected result that, without any thermal occupation, an equal match of the excitations in the optomechancially generated state and the first weak coherent state results in an equal superposition $|\psi\rangle = 1/\sqrt{2}(|0\rangle_{\text{m}} + e^{i\phi}|1\rangle_{\text{m}})$. We can further see that the numerical calculation predicts that only a state without any thermal background can have perfect interference visibility with a coherent state, and it can do so only in the limit of vanishing amplitude. We calculate a maximum visibility for a 50:50 superposition state without thermal background of $V = 1/\sqrt{2}$, which reproduces the analytical solution. Fur-

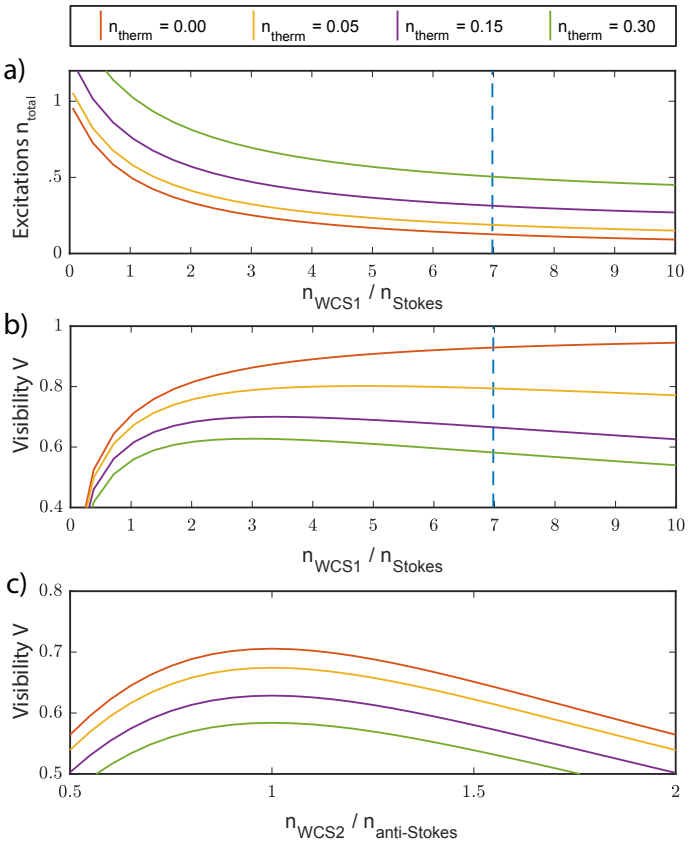

Figure 6.9: Numerical calculations on the pulsed coherence measurement of the main text. The color coding for different numbers of thermal excitations n_{therm} on top of the figure applies to all plots. (a) Numerical calculations of the expected number of excitations n_{total} in the superposition state of Eq. (6.3) of the main text. This number includes both the single phonon part for the superposition as well as the thermal background contribution. The horizontal axis indicates the ratio of excitations in the Stokes field n_{Stokes} and the weak coherent state n_{WCS1} with which it is overlapped for the state preparation. Experimentally, this ratio can be chosen by the respective count rates on the detectors, regardless of detection efficiency. The vertical dashed line indicates the experimental setting used in the main text. (b) Expected interference visibility V for the superposition states of (a) with a second weak coherent state of equal amplitude to the anti-Stokes field. Here we assume optimal settings in the readout step. (c) Decrease of the expected visibility of the interference from mismatching the number of excitations n_{WCS2} of the second weak coherent state from the anti-Stokes field $n_{\text{anti-Stokes}}$. The calculations here assume parameters for the state preparation corresponding to the vertical dashed line in (b).

thermore we see that for an increasing thermal background, the maximally attainable visibility is reduced and the optimal superposition ratio is shifted slightly to states with a stronger single phonon component. The drop-off in the expected visibility with an increase in the WCS amplitude is only gradual. In the experiment, we therefore choose to exceed the amplitude of the Stokes field with the amplitude of the weak coherent state by a factor of ~7 (dashed vertical line in Figures 6.9a and b). This allows us to increase

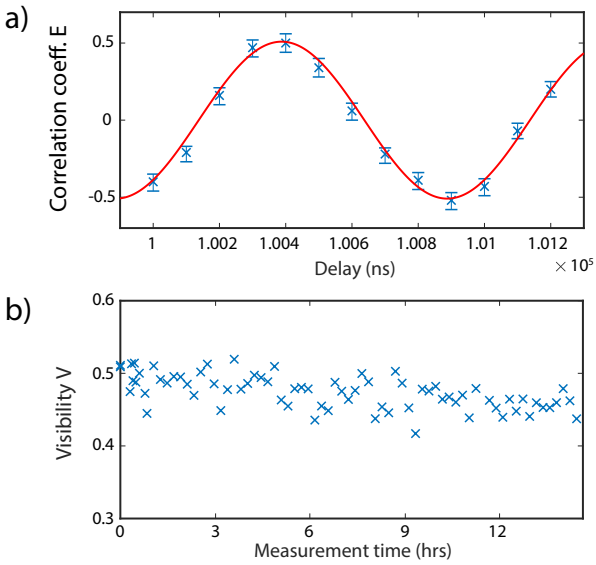

Figure 6.10: (a) Setup visibility calibration. The lasers are detuned from the optical resonance of the device and we use EOM1 (c.f. Figure 6.6) to modulate sidebands on the pulsed optical drives. The rest of the experiment is performed like the pulsed coherence measurement of the main text. The second order interference we expect from two weak coherent states, generated with EOM1 and EOM2, is bounded to 50%. Fitting the correlation coefficient E just as in the main text, we achieve visibilities in good agreement to this value for all relevant delays (shown is an example for a delay of ~100 μs). (b) Longterm stability of the interference visibility in (a). Drifts of our setup, in particular polarization variations, slowly reduce the achievable visibility in the setup. In the main experiment, the polarizations and optical powers were manually readjusted about every 24 hrs.

our measurement rate while only slightly compromising on the achievable visibility. In Figure 6.9c we see, that such a big mismatch is not possible for the amplitude β of the second weak coherent state used in the detection. Here, we need to match the anti-Stokes field from the device.

SETUP STABILITY

We test the stability of our setup during the long integration times in the coherence measurement by emulating the optomechanical device with the EOM1 right before the circulator in Figure 6.6. The lasers are detuned by 1 nm from the device, such that they do not interact with the optical mode of the device but are still efficiently reflected in the coupling waveguide. To emulate the optomechanical scattering from the device we drive EOM1 at the mechanical frequency to create weak sidebands at ω_c. We otherwise recreate the pulsed coherence measurement of the main text by creating weak coherent states with EOM2 from the reflected drives and measuring the interference in the coincidence counts. Since all detected fields are in electro-optically generated coherent states, the expected visibility in this case is 50%.

This measurement allows us verify the maximally attainable visibility of our setup (see Figure 6.10a). We measure a visibility of about 50%, regardless of the actual delay of red and blue pulses, which we test up to 1 ms. We can further test the longterm stability

of the setup on the timescale of hours. Figure 6.10b shows the evolution of the fitted visibility for a delay around 100 μs between the two pulses over more than 12 hrs. We see a slow decrease of the system visibility, with a reduction to ~45%. The reason for this effect is most likely due to polarization drifts in the setup which are not compensated for. During the actual measurement, the polarizations are readjusted every ~24 hrs. We assign a maximally achievable visibility of 95% to our setup, based on these slow drifts. The expected visibility for the interference given in the main text includes this correction.

7

CONCLUSION

The work presented in this thesis is an exploration of optomechanical nanobeams as DLCZ quantum memories. The resonators are operated close to the mechanical ground-state by cryogenic cooling in a dilution refrigerator. It was shown the blue-detuned drive produces light-matter entanglement which can be used to herald non-classical mechanical states. They can be stored and retrieved using the red-detuned interaction and the quantum nature of the mechanical state can be confirmed through measurements on the anti-Stokes photons (chapter 3). It was furthermore shown in chapter 4 that, using the DLCZ protocol, entanglement between two separate devices can be heralded by mixing their Stokes fields on beamsplitters and registering optomechanically scattered photons on single photon detectors. It was also shown in chapter 5 that the entanglement present in the combined system of Stokes fields and mechanical modes of two devices can be large enough to violate a Bell inequality. The experiments of these chapters were performed with storage times of the mechanical states of several hundreds of nanoseconds at most. It was shown in chapter 6 that employing phononic shielding around the nanobeam resonators, long-lived mechanical resonances can be fabricated which can store phononic Fock states for longer than one millisecond. Using a protocol to herald mechanical superposition states, the phase coherence of the mode was investigated. It was found that excess phase noise currently limits the storage of these states to 15 μs.

While the principal suitability of the structures for distributing long-distance entanglement could be shown during this work, future improvements need to be achieved to make them practical. Most importantly, the fabrication techniques will have to be further developed to reduce the negative effect of the surface. Improvements in surface quality and a reduction of native oxide growth after the fabrication will reduce the absorption heating in the devices. With this, active laser cooling [152] of the devices deep into their groundstate could drastically reduce the required measurement times. Rapid re-thermalization at millikelvin bath temperatures could, however, also be achieved by controlled coupling to other lossy phonon modes such the device could be actively Q-switched [153]. Alternative approaches to reaching better device performance are to

change the design to 2D [154, 155] or 3D structures [143, 156] which show lower absorption heating due to a reduced surface exposure as well as a better thermalization, albeit currently at a reduced coupling. Mechanical coherence times might also be improved in such devices [157]. Alternatively, different materials might be found which could outperform silicon [158, 159]. Beyond this, multi-mode quantum optomechanics in the quantum coherent regime would enable advanced protocols improving on standard DLCZ [160, 161]. Coupling of multiple modes could either be achieved optically [162, 163], in dielectric gradient fields [164], piezo-electrically [165] or by actively coupling degenerate modes [85]. Finally, coupling to both optical fields as well as superconducting circuits would enable fundamentally new protocols and operations on the devices. A coherent conversion of quantum states from the microwave domain [24] or the probabilistic entanglement of superconducting qubits over optical links [166, 167] are two of the main goals in this direction. In such hybrid systems, mechanical modes could thus be used for both transduction and storage of quantum information.

Quantum memories natively operating at telecommunication wavelengths are sparse, as relatively few natural resonances are available (see appendix A). Mechanical devices such as the optomechanical nanobeams discussed in this thesis could circumvent this by relying on purely engineered optical resonances which can be designed freely throughout the telecom band in a variety of host materials. Their flexibility and incorporation options with other technologies make them fit well to the toolbox of integrated quantum photonics. The big task to make them practical is to overcome the drawbacks of engineered solid-state systems, such as fluctuating environments as well as losses and noise due to imperfect fabrication techniques.

A

OPTICAL MEMORIES FOR QUANTUM REPEATERS

One of the current frontiers of quantum physics is to distribute quantum information beyond individual laboratories. Long-distance quantum links could provide a supporting structure to interconnect quantum computers[3, 4], including novel protocols for blind quantum computing [168] or private database queries [169] among others. In a future in which such quantum computers have compromised current cryptography standards, new types on quantum communication technologies could also enable communication channels secured by the laws of physics [2, 170]. In a scientific context, schemes have been proposed for improved global timekeeping [171] or astronomy [172, 173]. Generating entangled states with separation of the particles on a global scale would also enable new types of experiments on post-quantum theories, investigating abnormal decoherence processes and quantum gravity [174].

The experiments in this thesis are based on the DLCZ scheme [10]. It was among the first practical quantum repeater schemes requiring only linear optical elements, such as phase shifters and beamsplitters, and single photon counters. The quantum memories at the heart of the protocol were initially proposed to be clouds of cold atoms. The key aspect to make DLCZ a practical quantum repeater scheme is that the memory does not consist of a single emitter which is strongly coupled to an optical mode. It rather made use of collective excitations in dense optical media, which drastically relaxes experimental requirements compared to earlier schemes. The structure in this case is an atomic three level lambda system with two metastable lower states $|g_1\rangle$ and $|g_2\rangle$ which can be coupled by a Raman transition via an excited state $|e\rangle$ as shown in Figure A.1. All atoms are initially in $|g_1\rangle$, such that a weak off-resonant drive on the $|g_1\rangle - |e\rangle$ transition causes spontaneous emission on the $|e\rangle - |g_2\rangle$ transition. A detection of a photon in the Stokes field carries no information on which of the atoms went though the transition, such that the cloud is projected on a coherent superposition of all those possibilities. The driving fields have to be weak to avoid the multiple transitions from occurring. The collective excitation of the atomic cloud can be read out efficiently by resonantly driving

the $|g_2\rangle - |e\rangle$ transition. The distribution of entanglement between multiple clouds of atoms, i.e. the quantum memories, is done analogously to chapter 1.3. Joint measurements on the Stokes fields of simultaneously driven clouds can be used to project their states onto approximately maximally entangled states. These Bell-state measurements are performed, as in chapter 1.2.2, by mixing the fields on a beamsplitter and selecting on trials with a click in one of the detectors of the output arms. An analogous measurement on the anti-Stokes fields after readout can be used to swap entanglement between more clouds.

The DLCZ paper has spurred a lot of experimental efforts with implementations close to the original proposal (e.g. Ref. [63]). The scheme has, however, also successfully been translated to several other systems which are now sometimes referred to as DLCZ memories or read-only memories. Their common feature is that they can be excited under off-resonant driving from an optical transition, such that their state becomes entangled to an optical signal mode. Together with single photon detection in this signal mode, this allows to initialize them in highly non-classical states without the need for an outside quantum light source. Successful demonstrations have been achieved in atomic clouds [63, 175–178], warm atomic vapors [61, 62] and defects in solid state systems [68, 69, 179]. Mechanical modes have been considered as well, with experimental demonstrations of DLCZ entanglement [75] and phonon Fock states [58, 180] in room temperature terahertz diamond modes.

While the protocol has reduced the experimental requirements on the memory elements, it still comes with its own difficulties. One main problematic is that it does require longterm sub-wavelength phase stabilization between all the nodes of the repeater. This is a general problem with so-called single excitation protocols, where the quantum information is encoded in the number of excitations in the system. A straightforward improvement is to encode into a second degree of freedom, for example polarization [181]. A coincidence detection with two photons of orthogonal polarization is then required for a successful Bell-state measurement, which reduces the entanglement generation rate. On the upside, the phase stability requirements are relaxed several orders of magnitude to the order of the photon coherence length. Proposals for a scheme in which both the entanglement creation and swapping require two-photon coincidences were given in Ref. [182, 183] and experimental work followed in Ref. [184]. A review about further subtleties with DLCZ and its variations is given is Ref. [11].

A more general class of quantum memories, read and write memories, allow for a mapping of an optical state from an outside source and controlled re-emission later. Successful demonstrations have been carried out for example with single atoms [65, 185], clouds of atoms [151, 186], NV centers [187], ions [66, 67, 188], quantum dots [189] or rare-earth doped crystals [179]. Such absorptive memories have a greater flexibility in applications as the read-only memories, yet often require more experimental overhead hindering scalability. While not the focus of this manuscript, we note that the optomechanical interactions allow for a similar operation using the optomechanically induced transparency [13] with a recent experiment demonstrating quantum operation at short delays [14]. Regardless of the protocol, operation in the telecom band around 1550 nm

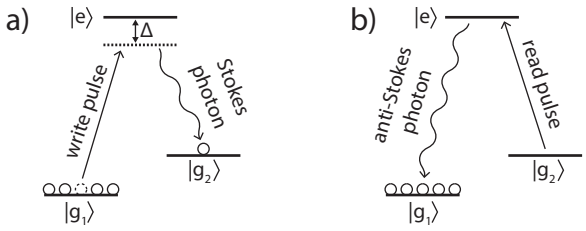

Figure A.1: Schematic of the processes used in the DLCZ scheme. a) Write process based on spontaneous Raman scattering under off-resonant driving of the $|g_1\rangle - |e\rangle$ transition. b) Highly efficient readout of the memory state by resonantly driving on the $|g_2\rangle - |e\rangle$ transition.

wavelength is strictly required for any realistic fiber-based approach for long-distance quantum communication. All of the above implementations require an additional frequency conversion step. This is a potential source of loss, noise and substantial experimental overhead. We note though, that recently demonstrations have exceeded conversion efficiencies of 50% [190]. Another way to avoid this problem is to use an asymmetric quantum light source, as for example implemented in solid-state detect centers [191]. The most promising candidates for native telecom quantum memories are erbium ions, doped into a variety of host materials [69]. Optical coherence times up to 4 ms [192] have been measured which could in the future be complemented spin coherence up to seconds [193]. Demonstrations of optical storage, however, have been limited to classical input states [135, 136] or relatively short storage times [137].

REFERENCES

[1] P. Kok, W. J. Munro, K. Nemoto, T. C. Ralph, J. P. Dowling, and G. J. Milburn, *Linear optical quantum computing with photonic qubits,* Reviews of Modern Physics **79**, 135 (2007).

[2] N. Gisin, G. Ribordy, W. Tittel, and H. Zbinden, *Quantum cryptography,* Reviews of Modern Physics **74**, 145 (2002).

[3] H. J. Kimble, *The quantum internet,* Nature **453**, 1023 (2008).

[4] S. Wehner, D. Elkouss, and R. Hanson, *Quantum internet: A vision for the road ahead,* Science **362**, 6412 (2018).

[5] A. I. Lvovsky, B. C. Sanders, and W. Tittel, *Optical quantum memory,* Nature Photonics **3**, 706 (2009).

[6] M. Aspelmeyer, T. J. Kippenberg, and F. Marquardt, *Cavity optomechanics,* Rev. Mod. Phys. **86**, 1391 (2014).

[7] J. Chan, *Laser cooling of an optomechanical crystal resonator to its quantum ground state of motion,* Ph.D. thesis, California Institute of Technology (2012).

[8] S. M. Meenehan, *Cavity Optomechanics at Millikelvin Temperatures,* Ph.D. thesis, California Institute of Technology (2015).

[9] G. S. MacCabe, H. Ren, J. Luo, J. D. Cohen, H. Zhou, A. Sipahigil, M. Mirhosseini, and O. Painter, *Phononic bandgap nano-acoustic cavity with ultralong phonon lifetime,* arXiv:1901.04129 (2019).

[10] L. M. Duan, M. D. Lukin, J. I. Cirac, and P. Zoller, *Long-distance quantum communication with atomic ensembles and linear optics.* Nature **414**, 413 (2001).

[11] N. Sangouard, C. Simon, H. de Riedmatten, and N. Gisin, *Quantum repeaters based on atomic ensembles and linear optics,* Reviews of Modern Physics **83**, 33 (2011).

[12] S. M. Meenehan, J. D. Cohen, S. Gröblacher, J. T. Hill, A. H. Safavi-Naeini, M. Aspelmeyer, and O. Painter, *Silicon optomechanical crystal resonator at millikelvin temperatures,* Phys. Rev. A **90**, 011803 (2014).

[13] S. Weis, R. Rivière, S. Deléglise, E. Gavartin, O. Arcizet, A. Schliesser, and T. J. Kippenberg, *Optomechanically Induced Transparency,* Science **330**, 1520 (2010).

[14] D. G. England, K. A. Fisher, J.-P. W. MacLean, P. J. Bustard, R. Lausten, K. J. Resch, and B. J. Sussman, *Storage and retrieval of THz-bandwidth single photons using a room-temperature diamond quantum memory,* Physical Review Letters **114**, 053602 (2015).

[15] J. W. Silverstone, D. Bonneau, J. L. O'Brien, and M. G. Thompson, *Silicon quantum photonics,* IEEE Journal of Selected Topics in Quantum Electronics **22**, 390 (2016).

[16] A. D. O'Connell, M. Hofheinz, M. Ansmann, R. C. Bialczak, M. Lenander, E. Lucero, M. Neeley, D. Sank, H. Wang, M. Weides, J. Wenner, J. M. Martinis, and A. N. Cleland, *Quantum ground state and single-phonon control of a mechanical resonator,* Nature **464**, 697 (2010).

[17] Y. Chu, P. Kharel, W. H. Renninger, L. D. Burkhart, L. Frunzio, P. T. Rakich, and R. J. Schoelkopf, *Quantum acoustics with superconducting qubits,* Science **358**, 199 (2017).

[18] Y. Chu, P. Kharel, T. Yoon, L. Frunzio, P. T. Rakich, and R. J. Schoelkopf, *Creation and control of multi-phonon fock states in a bulk acoustic-wave resonator,* Nature **563**, 666 (2018).

[19] A. Bienfait, K. J. Satzinger, Y. P. Zhong, H.-S. Chang, M.-H. Chou, C. R. Conner, E. Dumur, J. Grebel, G. A. Peairs, R. G. Povey, and A. N. Cleland, *Phonon-mediated quantum state transfer and remote qubit entanglement,* Science **364**, 368 (2019).

[20] P. Arrangoiz-Arriola, E. A. Wollack, M. Pechal, J. D. Witmer, J. T. Hill, and A. H. Safavi-Naeini, *Coupling a superconducting quantum circuit to a phononic crystal defect cavity,* Phys. Rev. X **8**, 031007 (2018).

[21] S. Barzanjeh, M. Wulf, M. Peruzzo, M. Kalaee, P. B. Dieterle, O. Painter, and J. M. Fink, *Mechanical on-chip microwave circulator,* Nature Communications **8**, 953 (2017).

[22] M. Kalaee, M. Mirhosseini, P. B. Dieterle, M. Peruzzo, J. M. Fink, and O. Painter, *Quantum electromechanics of a hypersonic crystal,* Nature Nanotechnology **14**, 334 (2019).

[23] J. Bochmann, A. Vainsencher, D. D. Awschalom, and A. N. Cleland, *Nanomechanical coupling between microwave and optical photons,* Nature Phys. **9**, 712 (2013).

[24] R. W. Andrews, R. W. Peterson, T. P. Purdy, K. Cicak, R. W. Simmonds, C. A. Regal, and K. W. Lehnert, *Bidirectional and efficient conversion between microwave and optical light,* Nature Phys. **10**, 321 (2014).

[25] T. Bagci, A. Simonsen, S. Schmid, L. G. Villanueva, E. Zeuthen, J. Appel, J. Taylor, A. Sørensen, K. Usami, A. Schliesser, and E. Polzik, *Optical detection of radio waves through a nanomechanical transducer.* Nature **507**, 81 (2014).

[26] A. Vainsencher, K. J. Satzinger, G. A. Peairs, and A. N. Cleland, *Bi-directional conversion between microwave and optical frequencies in a piezoelectric optomechanical device,* Appl. Phys. Lett. **109**, 033107 (2016).

[27] K. C. Balram, M. I. Davanço, J. D. Song, and K. Srinivasan, *Coherent coupling between radiofrequency, optical and acoustic waves in piezo-optomechanical circuits,* Nature Photon. **10**, 346 (2016).

[28] M. Forsch, R. Stockill, A. Wallucks, I. Marinković, C. Gärtner, R. A. Norte, F. van Otten, A. Fiore, K. Srinivasan, and S. Gröblacher, *Microwave-to-optics conversion using a mechanical oscillator in its quantum ground state,* Nature Physics (2019), 10.1038/s41567-019-0673-7.

[29] A. J. Leggett, *Testing the limits of quantum mechanics: motivation, state of play, prospects,* Journal of Physics: Condensed Matter **14**, R415 (2002).

[30] I. Pikovski, M. R. Vanner, M. Aspelmeyer, M. S. Kim, and Č. Brukner, *Probing planck-scale physics with quantum optics,* Nature Phys. **8**, 393 (2012).

[31] R. Penrose, *On gravity's role in quantum state reduction,* General Relativity and Gravitation **28**, 581 (1996).

[32] S. Bose, K. Jacobs, and P. L. Knight, *Scheme to probe the decoherence of a macroscopic object,* Physical Review A **59**, 3204 (1999).

[33] G. C. Ghirardi, A. Rimini, and T. Weber, *Unified dynamics for microscopic and macroscopic systems,* Physical Review D **34**, 470 (1986).

[34] S. Nimmrichter, K. Hornberger, and K. Hammerer, *Optomechanical sensing of spontaneous wave-function collapse,* Physical Review Letters **113**, 020405 (2014).

[35] S. Belli, R. Bonsignori, G. D'Auria, L. Fant, M. Martini, S. Peirone, S. Donadi, and A. Bassi, *Entangling macroscopic diamonds at room temperature: Bounds on the continuous-spontaneous-localization parameters,* Physical Review A **94**, 012108 (2016).

[36] M. Carlesso and S. Donadi, *Collapse models: main properties and the state of art of the experimental tests,* http://arxiv.org/abs/1907.12460v1 .

[37] B. Schrinski, S. Nimmrichter, B. A. Stickler, and K. Hornberger, *Macroscopicity of quantum mechanical superposition tests via hypothesis falsification,* Physical Review A **100**, 032111 (2019).

[38] A. G. J. Harms, *Characterization of optical losses using microdisk cavities*, Master's thesis, TU Delft (2017).

[39] K. N. A. van Bezouw, *Assessment of absorption losses in optomechanical microdisk resonator devices*, Master's thesis, TU Delft (2019).

[40] W. Kern and D. A. Puotinen, *Cleaning solutions based on hydrogen peroxide for use in silicon semiconductor technology,* RCA Rev. **31**, 187 (1970).

[41] R. van der Kolk, *Optimising the fabrication of optical microdisks*, Master's thesis, TU Delft (2019).

[42] I. Marinković, *Optomechanical devices in the quantum regime*, Ph.D. thesis, TU Delft (2019).

[43] S. Gröblacher, J. T. Hill, A. H. Safavi-Naeini, J. Chan, and O. Painter, *Highly efficient coupling from an optical fiber to a nanoscale silicon optomechanical cavity,* Appl. Phys. Lett., **103**, 181104 (2013).

[44] A. J. R. MacDonald, G. G. Popowich, B. D. Hauer, P. H. Kim, A. Fredrick, X. Rojas, P. Doolin, and J. P. Davis, *Optical microscope and tapered fiber coupling apparatus for a dilution refrigerator,* Review of Scientific Instruments **86**, 013107 (2015).

[45] J. D. Thompson, T. G. Tiecke, N. P. de Leon, J. Feist, A. V. Akimov, M. Gullans, A. S. Zibrov, V. Vuletić, and M. D. Lukin, *Coupling a single trapped atom to a nanoscale optical cavity,* Science **340**, 1202 (2013).

[46] L. Neuhaus, R. Metzdorff, S. Chua, T. Jacqmin, T. Briant, A. Heidmann, P.-F. Cohadon, and S. Deleglise, *PyRPL (python red pitaya lockbox) — an open-source software package for FPGA-controlled quantum optics experiments,* in *2017 Conference on Lasers and Electro-Optics Europe & European Quantum Electronics Conference (CLEO/Europe-EQEC)* (IEEE, 2017).

[47] A. H. Safavi-Naeini, J. Chan, J. T. Hill, S. Gröblacher, H. Miao, Y. Chen, M. Aspelmeyer, and O. Painter, *Laser noise in cavity-optomechanical cooling and thermometry,* New J. Phys. **15**, 035007 (2013).

[48] J. P. Moura, *Making light jump*, Ph.D. thesis, TU Delft (2019).

[49] M. Vlassov, *Optical filters used in quantum optomechanics,* (2016).

[50] A. G. Krause, *Acceleration Sensing, Feedback Cooling, and Nonlinear Dynamics with Nanoscale Cavity-Optomechanical Devices*, Ph.D. thesis, California Institute of Technology (2015).

[51] I. Marinković, A. Wallucks, R. Riedinger, S. Hong, M. Aspelmeyer, and S. Gröblacher, *Optomechanical Bell test,* Phys. Rev. Lett. **121**, 220404 (2018).

[52] S. Hong, R. Riedinger, I. Marinković, A. Wallucks, S. G. Hofer, R. A. Norte, M. Aspelmeyer, and S. Gröblacher, *Hanbury Brown and Twiss interferometry of single phonons from an optomechanical resonator,* Science **358**, 203 (2017).

[53] J. Chan, T. P. M. Alegre, A. H. Safavi-Naeini, J. T. Hill, A. Krause, S. Gröblacher, M. Aspelmeyer, and O. Painter, *Laser cooling of a nanomechanical oscillator into its quantum ground state,* Nature **478**, 89 (2011).

[54] J. J. Sakurai, *Modern Quantum mechanics* (Addison-Wesley publishing Company, Inc., 1994).

[55] S. G. Hofer, W. Wieczorek, M. Aspelmeyer, and K. Hammerer, *Quantum entanglement and teleportation in pulsed cavity optomechanics,* Phys. Rev. A **84**, 52327 (2011).

[56] C. Galland, N. Sangouard, N. Piro, N. Gisin, and T. J. Kippenberg, *Heralded Single-Phonon Preparation, Storage, and Readout in Cavity Optomechanics,* Phys. Rev. Lett. **112**, 143602 (2014).

[57] R. Riedinger, S. Hong, R. A. Norte, J. A. Slater, J. Shang, A. G. Krause, V. Anant, M. Aspelmeyer, and S. Gröblacher, *Non-classical correlations between single photons and phonons from a mechanical oscillator,* Nature **530**, 313 (2016).

[58] M. D. Anderson, S. T. Velez, K. Seibold, H. Flayac, V. Savona, N. Sangouard, and C. Galland, *Two-color pump-probe measurement of photonic quantum correlations mediated by a single phonon,* Physical Review Letters **120**, 233601 (2018).

[59] J. R. Johansson, P. D. Nation, and F. Nori, *Qutip: An open-source python framework for the dynamics of open quantum systems,* Comp. Phys. Comm. **183**, 1760 (2012).

[60] J. R. Johansson, P. D. Nation, and F. Nori, *Qutip 2: A python framework for the dynamics of open quantum systems,* Comp. Phys. Comm. **184**, 1234 (2013).

[61] K. Jensen, W. Wasilewski, H. Krauter, T. Fernholz, B. M. Nielsen, M. Owari, M. B. Plenio, A. Serafini, M. M. Wolf, and E. S. Polzik, *Quantum memory for entangled continuous-variable states,* Nature Phys. **7**, 13 (2011).

[62] K. F. Reim, P. Michelberger, K. C. Lee, J. Nunn, N. K. Langford, and I. A. Walmsley, *Single-photon-level quantum memory at room temperature,* Phys. Rev. Lett. **107**, 053603 (2011).

[63] C. W. Chou, H. de Riedmatten, D. Felinto, S. V. Polyakov, S. J. van Enk, and H. J. Kimble, *Measurement-induced entanglement for excitation stored in remote atomic ensembles,* Nature **438**, 828 (2005).

[64] D. N. Matsukevich, T. Chanelieère, S. D. Jenkins, S.-Y. Lan, T. A. B. Kennedy, and A. Kuzmich, *Entanglement of remote atomic qubits,* Phys. Rev. Lett. **96**, 030405 (2006).

[65] S. Ritter, C. Nölleke, C. Hahn, A. Reiserer, A. Neuzner, M. Uphoff, M. Mücke, E. Figueroa, J. Bochmann, and G. Rempe, *An elementary quantum network of single atoms in optical cavities,* Nature **484**, 195 (2012).

[66] D. L. Moehring, P. Maunz, S. Olmschenk, K. C. Younge, D. N. Matsukevich, L.-M. Duan, and C. Monroe, *Entanglement of single-atom quantum bits at a distance,* Nature **449**, 68 (2007).

[67] J. D. Jost, J. P. Home, J. M. Amini, D. Hanneke, R. Ozeri, C. Langer, J. J. Bollinger, D. Leibfried, and D. J. Wineland, *Entangled mechanical oscillators,* Nature **459**, 683 (2009).

[68] I. Usmani, C. Clausen, F. Bussières, N. Sangouard, M. Afzelius, and N. Gisin, *Heralded quantum entanglement between two crystals,* Nature Photon. **6**, 234 (2012).

[69] E. Saglamyurek, J. Jin, V. B. Verma, M. D. Shaw, F. Marsili, S. W. Nam, D. Oblak, and W. Tittel, *Quantum storage of entangled telecom-wavelength photons in an erbium-doped optical fibre,* Nature Photon. **9**, 83 (2015).

[70] B. Hensen, H. Bernien, A. E. Dréau, A. Reiserer, N. Kalb, M. S. Blok, J. Ruitenberg, R. F. L. Vermeulen, R. N. Schouten, C. Abellán, W. Amaya, V. Pruneri, M. W. Mitchell, M. Markham, D. J. Twitchen, D. Elkouss, S. Wehner, T. H. Taminiau, and R. Hanson, *Loophole-free Bell inequality violation using electron spins separated by 1.3 kilometres,* Nature **526**, 682 (2015).

[71] J. D. Teufel, T. Donner, D. Li, J. W. Harlow, M. S. Allman, K. Cicak, A. J. Sirois, J. D. Whittaker, K. W. Lehnert, and R. W. Simmonds, *Sideband cooling of micromechanical motion to the quantum ground state,* Nature **475**, 359 (2011).

[72] T. Palomaki, J. Teufel, R. Simmonds, and K. Lehnert, *Entangling mechanical motion with microwave fields,* Science **342**, 710 (2013).

[73] E. E. Wollman, C. U. Lei, A. J. Weinstein, J. Suh, A. Kronwald, F. Marquardt, A. A. Clerk, and K. C. Schwab, *Quantum squeezing of motion in a mechanical resonator,* Science **349**, 952 (2015).

[74] A. P. Reed, K. H. Mayer, J. D. Teufel, L. D. Burkhart, W. Pfaff, M. Reagor, L. Sletten, X. Ma, R. J. Schoelkopf, E. Knill, and K. W. Lehnert, *Faithful conversion of propagating quantum information to mechanical motion,* Nature Phys. **13**, 1163 (2017).

[75] K. C. Lee, M. R. Sprague, B. J. Sussman, J. Nunn, N. K. Langford, X.-M. Jin, T. Champion, P. Michelberger, K. F. Reim, D. England, D. Jaksch, and I. A. Walmsley, *Entangling macroscopic diamonds at room temperature,* Science **334**, 1253 (2011).

[76] S. M. Meenehan, J. D. Cohen, G. S. MacCabe, F. Marsili, M. D. Shaw, and O. Painter, *Pulsed Excitation Dynamics of an Optomechanical Crystal Resonator near Its Quantum Ground State of Motion,* Phys. Rev. X **5**, 041002 (2015).

[77] M. Razavi, M. Piani, and N. Lütkenhaus, *Quantum repeaters with imperfect memories: cost and scalability,* Phys. Rev. A **80**, 032301 (2009).

[78] K. Børkje, A. Nunnenkamp, and S. M. Girvin, *Proposal for entangling remote micromechanical oscillators via optical measurements,* Phys. Rev. Lett. **107**, 123601 (2011).

[79] W. Wieczorek, S. G. Hofer, J. Hoelscher-Obermaier, R. Riedinger, K. Hammerer, and M. Aspelmeyer, *Optimal state estimation for cavity optomechanical systems,* Phys. Rev. Lett. **114**, 223601 (2015).

[80] T. Asano, Y. Ochi, Y. Takahashi, K. Kishimoto, and S. Noda, *Photonic crystal nanocavity with a Q factor exceeding eleven million,* Opt. Express **25**, 1769 (2017).

[81] R. N. Patel, C. J. Sarabalis, W. Jiang, J. T. Hill, and A. H. Safavi-Naeini, *Engineering phonon leakage in nanomechanical resonators,* Phys. Rev. Applied **8**, 041001 (2017).

[82] N. Maring, P. Farrera, K. Kutluer, M. Mazzera, G. Heinze, and H. de Riedmatten, *Photonic quantum state transfer between a cold atomic gas and a crystal,* Nature **551**, 485 (2017).

[83] A. Rueda, F. Sedlmeir, M. C. Collodo, U. Vogl, B. Stiller, G. Schunk, D. V. Strekalov, C. Marquardt, J. M. Fink, O. Painter, G. Leuchs, and H. G. L. Schwefel, *Efficient microwave to optical photon conversion: an electro-optical realization,* Optica **3**, 597 (2016).

[84] A. P. Higginbotham, P. S. Burns, M. D. Urmey, R. W. Peterson, N. S. Kampel, B. M. Brubaker, G. Smith, K. W. Lehnert, and C. A. Regal, *Electro-optic correlations improve an efficient mechanical converter,* Nature Phys. **14**, 1038 (2018).

[85] K. Fang, J. Luo, A. Metelmann, M. H. Matheny, F. Marquardt, A. A. Clerk, and O. Painter, *Generalized non-reciprocity in an optomechanical circuit via synthetic magnetism and reservoir engineering,* Nature Phys. **13**, 465 (2017).

[86] R. C. Cumming, *The serrodyne frequency translator,* Proc. IRE **45**, 175 (1957).

[87] K. K. Wong, R. M. D. L. Rue, and S. Wright, *Electro-optic-waveguide frequency translator in linbo$_3$ fabricated by proton exchange,* Opt. Lett. **7**, 546 (1982).

[88] R. Horodecki, P. Horodecki, M. Horodecki, and K. Horodecki, *Quantum entanglement,* Rev. Mod. Phys. **81**, 865 (2009).

[89] S. Hill and W. K. Wootters, *Entanglement of a pair of quantum bits,* Phys. Rev. Lett. **78**, 5022 (1997).

[90] A. Kuzmich, W. P. Bowen, A. D. Boozer, A. Boca, C. W. Chou, L.-M. Duan, and H. J. Kimble, *Generation of nonclassical photon pairs for scalable quantum communication with atomic ensembles,* Nature **423**, 731 (2003).

[91] K. C. Lee, *Generation of room-temperature entanglement in diamond with broadband pulses*, Ph.D. thesis, University of Oxford (2012).

[92] J. S. Bell, *On the Einstein Podolsky Rosen Paradox,* Physics **1**, 195 (1964).

[93] A. Einstein, B. Podolsky, and N. Rosen, *Can quantum-mechanical description of physical reality be considered complete?* Physical Review **47**, 777 (1935).

[94] N. Bohr, *Can quantum-mechanical description of physical reality be considered complete?* Phys. Rev. **48**, 696 (1935).

[95] J. F. Clauser, M. A. Horne, A. Shimony, and R. A. Holt, *Proposed experiment to test local hidden-variable theories,* Phys. Rev. Lett. **23**, 880 (1970).

[96] S. J. Freedman and J. F. Clauser, *Experimental test of local hidden-variable theories,* Phys. Rev. Lett. **28**, 938 (1972).

[97] A. Aspect, P. Grangier, and G. Roger, *Experimental tests of realistic local theories via Bell's theorem,* Phys. Rev. Lett. **47**, 460 (1981).

[98] Y. H. Shih and C. O. Alley, *New Type of Einstein-Podolsky-Rosen-Bohm Experiment Using Pairs of Light Quanta Produced by Optical Parametric Down Conversion,* Phys. Rev. Lett. **61**, 2921 (1988).

[99] J. G. Rarity and P. R. Tapster, *Experimental violation of Bell's inequality based on phase and momentum,* Phys. Rev. Lett. **64**, 2495 (1990).

[100] P. G. Kwiat, K. Mattle, H. Weinfurter, A. Zeilinger, A. V. Sergienko, and Y. Shih, *New high-intensity source of polarization-entangled photon pairs,* Phys. Rev. Lett. **75**, 4337 (1995).

[101] G. Weihs, T. Jennewein, C. Simon, H. Weinfurter, and A. Zeilinger, *Violation of Bell's inequality under strict Einstein locality conditions,* Phys. Rev. Lett. **81**, 5039 (1998).

[102] M. A. Rowe, D. Kielpinski, V. Meyer, C. A. Sackett, W. M. Itan, C. Monroe, and D. J. Wineland, *Experimental violation of a Bell's inequality with efficient detection,* Nature **409**, 791 (2001).

[103] M. Giustina, M. A. M. Versteegh, S. Wengerowsky, J. Handsteiner, A. Hochrainer, K. Phelan, F. Steinlechner, J. Kofler, J.-A. Larsson, C. Abellán, W. Amaya, V. Pruneri, M. W. Mitchell, J. Beyer, T. Gerrits, A. E. Lita, L. K. Shalm, S. W. Nam, T. Scheidl, R. Ursin, B. Wittmann, and A. Zeilinger, *Significant-Loophole-Free Test of Bell's Theorem with Entangled Photons,* Phys. Rev. Lett. **115**, 250401 (2015).

[104] L. K. Shalm, E. Meyer-Scott, B. G. Christensen, P. Bierhorst, M. A. Wayne, M. J. Stevens, T. Gerrits, S. Glancy, D. R. Hamel, M. S. Allman, K. J. Coakley, S. D. Dyer, C. Hodge, A. E. Lita, V. B. Verma, C. Lambrocco, E. Tortorici, A. L. Migdall, Y. Zhang, D. R. Kumor, W. H. Farr, F. Marsili, M. D. Shaw, J. A. Stern, C. Abellán, W. Amaya, V. Pruneri, T. Jennewein, M. W. Mitchell, P. G. Kwiat, J. C. Bienfang, R. P. Mirin, E. Knill, and S. W. Nam, *Strong loophole-free test of local realism,* Phys. Rev. Lett. **115**, 250402 (2015).

[105] W. Rosenfeld, D. Burchardt, R. Garthoff, K. Redeker, N. Ortegel, M. Rau, and H. Weinfurter, *Event-Ready Bell Test Using Entangled Atoms Simultaneously Closing Detection and Locality Loopholes,* Phys. Rev. Lett. **119**, 010402 (2017).

[106] J. T. Barreiro, J.-D. Bancal, P. Schindler, D. Nigg, M. Hennrich, T. Monz, N. Gisin, and R. Blatt, *Demonstration of genuine multipartite entanglement with device-independent witnesses,* Nature Phys. **9**, 559 (2013).

[107] R. Schmied, J.-D. Bancal, B. Allard, M. Fadel, V. Scarani, P. Treutlein, and N. Sangouard, *Bell correlations in a Bose-Einstein condensate,* Science **352**, 441 (2016).

[108] M. Ansmann, H. Wang, R. C. Bialczak, M. Hofheinz, E. Lucero, M. Neeley, A. D. O'Connell, D. Sank, M. Weides, J. Wenner, A. N. Cleland, and J. M. Martinis, *Violation of Bell's inequality in Josephson phase qubits,* Nature **461**, 504 (2009).

[109] S. Pironio, A. Acín, S. Massar, A. B. de la Giroday, D. N. Matsukevich, P. Maunz, S. Olmschenk, D. Hayes, L. Luo, T. A. Manning, and C. Monroe, *Random numbers certified by Bell's theorem,* Nature **464**, 1021 (2010).

[110] P. Bierhorst, E. Knill, S. Glancy, Y. Zhang, A. Mink, S. Jordan, A. Rommal, Y.-K. Liu, B. Christensen, S. W. Nam, M. J. Stevens, and L. K. Shalm, *Experimentally generated randomness certified by the impossibility of superluminal signals,* Nature **556**, 223 (2018).

[111] A. Acín, N. Brunner, N. Gisin, S. Massar, S. Pironio, and V. Scarani, *Device-independent security of quantum cryptography against collective attacks,* Phys. Rev. Lett. **98**, 230501 (2007).

[112] P. Sekatski, J.-D. Bancal, S. Wagner, and N. Sangouard, *Certifying the building blocks of quantum computers from Bell's theorem,* Phys. Rev. Lett. **121**, 180505 (2018).

[113] E. Schrödinger, *Die gegenwärtige Situation in der Quantenmechanik,* Die Naturwissenschaften **48**, 807 (1935).

[114] R. Riedinger, A. Wallucks, I. Marinković, C. Löschnauer, M. Aspelmeyer, S. Hong, and S. Gröblacher, *Remote quantum entanglement between two micromechanical oscillators,* Nature **556**, 473 (2018).

[115] C. F. Ockeloen-Korppi, E. Damskägg, J.-M. Pirkkalainen, M. Asjad, A. A. Clerk, F. Massel, M. J. Woolley, and M. A. Sillanpää, *Stabilized entanglement of massive mechanical oscillators,* Nature **556**, 478 (2018).

[116] S. J. van Enk, N. Lütkenhaus, and H. J. Kimble, *Experimental procedures for entanglement verification,* Phys. Rev. A **75**, 052318 (2007).

[117] V. C. Vivoli, T. Barnea, C. Galland, and N. Sangouard, *Proposal for an Optomechanical Bell Test,* Phys. Rev. Lett. **116**, 070405 (2016).

[118] S. G. Hofer, K. W. Lehnert, and K. Hammerer, *Proposal to Test Bell's Inequality in Electromechanics,* Phys. Rev. Lett. **116**, 070406 (2016).

[119] J. Chan, A. H. Safavi-Naeini, J. T. Hill, S. Meenehan, and O. Painter, *Optimized optomechanical crystal cavity with acoustic radiation shield,* App. Phys. Lett. **101**, 081115 (2012).

[120] M. A. Horne, A. Shimony, and A. Zeilinger, *Two-particle interferometry,* Phys. Rev. Lett. **62**, 2209 (1989).

[121] H. de Riedmatten, J. Laurat, C. W. Chou, E. W. Schomburg, D. Felinto, and H. J. Kimble, *Direct measurement of decoherence for entanglement between a photon and stored atomic excitation,* Phys. Rev. Lett. **97**, 113603 (2006).

[122] B. S. Cirel'son, *Quantum generalizations of Bell's inequality,* Lett. Math. Phys. **4**, 93 (1980).

[123] A. Bassi, K. Lochan, S. Satin, T. P. Singh, and H. Ulbricht, *Models of wave-function collapse, underlying theories, and experimental tests,* Rev. Mod. Phys. **85**, 471 (2013).

[124] S. Bose, A. Mazumdar, G. W. Morley, H. Ulbricht, M. Toroš, M. Paternostro, A. A. Geraci, P. F. Barker, M. S. Kim, and G. Milburn, *Spin entanglement witness for quantum gravity,* Phys. Rev. Lett. **119**, 240401 (2017).

[125] C. Marletto and V. Vedral, *Gravitationally induced entanglement between two massive particles is sufficient evidence of quantum effects in gravity,* Phys. Rev. Lett. **119**, 240402 (2017).

[126] J. Minář, H. de Riedmatten, C. Simon, H. Zbinden, and N. Gisin, *Phase-noise measurements in long-fiber interferometers for quantum-repeater applications,* Phys. Rev. A **77**, 052325 (2008).

[127] C. Simon, *Towards a global quantum network,* Nature Photon. **11**, 678 (2017).

[128] Y. Wang, M. Um, J. Zhang, S. An, M. Lyu, J.-N. Zhang, L.-M. Duan, D. Yum, and K. Kim, *Single-qubit quantum memory exceeding ten-minute coherence time,* Nature Photon. **11**, 646 (2017).

[129] C. Crocker, M. Lichtman, K. Sosnova, A. Carter, S. Scarano, and C. Monroe, *High purity single photons entangled with an atomic qubit,* Optics Express **27**, 28143 (2019).

[130] S.-J. Yang, X.-J. Wang, X.-H. Bao, and J.-W. Pan, *An efficient quantum light-matter interface with sub-second lifetime,* Nature Photon. **10**, 381 (2016).

[131] D. Saunders, J. Munns, T. Champion, C. Qiu, K. Kaczmarek, E. Poem, P. Ledingham, I. Walmsley, and J. Nunn, *Cavity-enhanced room-temperature broadband raman memory,* Phys. Rev. Lett. **116**, 090501 (2016).

[132] Y. Wang, J. Li, S. Zhang, K. Su, Y. Zhou, K. Liao, S. Du, H. Yan, and S.-L. Zhu, *Efficient quantum memory for single-photon polarization qubits,* Nature Photon. **13**, 346 (2019).

[133] N. Kalb, A. Reiserer, S. Ritter, and G. Rempe, *Heralded storage of a photonic quantum bit in a single atom,* Phys. Rev. Lett. **114**, 220501 (2015).

[134] C. E. Bradley, J. Randall, M. H. Abobeih, R. C. Berrevoets, M. J. Degen, M. A. Bakker, M. Markham, D. J. Twitchen, and T. H. Taminiau, *A 10-qubit solid-state spin register with quantum memory up to one minute,* arXiv:1905.02094 (2019).

[135] J. Dajczgewand, J.-L. L. G. A. Louchet-Chauvet, and T. Chaneliere, *Large efficiency at telecom wavelength for optical quantum memories,* Optics Letters **39**, 2711 (2014).

[136] I. Craiciu, M. Lei, J. Rochman, J. M. Kindem, J. G. Bartholomew, E. Miyazono, T. Zhong, N. Sinclair, and A. Faraon, *Nanophotonic quantum storage at telecommunication wavelength,* Physical Review Applied **12**, 024062 (2019).

[137] M. F. Askarani, M. G. Puigibert, T. Lutz, V. B. Verma, M. D. Shaw, S. W. Nam, N. Sinclair, D. Oblak, and W. Tittel, *Storage and reemission of heralded telecommunication-wavelength photons using a crystal waveguide,* Phys. Rev. Applied **11**, 054056 (2019).

[138] R. Manenti, A. F. Kockum, A. Patterson, T. Behrle, J. Rahamim, G. Tancredi, F. Nori, and P. J. Leek, *Circuit quantum acoustodynamics with surface acoustic waves,* Nature Commun. **8**, 975 (2017).

[139] L. R. Sletten, B. A. Moores, J. J. Viennot, and K. W. Lehnert, *Resolving phonon fock states in a multimode cavity with a double-slit qubit,* Phys. Rev. X **9**, 021056 (2019).

[140] P. Arrangoiz-Arriola, E. A. Wollack, Z. Wang, M. Pechal, W. Jiang, T. P. McKenna, J. D. Witmer, R. V. Laer, and A. H. Safavi-Naeini, *Resolving the energy levels of a nanomechanical oscillator,* Nature **571**, 537 (2019).

[141] T. P. Purdy, K. E. Grutter, K. Srinivasan, and J. M. Taylor, *Quantum correlations from a room-temperature optomechanical cavity,* Science **356**, 1265 (2017).

[142] J. Chen, M. Rossi, D. Mason, and A. Schliesser, *Entanglement of propagating optical modes via a mechanical interface,* http://arxiv.org/abs/1911.05729v2 .

[143] P. Kharel, Y. Chu, M. Power, W. H. Renninger, R. J. Schoelkopf, and P. T. Rakich, *Ultra-high-q phononic resonators on-chip at cryogenic temperatures,* APL Photonics **3**, 066101 (2018).

[144] A. H. Safavi-Naeini, J. Chan, J. T. Hill, T. P. M. Alegre, A. Krause, and O. Painter, *Observation of quantum motion of a nanomechanical resonator,* Phys. Rev. Lett. **108**, 033602 (2012).

[145] A. I. Lvovsky and J. Mlynek, *Quantum-optical catalysis: Generating nonclassical states of light by means of linear optics,* Phys. Rev, Lett. **88**, 250401 (2002).

[146] K. J. Resch, J. S. Lundeen, and A. M. Steinberg, *Quantum state preparation and conditional coherence,* Phys. Rev. Lett. **88**, 113601 (2002).

[147] W. A. Phillips, *Two-level states in glasses,* Reports on Progress in Physics **50**, 1657 (1987).

[148] C. Müller, J. H. Cole, and J. Lisenfeld, *Towards understanding two-level-systems in amorphous solids: insights from quantum circuits,* Reports on Progress in Physics **82**, 124501 (2019).

[149] M. Constantin, C. C. Yu, and J. M. Martinis, *Saturation of two-level systems and charge noise in josephson junction qubits,* Phys. Rev. B **79**, 094520 (2009).

[150] R. O. Behunin, P. Kharel, W. H. Renninger, and P. T. Rakich, *Engineering dissipation with phononic spectral hole burning,* Nature Materials **16**, 315 (2016).

[151] K. S. Choi, H. Deng, J. Laurat, and H. J. Kimble, *Mapping photonic entanglement into and out of a quantum memory,* Nature **452**, 67 (2008).

[152] L. Qiu, I. Shomroni, P. Seidler, and T. J. Kippenberg, *High-fidelity laser cooling to the quantum ground state of a silicon nanomechanical oscillator,* http://arxiv.org/abs/1903.10242v1 .

[153] H. Okamoto, I. Mahboob, K. Onomitsu, and H. Yamaguchi, *Rapid switching in high-q mechanical resonators,* Applied Physics Letters **105**, 083114 (2014).

[154] A. H. Safavi-Naeini, J. T. Hill, S. Meenehan, J. Chan, S. Gröblacher, and O. Painter, *Two-dimensional phononic-photonic band gap optomechanical crystal cavity,* Physical Review Letters **112**, 153603 (2014).

[155] H. Ren, M. H. Matheny, G. S. MacCabe, J. Luo, H. Pfeifer, M. Mirhosseini, and O. Painter, *Two-dimensional optomechanical crystal cavity with high quantum cooperativity,* http://arxiv.org/abs/1910.02873v1 .

[156] W. H. Renninger, P. Kharel, R. O. Behunin, and P. T. Rakich, *Bulk crystalline optomechanics,* Nature Phys. **14**, 601 (2018).

[157] R. O. Behunin, F. Intravaia, and P. T. Rakich, *Dimensional transformation of defect-induced noise, dissipation, and nonlinearity,* Phys. Rev. B **93**, 224110 (2016).

[158] M. J. Burek, J. D. Cohen, S. M. Meenehan, N. El-Sawah, C. Chia, T. Ruelle, S. Meesala, J. Rochman, H. A. Atikian, M. Markham, D. J. Twitchen, M. D. Lukin, O. Painter, and M. Lončar, *Diamond optomechanical crystals,* Optica **3**, 1404 (2016).

[159] R. Stockill, M. Forsch, G. Beaudoin, K. Pantzas, I. Sagnes, R. Braive, and S. Gröblacher, *Gallium phosphide as a piezoelectric platform for quantum optomechanics,* Physical Review Letters **123**, 163602 (2019).

[160] S. Rips and M. J. Hartmann, *Quantum information processing with nanomechanical qubits,* Physical Review Letters **110**, 120503 (2013).

[161] K. Stannigel, P. Komar, S. J. M. Habraken, S. D. Bennett, M. D. Lukin, P. Zoller, and P. Rabl, *Optomechanical quantum information processing with photons and phonons,* Physical Review Letters **109**, 013603 (2012).

[162] A. Shkarin, N. Flowers-Jacobs, S. Hoch, A. Kashkanova, C. Deutsch, J. Reichel, and J. Harris, *Optically mediated hybridization between two mechanical modes,* Physical Review Letters **112**, 013602 (2014).

[163] M. J. Weaver, F. Buters, F. Luna, H. Eerkens, K. Heeck, S. de Man, and D. Bouwmeester, *Coherent optomechanical state transfer between disparate mechanical resonators,* Nat. Comm. **8**, 824 (2017).

[164] T. Faust, J. Rieger, M. J. Seitner, J. P. Kotthaus, and E. M. Weig, *Coherent control of a classical nanomechanical two-level system,* Nature Physics **9**, 485 (2013).

[165] H. Okamoto, A. Gourgout, C.-Y. Chang, K. Onomitsu, I. Mahboob, E. Y. Chang, and H. Yamaguchi, *Coherent phonon manipulation in coupled mechanical resonators,* Nature Physics **9**, 480 (2013).

[166] K. Stannigel, P. Rabl, A. S. Sørensen, P. Zoller, and M. D. Lukin, *Optomechanical Transducers for Long-Distance Quantum Communication,* Phys. Rev. Lett. **105**, 220501 (2010).

[167] C. Zhong, Z. Wang, C. Zou, M. Zhang, X. Han, W. Fu, M. Xu, S. Shankar, M. H. Devoret, H. X. Tang, and L. Jiang, *Heralded generation and detection of entangled microwave–optical photon pairs,* http://arxiv.org/abs/1901.08228v1 .

[168] S. Barz, E. Kashefi, A. Broadbent, J. F. Fitzsimons, A. Zeilinger, and P. Walther, *Demonstration of blind quantum computing,* Science **335**, 303 (2012).

[169] M. Jakobi, C. Simon, N. Gisin, J.-D. Bancal, C. Branciard, N. Walenta, and H. Zbinden, *Practical private database queries based on a quantum-key-distribution protocol,* Physical Review A **83**, 022301 (2011).

[170] S. Pirandola, U. L. Andersen, L. Banchi, M. Berta, D. Bunandar, R. Colbeck, D. Englund, T. Gehring, C. Lupo, C. Ottaviani, J. Pereira, M. Razavi, J. S. Shaari, M. Tomamichel, V. C. Usenko, G. Vallone, P. Villoresi, and P. Wallden, *Advances in quantum cryptography,* http://arxiv.org/abs/1906.01645v1 .

[171] P. Kómár, E. M. Kessler, M. Bishof, L. Jiang, A. S. Sørensen, J. Ye, and M. D. Lukin, *A quantum network of clocks,* Nature Physics **10**, 582 (2014).

[172] D. Gottesman, T. Jennewein, and S. Croke, *Longer-baseline telescopes using quantum repeaters,* Physical Review Letters **109**, 070503 (2012).

[173] E. Khabiboulline, J. Borregaard, K. D. Greve, and M. Lukin, *Optical interferometry with quantum networks,* Physical Review Letters **123**, 070504 (2019).

[174] D. Rideout, T. Jennewein, G. Amelino-Camelia, T. F. Demarie, B. L. Higgins, A. Kempf, A. Kent, R. Laflamme, X. Ma, R. B. Mann, E. Martín-Martínez, N. C. Menicucci, J. Moffat, C. Simon, R. Sorkin, L. Smolin, and D. R. Terno, *Fundamental quantum optics experiments conceivable with satellites—reaching relativistic distances and velocities,* Classical and Quantum Gravity **29**, 224011 (2012).

[175] D. N. Matsukevich, *Quantum state transfer between matter and light,* Science **306**, 663 (2004).

[176] J. Laurat, K. S. Choi, H. Deng, C. W. Chou, and H. J. Kimble, *Heralded entanglement between atomic ensembles: Preparation, decoherence, and scaling,* Physical Review Letters **99**, 180504 (2007).

[177] B. Zhao, Y.-A. Chen, X.-H. Bao, T. Strassel, C.-S. Chuu, X.-M. Jin, J. Schmiedmayer, Z.-S. Yuan, S. Chen, and J.-W. Pan, *A millisecond quantum memory for scalable quantum networks,* Nature Phys. **5**, 95 (2009).

[178] Y.-F. Pu, N. Jiang, W. Chang, H.-X. Yang, C. Li, and L.-M. Duan, *Experimental realization of a multiplexed quantum memory with 225 individually accessible memory cells,* Nature Communications **8**, 15359 (2017).

[179] M. P. Hedges, J. J. Longdell, Y. Li, and M. J. Sellars, *Efficient quantum memory for light,* Nature **465**, 1052 (2010).

[180] S. T. Velez, K. Seibold, N. Kipfer, M. D. Anderson, V. Sudhir, and C. Galland, *Preparation and decay of a single quantum of vibration at ambient conditions,* Physical Review X **9**, 041007 (2019).

[181] L. Jiang, J. M. Taylor, and M. D. Lukin, *Fast and robust approach to long-distance quantum communication with atomic ensembles,* Physical Review A **76**, 012301 (2007).

[182] B. Zhao, Z.-B. Chen, Y.-A. Chen, J. Schmiedmayer, and J.-W. Pan, *Robust creation of entanglement between remote memory qubits,* Physical Review Letters **98**, 240502 (2007).

[183] Z.-B. Chen, B. Zhao, Y.-A. Chen, J. Schmiedmayer, and J.-W. Pan, *Fault-tolerant quantum repeater with atomic ensembles and linear optics,* Physical Review A **76**, 022329 (2007).

[184] Z.-S. Yuan, Y.-A. Chen, B. Zhao, S. Chen, J. Schmiedmayer, and J.-W. Pan, *Experimental demonstration of a BDCZ quantum repeater node,* Nature **454**, 1098 (2008).

[185] H. P. Specht, C. Nölleke, A. Reiserer, M. Uphoff, E. Figueroa, S. Ritter, and G. Rempe, *A single-atom quantum memory,* Nature **473**, 190 (2011).

[186] A. G. Radnaev, Y. O. Dudin, R. Zhao, H. H. Jen, S. D. Jenkins, A. Kuzmich, and T. A. B. Kennedy, *A quantum memory with telecom-wavelength conversion,* Nature Physics **6**, 894 (2010).

[187] H. Bernien, B. Hensen, W. Pfaff, G. Koolstra, M. S. Blok, L. Robledo, T. H. Taminiau, M. Markham, D. J. Twitchen, L. Childress, and R. Hanson, *Heralded entanglement between solid-state qubits separated by three metres,* Nature **497**, 86 (2013).

[188] B. B. Blinov, D. L. Moehring, L.-M. Duan, and C. Monroe, *Observation of entanglement between a single trapped atom and a single photon,* Nature **428**, 153 (2004).

[189] R. Stockill, M. Stanley, L. Huthmacher, E. Clarke, M. Hugues, A. Miller, C. Matthiesen, C. L. Gall, and M. Atatüre, *Phase-tuned entangled state generation between distant spin qubits,* Physical Review Letters **119**, 010503 (2017).

[190] T. van Leent, M. Bock, R. Garthoff, K. Redeker, W. Zhang, T. Bauer, W. Rosenfeld, C. Becher, and H. Weinfurter, *Long-distance distribution of atom-photon entanglement at telecom wavelength,* http://arxiv.org/abs/1909.01006v1 .

[191] F. Bussières, C. Clausen, A. Tiranov, B. Korzh, V. B. Verma, S. W. Nam, F. Marsili, A. Ferrier, P. Goldner, H. Herrmann, C. Silberhorn, W. Sohler, M. Afzelius, and N. Gisin, *Quantum teleportation from a telecom-wavelength photon to a solid-state quantum memory,* Nature Photonics **8**, 775 (2014).

[192] T. Böttger, C. W. Thiel, R. L. Cone, and Y. Sun, *Effects of magnetic field orientation on optical decoherence in* Er^{3+}*:*Y_2SiO_5, Physical Review B **79**, 115104 (2009).

[193] M. Rančić, M. P. Hedges, R. L. Ahlefeldt, and M. J. Sellars, *Coherence time of over a second in a telecom-compatible quantum memory storage material,* Nature Phys. **14**, 50 (2017).

CURRICULUM VITÆ

Andreas WALLUCKS

14-02-1989 Born in Freiburg im Breisgau, Germany.

EDUCATION

2006–2008 High School
Rotteck Gymnasium, Freiburg, Germany

2008–2009 B.Sc. in Physics
Universität Freiburg, Germany

2009–2012 B.Sc. in Physics
Universität Konstanz, Germany

2012–2014 M.Sc. in Physics
Universität Konstanz, Germany
Thesis: Fabrication and annealing of metal nanoparticle aggregates
Promotor: Apl. Prof. Dr. J. Boneberg

2016–2020 Ph.D. Physics
Delft University of Technology, the Netherlands
Thesis: Towards an Optomechanical Quantum Memory
Promotor: Dr. S. Gröblacher
Promotor: Prof. Dr. Ir. H. S. J. van der Zant

LIST OF PUBLICATIONS

* indicates equal contribution

7. **A. Wallucks**, I. Marinković, B. Hensen, R. Stockill and S. Gröblacher, *A quantum memory at telecom wavelengths*, (under review).

6. M. Forsch*, R. Stockill*, **A. Wallucks**, I. Marinković, C. Gärtner, R. A. Norte, F. van Otten, A. Fiore, K. Srinivasan, and S. Gröblacher, *Microwave-to-optics conversion using a mechanical oscillator in its quantum groundstate*, Nature Physics (2019).

5. I. Marinković*, **A. Wallucks***, R. Riedinger, S. Hong, M. Aspelmeyer, and S. Gröblacher, *Optomechanical Bell Test*, Phys. Rev. Lett. **121**, 220404 (2018).

4. R. A. Norte, M. Forsch, **A. Wallucks**, I. Marinković, and S. Gröblacher, *Platform for Measurements of the Casimir Force between Two Superconductors*, Phys. Rev. Lett. **121**, 030405 (2018).

3. R. Riedinger*, **A. Wallucks***, I. Marinković*, C. Löschnauer, M. Aspelmeyer, S. Hong, and S. Gröblacher, *Remote quantum entanglement between two micromechanical oscillators*, Nature **556**, 473 – 477 (2018).

2. S. Hong*, R. Riedinger*, I. Marinković*, **A. Wallucks***, S. G. Hofer, R. A. Norte, M. Aspelmeyer, and S. Gröblacher, *Hanbury Brown and Twiss interferometry of single phonons from an optomechanical resonator*, Science **358**, 203 – 206 (2017).

1. F. Haering, U. Wiedwald, S. Nothelfer, B. Koslowski, P. Ziemann, L. Lechner, **A. Wallucks**, K. Lebecki, U. Nowak, J. Gräfe, E. Goering, and G. Schütz, *Switching modes in easy- and hard-axis magnetic reversal in a self-assembled antidot array*, Nanotechnology **24**, 465709 (2013).

ACKNOWLEDGEMENTS

After four years of working on the experiments presented in this thesis, I am happy to conclude by showing my gratitude to all the other people without whom this would not be possible. It has been a huge collaborative effort to enable the experiments with the nanobeams, from long before the start of my PhD, in two labs at the same time during it and with more experiments afterwards already in the planning. First and foremost, I want to thank you, Simon, for having me as a PhD student and putting me on this project. Thanks so much for all the confidence, motivation and clarity and for always giving me an opportunity to learn and grow. Thank you also for managing the group the way you do - it was an awesome experience for the whole four years and it has all to do with your management, communication and focus on teamwork. Herre, thank you for being my promoter and for the mentoring in between the years during our meetings.

With the work was done in collaboration, and I mostly need to thank you, Igor, for being the other half of the team silicon over the four years. Thanks for everything that I learned from you when I started as well over the rest of the years and also for reminding me to be goal oriented and pragmatic when it counts. I also want to thank the Vienna part of our team for enabling one of the closest collaborations I have seen so far. I truly enjoyed our work together, the atmosphere, and the continued exchanges to this day. So thanks a lot Markus for heading the Austrian part of this effort and for hosting me over the summer of 2016 in your lab. Sungkun, thanks so much for explaining all about the experiments to me and teaching me how to run the measurements. Ralf, I had a lot of fun working with you and especially learning how to come up with creative solutions.

Beyond the actual core silicon team, the group as a whole clearly had a mayor contribution to the work by always being extremely helpful, collaborative and most importantly exciting to be a part of. A special thanks to you, Richard, in my view you were greatly responsible for shaping the mentality of the lab in the beginning years to be such an open and fun environment and I have no doubt you will do so with your own group as well. João, as the first PhD of the group, you kind of paved the way for me and others and I am super thankful for all that you did. It's great to have you around in the lab and outside of it. Maarten, its was good fun doing our PhDs in parallell over the last four years. Thanks for always offering your judgment at exactly the right time and others. Claus, the beest, I appreciate you sharing all your fabrication knowledge. I also enjoyed the many coffees and dinners a lot. Moritz, thanks for always being so helpful and cheerful and also patient while explaining crystal structures to me. Rob, I learned a lot from discussing physics with you especially how there is always a different angle to view things in. Thanks so much also for your input to the experiments. Jingkun, thanks for all the times you supported the experiments and shared your equipment. Thanks to you, Matthijs, for the countless times you were offering your help and making sure our two labs run well together and for making sure lunch is punctual. Bas, I really appreciate

you sharing all your experience and showing me new ways do things in the lab. Nicco and Rodrigo, thanks for your patience while I was finishing this thesis and I am looking forward to finally starting our new experiment. Jie, it is great to have you in the group as a theoretician. Clemens, thanks for teaching me about the electronics and discussing the experiments. Alex, Beverly and Ian, I am grateful about the projects that we have been involved in together and good luck to you in the future. Micha, Kees and Roald, thanks to you too for all your contributions to the experiments.

I also don't want to forget all the help and support from so many people outside the group. Daniel, thanks for all the discussions and for being a great office mate. Mark, thanks so much for all your electronics knowledge that you were always happy to share. Sarwan, Martijn, Shun and Gary, thanks a lot for all the great discussions on optomechanics. Marios, Mario, Byoung-Moo and Christian, thanks to you too for helping me understand superconducting circuits and gravitational collapses a bit better. Thomas, I appreaciate you helping me with lab stuff so many times. Josh, thanks for sharing your knowledge about quantum memories and repeaters. Also thanks for all the mini projects, new ideas and helpful discussions Mathijs, João, Yaroslav, Fillipo, Max, Matt, Wolfgang, Witlef, Clemens and Fernando. Charles, Marc, Eugene, Marco, Ewan, Arnold and Frank, thanks for all the help in the cleanroom and around it. Thanks to you, Maria, for all the work you were doing for me and the group. I am grateful and impressed how easily you solved all of the problems with which I came to you over the years. A big thanks also to all other support staff, in particular Etty, Marije and Erika. Tino, thanks for keeping us safe and for always being up for a quick chat. Ronald, I really appreciate the great work you did machining the parts of our setup.

Also thanks to everyone making MED/QN super fun over the years, both on the third and on the first floor as well as outside of the campus. It was great to have you all around, Felix, Ranko, Ines, Dejan, Yildiz, Mafalda, Dima, Jorrit, Ignacio, Luigi. Davide, Alfredo and Jan, I am so happy for all the climbing we did. I'll keep fond memories of the Tuesdays Holger, Pascal, Marc, Nikos, Dirk, Joeri, Iacopo, Thierry and Edouard. And thanks to the PIs and everyone else as well for shaping the department the way it is.

Finally, I want to conclude with perhaps the most important people, my family. Without a doubt I owe the most gratitude to you, for your enduring support in the past and your continued support in the future.